universität wien

DISSERTATION / DOCTORAL THESIS

Titel der Dissertation / Title of the Doctoral Thesis

Three-dimensional description of vibration-assisted electron knock-on displacements in 2D materials

verfasst von / submitted by

Alexandru Ionut Chirita Mihaila MSc

angestrebter akademischer Grad / in partial fulfilment of the requirements for the degree of

Doktor der Naturwissenschaften (Dr. rer. nat.)

Wien, 2023 / Vienna, 2023

Studienkennzahl lt. Studienblatt / degree programme code as it appears on the student record sheet:	UA 796 605 411
Dissertationsgebiet lt. Studienblatt / field of study as it appears on the student record sheet:	Physik
Betreut von / Supervisor:	Assoz. Prof. Dr. Toma Susi

Acknowledgements

It's been about six years since I joined the Physics of Nanostructured Materials Group and now that my time here has come to an end, I would like to thank and commend the people that shaped me as a scientist and played an important role in who I am today.

First and foremost, I would like to thank my supervisor Prof. Toma Susi for his continuous support, not just through my PhD studies, but also during the early days when I was still a master student. Toma guided me along every step of my research project and has always been available whenever I was at an impasse. Without his knowledge and his rigorous way of doing science, which he openly shared with me, I would not have have achieved the results presented in this thesis. I want to thank him for carefully reviewing my thesis draft and for the countless tips that improved it by a great margin. Moreover, I am grateful to have had the opportunity to work under a young and accomplished scientist like himself.

I want to express my gratitude towards Prof. Jani Kotakoski for giving me the opportunity to start my masters' project in this group. Despite not having the knowledge, nor the expertise at that time to deal with the project at hand, he entrusted me with it, and thus paved the way to what later turned into my PhD project. Jani's advice has been valuable and much appreciated during my PhD, and helped reach a conclusion whenever I was at a crossroad. I am also grateful for his companionship and kindness, for all the events and activities that he organised or participated in, even outside of the academic life, which have contributed to many great memories.

I thank Dr. Alexander Markevich for the countless valuable discussions and scientific input, that made it possible to reach many conclusions in my project. On a personal level, I want to express my deepest form of gratitude for his moral support and friendship, and for the countless memories that made my stay in the group so much more entertaining.

I would also like to acknowledge Prof. J. Murray Gibson. During his short visit in Vienna, we

had many interesting discussions ranging from volleyball games to stories about his early days at Bell Labs. I was not only struck by his enthusiasm and endless curiosity - no matter the topic of discussion, but also by his strength of character and rationality in the face of difficult situations. Despite being a beacon of knowledge and wisdom, Murray has always treated me as an equal, has been encouraging and motivating, and therefore I owe him my gratitude and my utmost respect.

I would also like to thank my former and present colleagues Andreas Postl, Christoph Hofer, Ursula Ludacka, Alberto Trentino, Bernhard Fickl, Heena Inani, Rajendra Singh, Sophie Schäringer, Gudrun Pötzlberger, Clemens Mangler, Manpreet Kaur, Stefan Noisternig, Jacob Madsen, Harriet Ahlgren, Arixin Bo, Carsten Speckman, Wael Joudi, Manuel Längle, Fabian Kraft, Barbara Mayer, Diana Propst, Clara Kofler, David Lamprecht, Daniel Imrich, Valeria Chesnyak and the rest of the PNM group. A special shoutout you goes to Thuy An Buy, Mukesh Tripathi, Georg Zagler, Gregor Leuthner, Kimmo Mustonen and Michael Somma for their friendship and great memories we share. I want to acknowledge my former study colleagues and dear friends Mihaela Martin, Madalina Costea, Anita Resch, Sebastian Lekart and all my friends at the beachvolleyball court; a place that has acted as a shrine of rejuvenation during stressful times. A heartfelt thanks goes to Luca Anna Varhelyi for being by my side for many years throughout my studies and for all the moral support she has offered.

Lastly, I want to acknowledge my parents Marius-Ion and Dorina-Maria for guiding me towards a scientific path. Moreover, I want to thank them along with my brother Marius-Constantin and my grandparents Nicolae, Sinziana and Viorica for their continuous support and unconditional love.

Vienna, 13.01.2023

Abstract (DE)

Beobachtungen auf atomarer Ebene von Materialien werden oft unter Verwendung eines Transmissionselektronenmikroskops durchgeführt. Abhängig von der Beschleunigungsspannung der Elektronen, kann der Strahl Defekte in der Probe induzieren oder verschiedene Dynamiken hervorrufen. Der elastischer Stoß von Elektronen an Atome ist der Hauptschadenmechanismus und obwohl die Schwingungen der Atome das Wirkungsquerschnitt beeinflusst, wurde bisher nur die Schwingungsrichtung der Atome außerhalb der Ebene betrachtet. Da es eine nicht Übereinstimmung zwischen Experiment und Theorie gibt, präsentieren wir hier eine vollständige dreidimensionale Theorie der elastischer Stoße zwischen Elektronen und Atome, die uns erlaubt den Wirkungsquerschnitt beliebiger Dynamiken zu berechnen. Wir validieren das Modell mit zuvor experimentell gemessene Werte mit Hilfe der Rastertransmissionselektronenmikroskop und verwenden unsere Methodik um Dynamiken wie die reversible Sprünge der Stickstoffatome in Graphen, oder der Tausch zwischen Silizium- und Kohlenstoffatome zu erklären. Das Modell basiert sich auf ab-initio Methoden und kann auf beliebige Materialien angewendet werden um den elastischen Stoß als Schadenmechanismus zu erklären.

Abstract (EN)

Transmission electron microscopy characterization may damage materials, but an electron beam can also induce interesting dynamics. Elastic knock-on is the main electron irradiation damage mechanism in metals including graphene, and although atomic vibrations influence the displacement cross section, only the out-of-plane direction have been considered so far. Because of the mismatch between experiment and theory, we introduce a full three-dimensional first-principles theory of knock-on displacements to describe dynamics into arbitrary directions. We validate the model with previously experimentally measured values using the scanning transmission electron microscope and use our methodology to explain dynamics such as the reversible jumps of nitrogen atoms in graphene, or the swapping between silicon and carbon atoms. The model is based on ab-initio methods and can be applied to any material to explain knock-on as a damage mechanism.

Contents

List of Figures

List of Tables

Acronyms

2D Two-dimensional.

ADF Annular dark field.

ASE Atomic Simulation Environment.

CVD Chemical vapor deposition.

DFT Density functional theory.

DFTB Density-functional tight-binding.

EELS Electron energy-loss spectroscopy/spectrometer.

HAADF High-angle annular dark field.

KMC Kinetic Monte Carlo.

MAADF Medium-angle annular dark field.

MD Molecular dynamics.

PAW Projector-augmented waves.

STEM Scanning transmission electron microscope/microscopy.

SV Single vacancy.

TEM Transmission electron microscope/microscopy.

WMSE Weighted mean-square error.

Chapter 1

Introduction

1.1 Motivation

Throughout history, mankind gazed out into the night sky without recognizing the stars of our galaxy as other suns, or the billions of galaxies making up the rest of our universe. While telescopes have let us view and understand the cosmos, microscopes have granted us access to the invisible world around us, allowing us to view the smallest components of living and inanimate objects alike. There are mentions of people using lenses for magnification since antiquity [1], but the first optical microscope was arguably built by Hans and Zacharias Janssen in 1590 [2], and this paved the way for many scholars in the pursuit of finding out what matter is made of. Microscopy has been ever since the backbone of many scientific breakthroughs, such as the discovery of cells by Robert Hooke in 1665 [3] or the discovery of bacteria in 1676 by Antonie Van Leeuwenhoek [4].

In 1873, Ernst Abbe found that the resolution of visible-light microscopes is not constrained by the quality of the instrument but by the wavelength of light and the aperture of its optics [5], and so reported that the smallest resolvable distance between two points can not be smaller than roughly half the wavelength of the imaging light beam. However, this did not stop Ernst Ruska and Max Knoll to build the first electron microscope in 1931 [6], who were at that point counting on the extremely small size of the electrons [7], since they were not aware of Louis De Broglie's work on wave-particle duality in 1924 [8]. They found out about De Broglie's work in the summer of 1931, that even for the electron microscope, the resolution should be limited by the wavelength, but were immediately satisfied when they used his equation to calculate the wavelength of the

electron to be five orders of magnitude smaller than visible light [7]. However, resolution was still limited and Otto Scherzer proved in 1936 that chromatic and spherical aberrations of rotationally symmetric electron lenses are unavoidable [9]. It was only after more than half a century that Joachim Zach and Max Haider substituted the electric multipoles for magnetic multipoles, which are mandatory for eliminating chromatic aberrations [10], and achieved an improvement in the resolution of an electron microscope.

Despite being first built in 1938 [11] by Baron Manfred von Ardenne, the scanning transmission electron microscope (STEM) did not see many improvements until Albert Crewe developed the field emission gun [12] in 1969 and just one year later achieved a resolving power of 5 Å and reported the "visibility" of single atoms [13] by imaging uranium on thin carbon films. This progress was followed by Ondrej Krivanek and colleagues [14] who managed to correct for spherical aberrations and demonstrated a significant resolution improvement of STEM [15] in 2003. Around the same time, Kostya Novoselov and Andre Geim discovered graphene in 2004 [16], which led to a surge in two-dimensional materials research and atomic-level observations using transmission electron microscopy (TEM) [17].

In a TEM, a beam of accelerated electrons is transmitted through the sample, interacting with it as it passes through. The first description of the interaction between charged particles due to the Coulomb force by Ernest Rutherford dates back to 1911 [18]. Further, the theoretical cross section for the Coulomb scattering between an electron and a nucleus was derived by Nevill Mott [19] in 1930, who also considered the spin of the electron. Several years later in 1948, McKinley and Feschbach expanded the results of Mott in a power series, obtaining an analytical cross-section formula for the relativistic scattering between an electron and nuclei up to middle-Z elements [20]. Depending on the acceleration voltage, the beam may also induce defects in the sample either due to elastic or inelastic interactions with the target atoms. Knock-on atom displacements due to elastic electron backscattering [21] affect all materials, and are the primary damage mechanism for graphene [17]. For non-destructive imaging, the electron should not transfer more energy than the energy needed to displace an atom from the lattice. The major improvements in aberration correction have not only allowed the construction of electron microscopes with sub-Ångström resolution but have also enabled to operate them at acceleration voltages below the energy thresholds where one might induce defects or even destroy the sample.

Operating an electron microscope at energies close to the knock-on threshold requires a more

complete description of the displacement cross sections. Jannik Meyer and colleagues [22] have shown that a static lattice approximation was insufficient in predicting any defect creation in graphene at acceleration voltages below 108 keV, and that accounting for out-of-plane vibrations of the target C atoms resulted in a better agreement with experimental observations. The same was observed Hannu-Pekka Komsa et al. [23] in a similar study on different transition metal dichalcogenides. Further improvements to the theory came from Toma Susi et al. [24] who derived the atom velocity distribution from the phonon density of states instead of using a Debye model, and by myself and colleagues [25], where the effect of the temperature on the displacement threshold energy of the atoms was quantified. However, for a full physical description of the electron-atom interactions, both nuclear velocities and momentum transfers in all directions must be included.

This work introduces a full three-dimensional theory of electron knock-on displacements for arbitrarily moving target atoms, and explores its implications for knock-on displacements from pristine graphene as well as for the beam-induced dynamics of silicon substitutions [26, 27], and the reversible dynamics of its pyridinic nitrogen impurity sites [28]. The timescale at which such processes happen is on the order of 10^{-12} s, and thus can only be visualized and understood using atomistic simulations. Density functional theory (DFT) molecular dynamics (MD) is an established tool to investigate many-body condensed matter and biomolecular systems. Using DFT-MD, the emission of the target atoms under different conditions can be simulated in order to find the displacement threshold energies and to understand the conditions under which the beam-induced dynamics occur. Those findings can then be compared to observations and used to validate a three-dimensional theoretical framework for predicting the experimental cross section, which is derived from relativistic momentum and energy conservation.

1.2 (Scanning) transmission electron microscopy

To find out what materials are made of and to improve their synthesis, atomic-scale characterization is needed to study their structure and composition. The transmission electron microscope (TEM) and the scanning transmission electron microscope (STEM) have emerged as some of the best tools to fulfill this purpose due to recent advances in instrumentation, which allow to correct the aberrations caused by imperfect electron optics [29–31] and thus open the way to atomic-resolution imaging.

Electrons have wavelengths on the order of picometers (10^{-12} m) and therefore can interact with the atomic lattice and provide meaningful information of interatomic distances that are on the order of a few Ångströms (10^{-10} m). As mentioned above, TEM and STEM both use electrons for the purpose of imaging, and in Fig. 1.1 we show a schematic comparison between them. In a conventional TEM, the electrons produced by a source go through a condenser aperture, and are focused as a parallel beam onto the sample by a condenser lens. The transmitted electrons will then pass through an objective aperture to exclude electrons scattered at high angles and are forwarded onto the objective lens. The objective lens will focus the electrons to create an image, but some of them will have different velocities (different wavelengths) due to instability in the acceleration voltage or due to inelastic scattering with the target sample, and so they will have

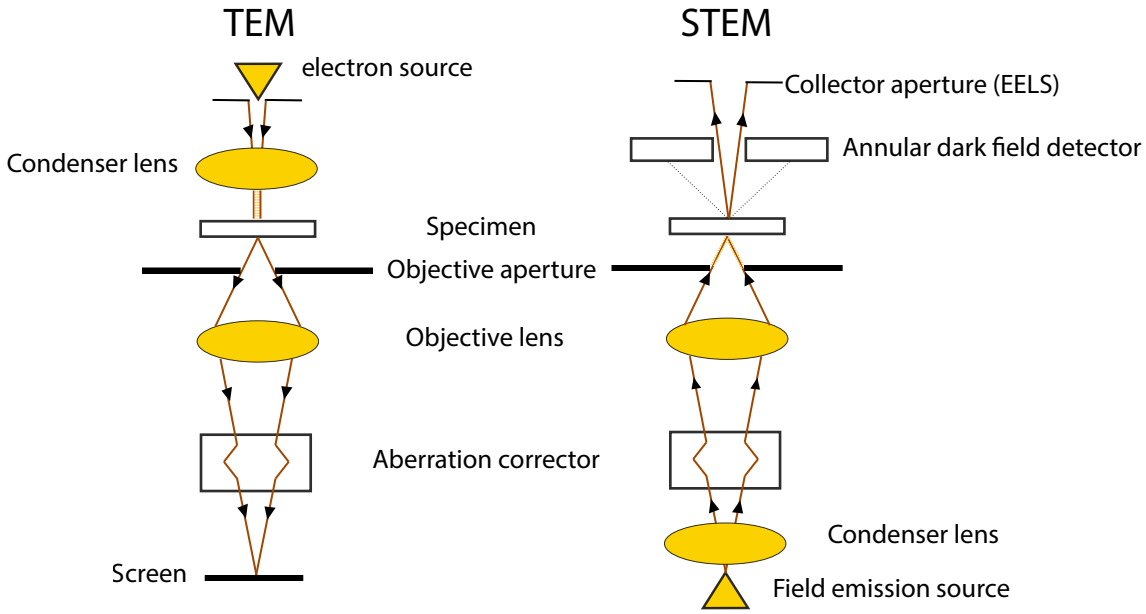

Figure 1.1: Schematic comparison between a conventional TEM and a scanning TEM

different focal lengths as a result of chromatic aberrations (Fig. 1.2c). Electrons passing through the periphery of the objective lens will be refracted more than the ones passing closer to the axis due to spherical and other aberrations (Fig. 1.2b). It is challenging to suppress aberrations, since the aberration coefficients of electromagnetic lenses are positive [32]. However, sequences of sextupole and octupole magnets can be used as aberration correctors before the image is finally recorded. Besides that, also selecting electrons that are closest to the optical axis by inserting limiting apertures can help, since they are not affected as much by the lens aberrations.

In contrast to the conventional TEM, in a STEM the aberration correction of the electrons happens before they enter the objective lens. They are focused into an Ångström-sized beam which scans the sample pixel by pixel. The image is then formed by the electrons that scatter due to the Coulomb interaction with the nuclei, and which are collected by an annular dark field (ADF) detector. The angle at which the electrons scatter is highly dependent on the atomic number Z of the atoms. If an atom has a high Z, more electrons will be scattered to high angles and collected by a high-angle ADF (HAADF), or if Z is low, by a medium-angle ADF detector (MAADF). This imaging technique is often called Z-contrast imaging. These electrons that scatter elastically with the sample contribute to the image, while the ones that undergo inelastic interactions can be collected by an electron energy-loss spectrometer (EELS), which can be used to provide the chemical composition at the atomic scale.

Having a highly focused aberration-corrected electron beam makes the STEM one of the most powerful tools to achieve sub-Ångström resolution imaging. While the unprecedented quality of images are giving us valuable information on the structure of the samples, the electron probe can also be used to manipulate a Si impurity in graphene [26, 27] by means of controlled electron irradiation of the neighboring C atoms.

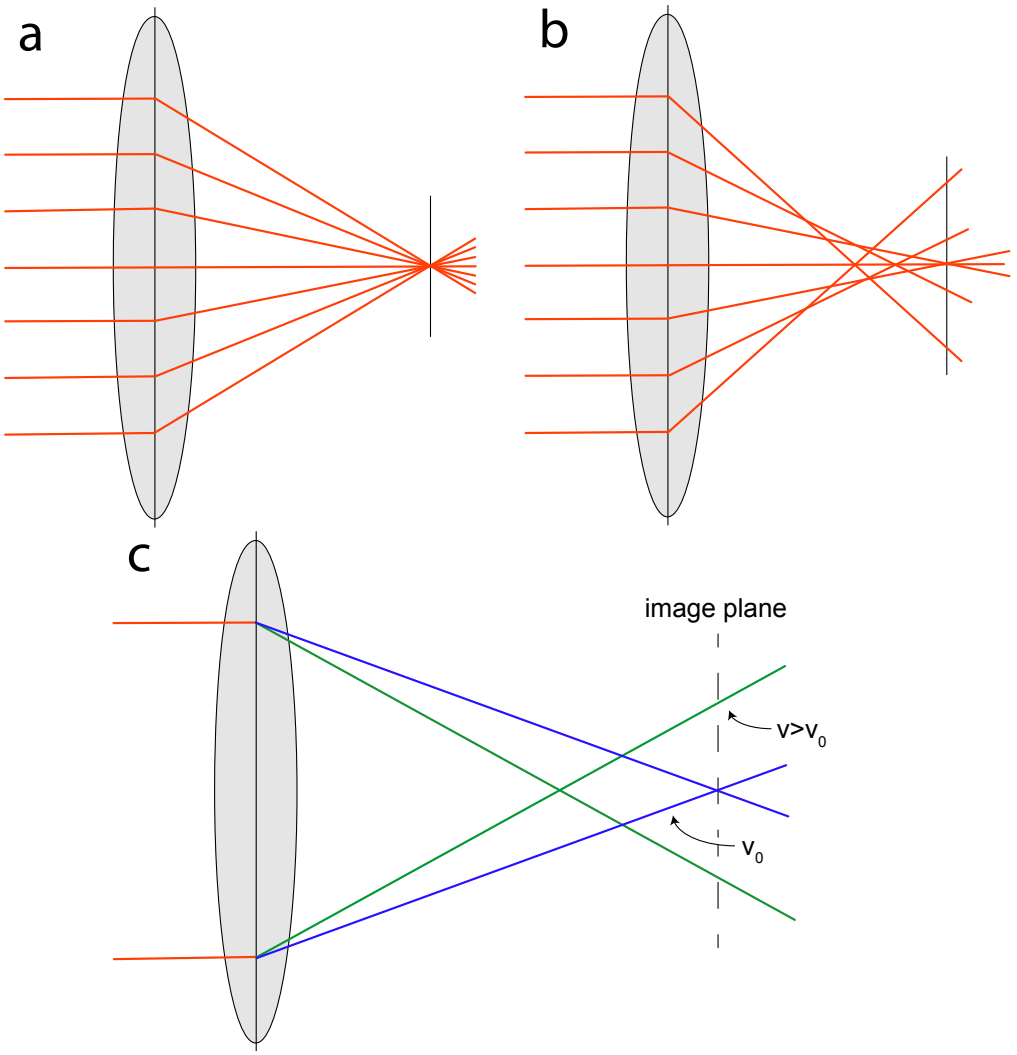

Figure 1.2: a) Electrons passing through an ideal lens. Electron rays affected by b) spherical and c) chromatic aberrations (v and v_0 represent electron velocities).

1.3 Graphene

In the last two centuries there have been several major breakthroughs in the field of material science, such as the discovery of polymers in 1830, semiconductors in 1833 and plastic in 1941. The existence of two-dimensional (2D) materials had been argued before [33, 34], but they were thought to be unstable at room temperature because thermal fluctuations would be comparable to the distance between the atoms. Andre Geim and his Ph.D. student Konstantin Novoselov isolated graphene, a one-atom thick layer of carbon atoms, for the first time and after several failed attempts managed to publish their discovery in October 2004 [16]. The Nobel prize in Physics for this discovery was awarded to them in 2010.

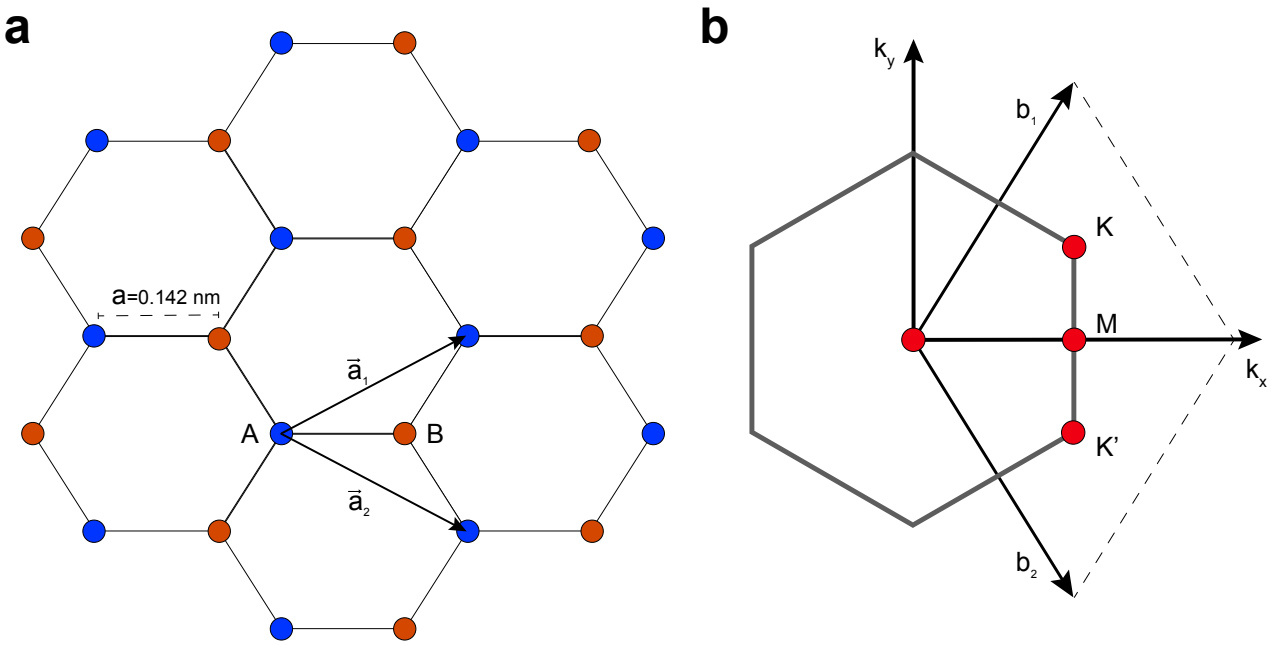

Figure 1.3: a) Graphene lattice structure in real space with the corresponding unit vectors, b) Reciprocal space with the first Brillouin zone and high-symmetry points.

Graphene is a single layer of carbon atoms that are bound in a honeycomb lattice (see Fig. 1.3). It is the building block of graphite, which consists of multiple stacked graphene layers bound by the van der Waals force. The graphene honeycomb lattice is built out of two triangular sublattices (Fig. 1.3a, A (blue) and B (orange)). Assuming the distance between the carbon atoms is a = 0.142 nm, the lattice vectors can be calculated by the properties of the isosceles triangle as

$$\vec{a}_1 = \frac{a}{2}\left(3, \sqrt{3}\right), \quad \vec{a}_2 = \frac{a}{2}\left(3, -\sqrt{3}\right). \tag{1.1}$$

The correspondent reciprocal lattice vectors $\vec{b}_1$ and $\vec{b}_2$ (Fig. 1.3b) to the triangular Bravais lattice of graphene are

$$\vec{b}_1 = \frac{2\pi}{3a}\left(1, \sqrt{3}\right), \quad \vec{b}_2 = \frac{2\pi}{3a}\left(1, -\sqrt{3}\right). \tag{1.2}$$

Despite its 2D nature and being one-atom thick, graphene is not completely flat, displaying ripples in the structure that can go up to 1 nm in height as transmission electron microscope studies have

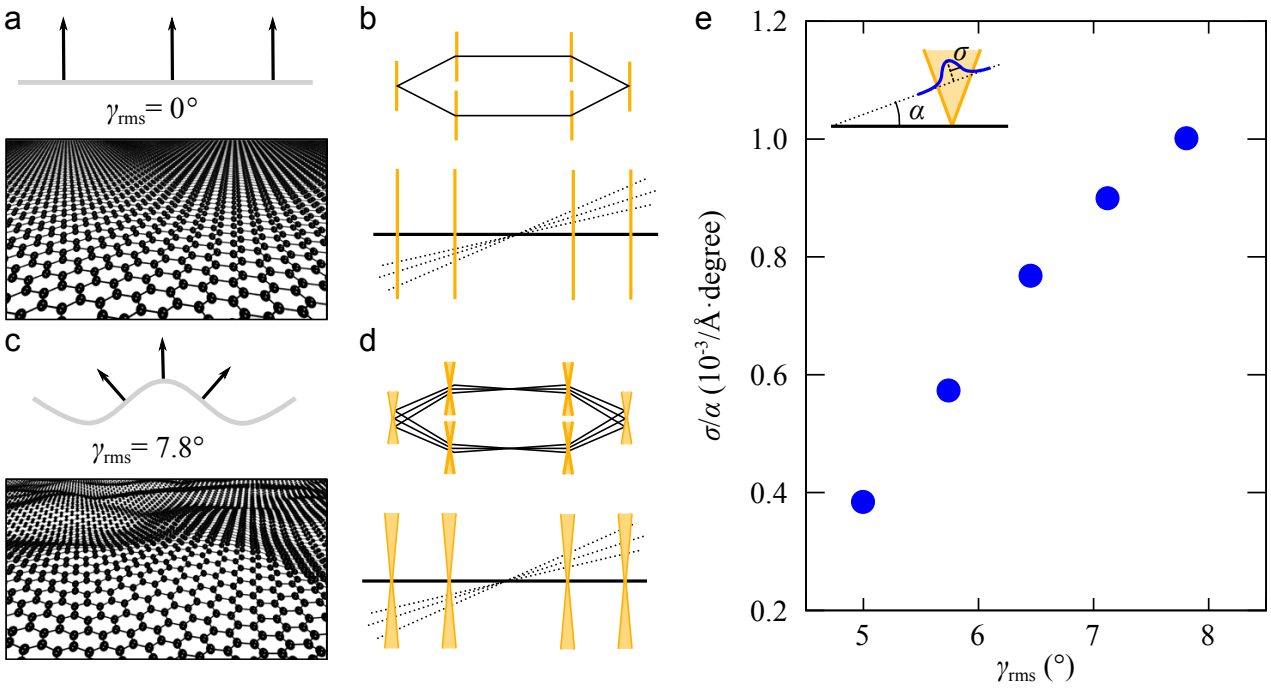

Figure 1.4: Effect of varying surface inclination on the graphene diffraction pattern. A flat sample has parallel lattice normals throughout **a**, which leads to sharp rods in the reciprocal space **b** giving the same width for diffraction spots regardless of the sample tilt. In contrast, a corrugated sample **c** (here with root mean square inclination of $\gamma_{\mathrm{rms}} = 7.8°$) exhibits cone-like volumes in the reciprocal space **d** that lead to increasing diffraction spot sizes for higher sample tilts. **e** Relationship between the diffraction spot size (σ) and the sample tilt (α) for simulated corrugated graphene structures with varying values of γ_{rms}. Figure adapted from Ref. [35] (CC-BY).

confirmed [35, 36]. It is challenging to measure such ripples in a one-atom thick membrane, especially since these subnanometric undulations can not be directly imaged due to the depth of field in a TEM. However, they can be estimated from the electron diffraction patterns (see Fig. 1.4), where the width of the diffraction spots can be correlated with the inclination of the plane [35]. However, for the purpose of our study, a flat lattice is an adequate local description.

Each carbon atom in the graphene lattice has six electrons, two on the core shell and four on the valence shell, with a ground state electronic structure $1s^2\ 2s^2\ 2p^2$. Electrons in the $1s$ orbital do no contribute to chemical bonding. The outer-shell electrons on the $2s$, $2p_x$ and $2p_y$ orbitals hybridize to form three sp^2 in-plane orbitals, which are responsible for the strong σ bonds (Fig. 1.5a, b) that result from the head-to-head overlap of orbitals between the carbon atoms. These bonds have an angle of $120°$ between them resulting in the hexagonal structure of graphene (Fig. 1.5c). The p_z orbital, which hosts the remaining electron, is perpendicular to the others and combines with the p_z orbitals of the neighbouring C atom to form π-bonds. One can visualize the

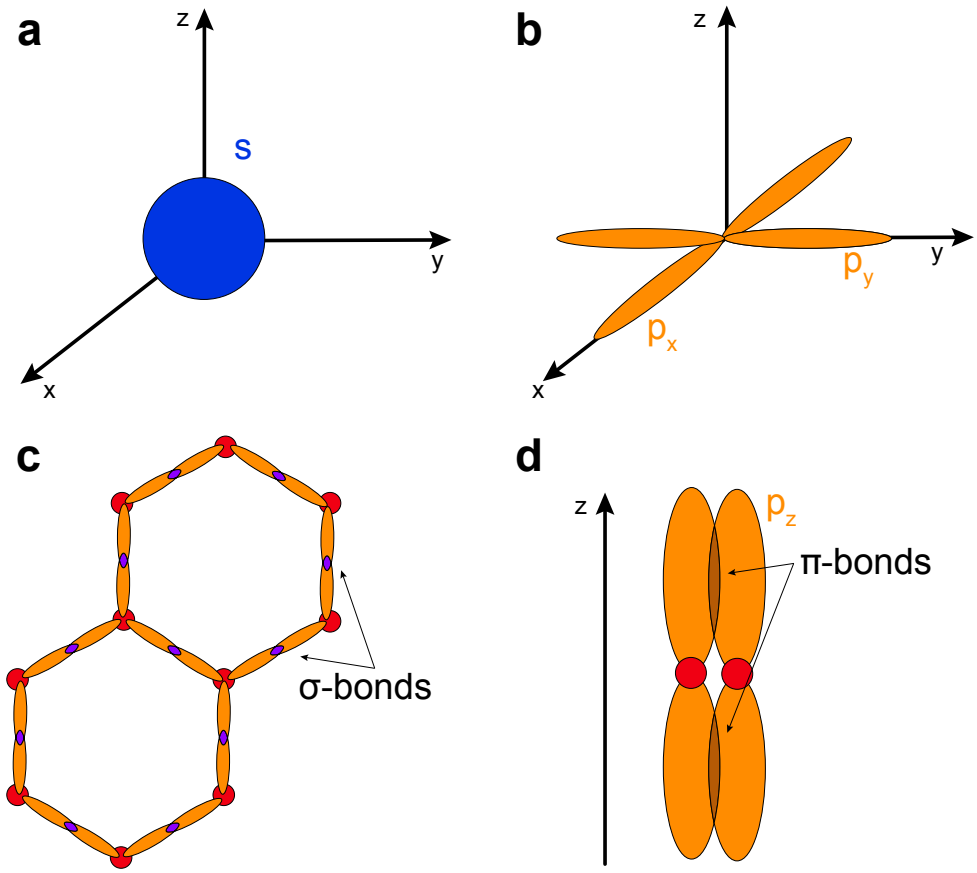

Figure 1.5: Orbital hybridization of the carbon atoms in the graphene lattice.

π bonds as the lateral overlap between the p_z orbitals (see Fig. 1.5d), where the electrons can hop from one sublattice to the next.

The important physics of graphene takes place at the reciprocal-space two points of high symmetry, K and K', where the valence and conduction band touch at the corners of the Brillouin zone (Fig. 1.3b) resulting in a zero band gap:

$$\vec{K}' = \left(\frac{2\pi}{3a}, \frac{2\pi}{3\sqrt{3}a}\right), \quad \vec{K} = \left(\frac{2\pi}{3a}, -\frac{2\pi}{3\sqrt{3}a}\right). \tag{1.3}$$

The electrons in the vicinity of these points can be described by the Dirac equation in two dimensions and behave like massless fermions [37]. This explains some of graphene's electronic properties, which makes the material unique, such as the high electron mobility [38, 39] or the room-temperature quantum Hall effect [40]. As a consequence, the dispersion of the electrons is linear with very high mobility. Graphene behaves like a zero-gap semiconductor and the charge

carriers have an electron mobility over 15,000 $\mathrm{cm}^2/\mathrm{Vs}$ at room temperature [16, 41]. Graphene is the strongest material ever measured and also the most stretchable crystal [42] thanks to the sp^2-hybridized bonds. It has a tensile strength of 130 GPa and an elastic modulus of 330 N/m [42]. Its thermal properties are also remarkable, boasting a thermal conductivity of up to 5000 W/m K at room temperature [43], which is about 20 times higher than that of copper, and has a negative thermal expansion coefficient between 0 and 700K [44].

However, these exceptional properties are mostly present in defect-free pristine graphene and any deviation from this, such as defects or impurities [45], may cause changes in the properties.

1.4 Defects in graphene

"*Crystals are like people, it is the defects in them which tend to make them interesting!*"
- Colin Humphreys.

Defects in crystals can take many forms and depending on their dimensionality (ranging from 0 to 3), can be classified as point defects, line defects, surface defects and bulk defects. Zero-dimensional point defects are localized disruptions in the regularity of the lattice such as interstatial atoms, bond rotations, missing atoms or impurities. Line defects or dislocations, are one-dimensional defects and represent an abrupt change in the regular arrangement of atoms along a line in a solid. Two-dimensional defects are discontinuities in the crystal structure of a surface, where regions of this surface have a different orientation with respect to one another, and three-dimensional defects manifest as voids or clusters of impurities within a bulk material.

The highly energetic electron beam can transfer a considerable amount of kinetic energy to the atoms and if that energy exceeds their displacement threshold energy (the energy required to displace an atom from the lattice) the atom is removed and a defect is created. The most common type of defect resulting from irradiation of solids are Frenkel defects [46, 47]. They form when an atom receives enough energy to displace it from its initial lattice position and end up in an interstatial site within the crystal, leaving a vacancy behind. However, in 2D materials such

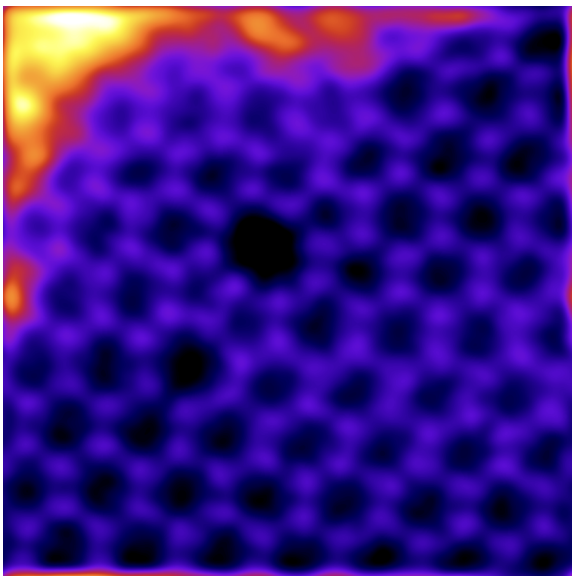

Figure 1.6: STEM image of graphene with defects. We can see an octagon, three pentagons and an heptagon. (Image courtesy of Mukesh Tripathi)

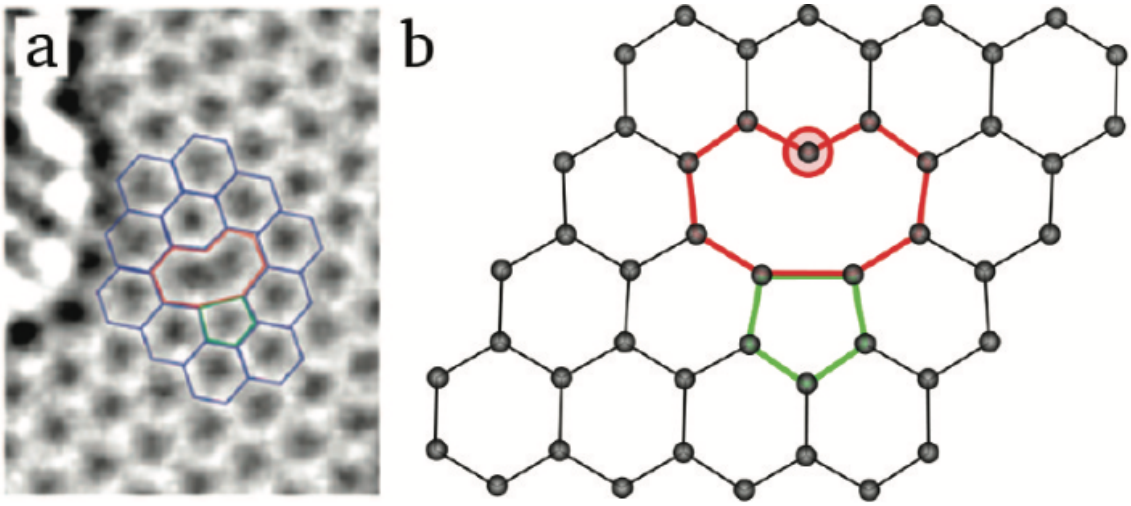

Figure 1.7: a) Single vacancy in graphene as seen in an experimental TEM image (adapted with permission from Ref. [50]. Copyright 2008 American Chemical Society); b) its atomic structure obtained from DFT calculations. (Reprinted with permission from Ref. [49]. Copyright 2011 American Chemical Society)

as graphene the atoms would either be knocked out completely, or if the energy and momentum transferred are not high enough, they might cause bond rotations and thus creating Stone-Wales type defects [48]. In Fig. 1.6 we can see the defective graphene lattice with the C atoms forming one octagon, one heptagon and few pentagons as a result of two missing atoms and a 90° C–C bond rotation.

One of the simplest defects in 2D materials is a missing atom. One missing carbon atom from the graphene lattice forms a single vacancy (SV) site as seen in Fig. 1.7. Here, the missing atom leads to the formation of a five- and a nine-membered ring, with one of the C atoms left with a dangling bond [49]. Removing more than one atom from the lattice can lead to multiple vacancies and even formation of large holes. For example, double vacancies can be created by the merging of two SV or by removing two neighboring atoms (see Ref. [49] for such examples). As a rule of thumb, vacancies with an even number of missing atoms are energetically more favored than the ones with an odd number because their dangling bonds are saturated.

Another type of defect are substitutional impurities in graphene, where atoms such as silicon, boron, nitrogen or germanium have been observed to replace C atoms [28, 51–56] (see Figure 1.8). These kind of defects are of particular interest in this work, since they can non-destructively move in graphene [26, 28, 57], thus opening the door to designing custom patterns within graphene, such as embedded silicon structures [58]. There are many physical and chemical routes to synthesize doped

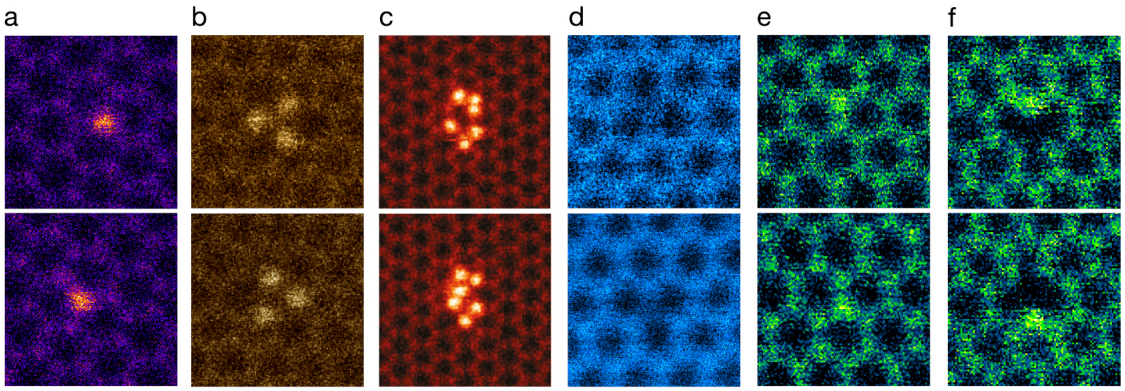

Figure 1.8: Electron beam-induced dynamics (top and bottom show consecutive ADF images) from left to right a-f: substitutional Si, Si trimer in a hexavacancy, Si_6 cluster in a pore, substitutional B, substitutional N, pyridinic N in a single vacancy. Figure reproduced from Ref. [55] (CC-BY 3.0).

graphene, including ion implantation and chemical vapor deposition using a suitable heteroatom-containing precursor. However, since these go beyond the scope of the current work, the interested reader is referred to recent reviews on the topic [59, 60].

1.4.1 Silicon impurities in graphene

In 2012, using a combination of Z-contrast imaging and electron energy-loss spectroscopy (EELS) [61, 62] within a STEM operated at 60 keV, two distinct substitutional Si defect geometries were observed in graphene [51]. The Si impurities were either substituting a single C atom or a C–C pair, which formed either a three- or a four-coordinated Si defect, respectively. The exact origin of the Si impurities is not exactly known, but are thought to originate from the chemical vapor deposition (CVD) process used for growing graphene or the glassware used to process samples [51, 62]. The buckled structure surrounding the three-coordinated Si atoms was inferred by analyzing electron energy-loss spectra [51] and also later directly by acquiring images when the sample is tilted [63]. The Si atom may buckle up or down with respect to the graphene lattice causing a deformation in the out-of-plane direction. Despite having a symmetric appearance in normal-incidence plane-view images [51, 64], this buckling causes a shift of position in the tilted projections [63]. This can be visualized by overlaying a flat and a relaxed model on top of the STEM images in Fig. 1.9.

While the 60 keV electron beam rarely transfers enough energy to knock out the carbon atoms, experiments have shown that three-coordinated Si atoms change places with neighboring C atoms under such irradiation [64]. To understand the observed swapping mechanism, DFT/MD

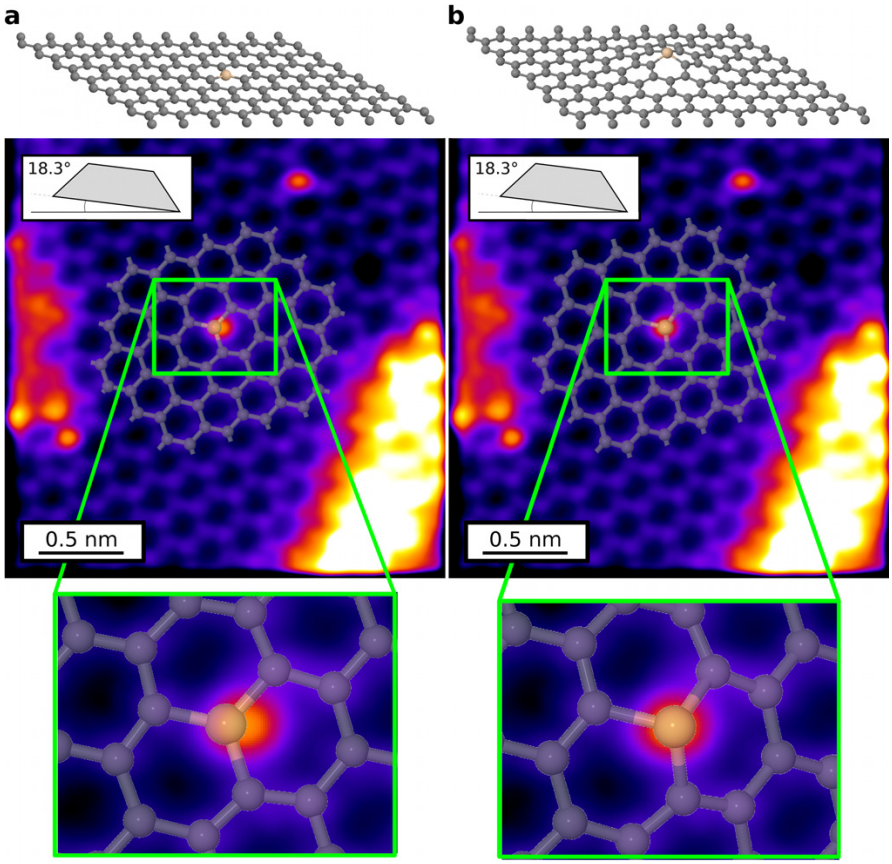

Figure 1.9: STEM image of a Si dopant in graphene overlaid by a flat model (a) and a relaxed buckled model (b). On the top row, side views of the models are shown. The magnified image (bottom) shows a poor match of the Si atom position using the flat model (a) but an excellent match using the buckled structure (b). Figure adapted with permission from Ref. [63].

simulations were employed [64](see Sec.1.7.1). If one of the C neighbors gets slightly but not completely displaced from the lattice, the Si simultaneously relaxes into the place vacated by the C atom, while it gets pulled back into the initial place of the Si (see Fig. 1.10). In a followup study, the controlled manipulation of a three-coordinated Si impurity at 55 and 60 keV was established by Tripathi et al. [27], where they precisely moved the Si atom along a hexagonal path as shown in Fig. 1.11. This was achieved by placing the beam of the STEM on one of the C atoms between scanning frames until a jump was observed.

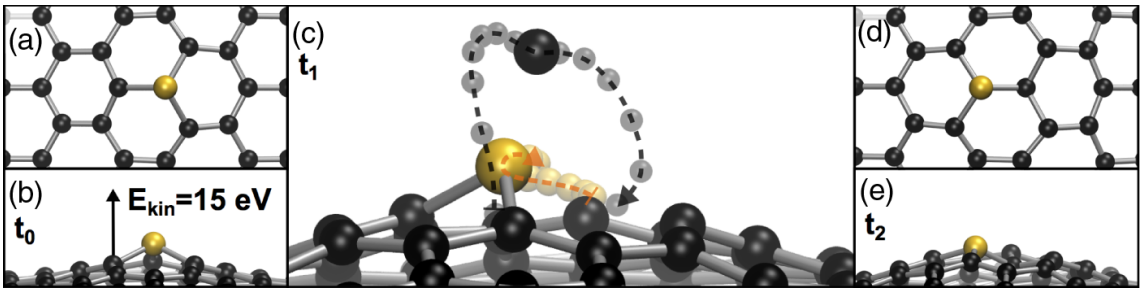

Figure 1.10: Molecular dynamics simulation of an electron impact delivering 15 eV to a C atom neighboring Si–C_3 in graphene. (a) Top view of the starting configuration at time t_0. (b) Side view at t_0, with the kinetic energy indicated on the impacted atom. (c) A snapshot at t_1 ($\approx$ 700 time steps into the simulation), with the entire trajectories of the ejected C atom and the Si atom marked by semitransparent balls and dashed lines. (d) Top view near the end of the simulation at time t_2 after $\approx$ 1400 time steps. (e) Side view at time t_2. Note that although the atomic motion has not ceased by this point, no further changes in the atomic configuration follow. Figure reproduced from Ref. [64] (CC-BY 3.0).

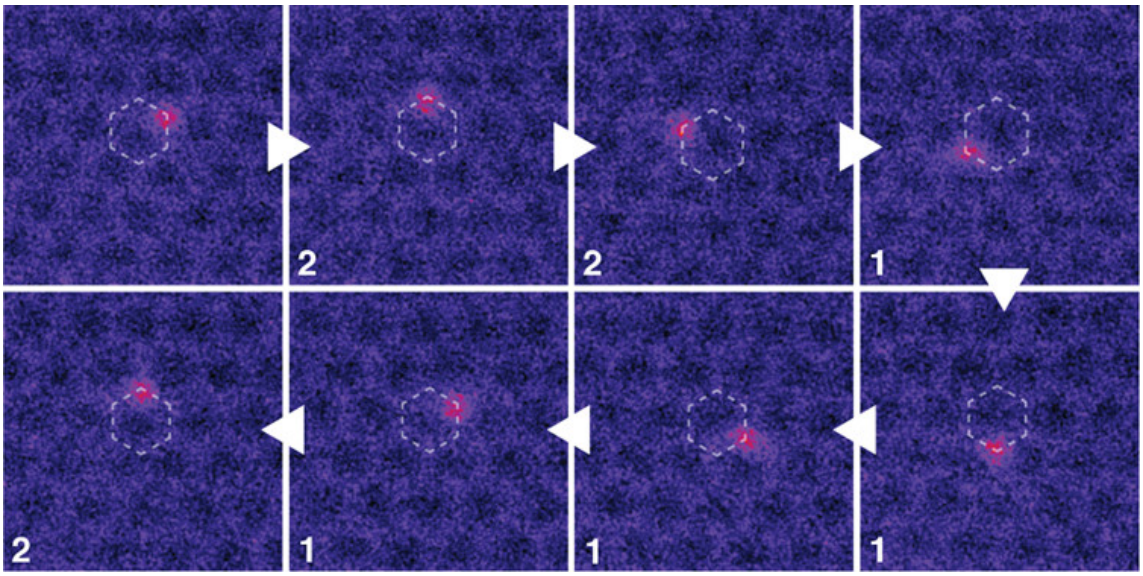

Figure 1.11: Electron-beam manipulation of Si at 60 keV around a hexagon. The overlaid numbers show the number of 10 s spot irradiations preceding each frame, and the triangles indicate the ordering of the frames. Figure reproduced from Ref. [27] (CC-BY 4.0).

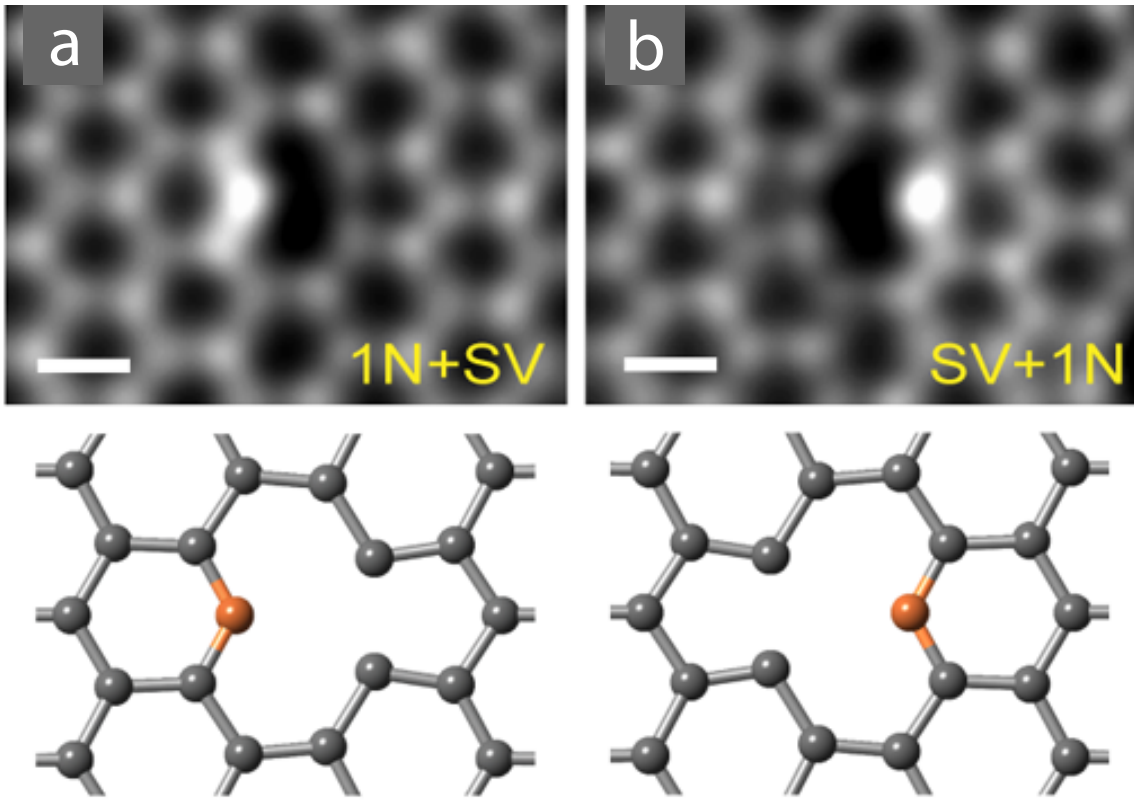

Figure 1.12: Single pyridinic N at two equivalent sites a) with the corresponding model b). Scale bar is 2 nm (Figure adapted with permission from Ref. [28]. Copyright 2015 American Chemical Society)

.

1.4.2 Nitrogen impurity at a single vacancy

Single vacancies (SV) are common in graphene and have been observed by TEM [50]. Of interest in this work are SV where the C atom with a dangling bond is substituted by a N atom, after exposing the CVD grown graphene to N in a gas chamber at 100° C [28]. More recent studies [65] have also reported N substitutions in graphene without intentional doping. The pyridinic nitrogen dopant has been observed to jump back and forth across the vacancy under the scanning electron beam at a temperature of 500° by [28] (Fig. 1.8f and Fig. 1.12) and later by us at room temperature [57] (Fig. 3.10). However, these dynamics of the pyridinic nitrogen at the single vacancy have yet to be explained and are central to this work as we will see further in Chapter 3.

1.5 Irradiation effects in solids

The effects of electron irradiation in solids is a field of intense research, since plenty of them are investigated by means of electron microscopy. Formation of unexpected structures due to irradiation has often been observed in carbon nanostructures and graphitic materials. The electron beam can transform graphene into single-atom carbon chains and carbon nanoribbons [66, 67], graphene flakes into fullerenes [68], or amorphise graphene under prolonged exposure [69]. Therefore it is of great importance to understand how energetic particles such as electrons interact with the target, and what are the effects caused by the energy or momentum transfer that take place. The most common effects of irradiation are:

- knock-on displacement of atoms;
- electronic excitations and ionization;
- collective electronic excitations such as plasmons;
- phonon excitation and heating;
- radiolysis and bond breaking;
- x-ray emission ;
- emission of secondary or Auger electrons.

When an accelerated electron encounters an atom, it may first penetrate the outer loosely bound electron cloud, go further to interact with the core-shell electrons, and could also finally encounter the nucleus. Several effects might arise along the electron's trajectory as is pictured in Fig. 1.13, where SE and BSE stands for secondary electrons and backscattered electrons, respectively. We split these effects into those which lead to direct atom displacements and those that do not. The likelihood of damaging the target material by knocking out atoms increases with the acceleration voltage and is described by elastic interactions between the electron and the atom, while ionization caused by inelastic interactions will increase at lower acceleration voltages. In the next section, we will focus in more detail on elastic interactions and how they contribute to the displacement of atoms and introduce some of the irradiation effects caused by inelastic interactions.

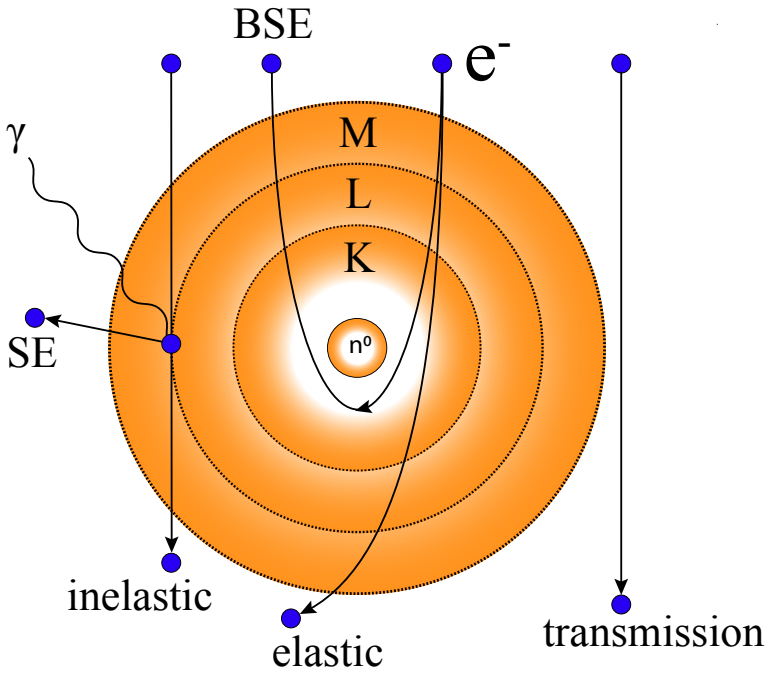

Figure 1.13: Electron-nucleus interactions.

1.5.1 Electron-atom elastic interactions and knock-on damage

An elastic or quasi-elastic interaction between an electron and an atom will result in the scattering of the electron without any or negligible loss of energy due to the large difference in mass between the electron and an atom (e.g a C atom is roughly 22000 times heavier than an electron). The electron needs to be fast enough to penetrate the electron cloud and get close to the nucleus where it will scatter in a different direction due to the Coulomb interaction (see BSE in Fig. 1.13). It is the change in direction of the electron that causes a momentum transfer.

Damage production through electron irradiation has been studied for more than half a decade, especially defect production (Frenkel pairs) in metal crystals [70]. To quantify the amount of defects produced the electrical resistivity was measured, since it is proportional to the concentration of created Frenkel defects [46, 47, 70]. The most important quantity in these studies, which describes the minimum amount of energy necessary to displace an atom from the lattice, is called the displacement threshold energy E_{d}. In solids, one electron impact may cause multiple displacements, depending on how much energy the electron transfers to the atom. According to the Kinchin-Pease theory [71], a minimum energy of at least double the displacement threshold energy E_{d} must be transferred to an atom so that it may induce further displacements. Thus,

we assume that atoms receiving energies between E_{d} and $2E_{\mathrm{d}}$ are displaced, but will not induce further displacements [71]. The orientation of the sample with respect to the incoming electron beam also affects the displacement threshold. One of the first studies to measure and account for the anisotropy of the displacement threshold energy in single copper and platinum crystals with different orientations were done by Bauer et al. [46] and Jung et al. [47] in 1964 and 1973, respectively. They have shown that both fcc (face-centered-cubic) metals exhibit the lowest displacement thresholds in the closest-packed directions (110) and (100). The anisotropy of the displacement threshold is valid not just for 3D structures but must be accounted for in low-dimensional materials, as shown by Zobelli et al. [72] for carbon nanotubes and in this work for graphene. However, compared to solids, once the atom has been displaced from its lattice position, in 2D materials it will most likely be removed from the system and not get the chance to recombine as an interstitial.

Knock-on collisions of highly energetic electrons with atoms affects all materials and are the primary damage mechanism in carbon nanostructures [21] and graphene [17]. The displacement threshold energy for a C atom in graphene is about 21.13 eV [24] and the maximum amount of kinetic energy transferred by an electron at an acceleration voltage of 100 keV in the static nucleus approximation [72] is 20.05 eV. The energy difference of about 1 eV between the experimental and the predicted displacement thresholds is not due to energy conservation, but rather from the momentum conservation that is not quite correct in the static lattice approximation. In any real material the nuclei are not at rest, and depending on the velocity and the direction they are vibrating, this may enable a substantially higher amount of kinetic energy to be transferred to the nucleus as was shown recently [24, 25, 73]. Those studies accounted for atoms vibrating in the out-of-plane direction, which may lead to a kinetic energy transfer of up to 24 eV depending on the velocity of the atom, a boost of almost 4 eV. At electron acceleration voltages below 100 keV, irradiation damage in graphene cannot be explained in the static approximation, but is observed down to 85 keV [22, 24]. To date, the momentum transfer to the nuclei has only been treated in the out of-plane direction. For a complete description of electron-beam induced dynamics such as Si-C inversions [27], pyridinic N jumps [28, 57] and knock-on damage, momentum transfers in all directions must be included. In Sec. 3.1.2 we present a full three-dimensional theory of elastic electron-atom interactions for arbitrarily moving target atoms, which can be used to predict the probabilities of knock-on and beam-induced dynamics by calculating the corresponding displacement cross sections, which is the method used to quantify such beam-induced effects.

1.5.2 Inelastic interactions

Inelastically scattering electrons are also important, because they generate signals that can reveal the chemical composition of the target and cause ionization. Electron-electron interactions leading to generation of characteristic x-rays, secondary electrons, plasmons and ionization damage will be discussed below.

Characteristic x-rays To produce characteristic x-rays, a beam electron must penetrate through the outer shells and reach the core (inner shell) electrons. If the energy transfer is greater than the binding energy of an inner-shell electron, it escapes leaving a hole behind. The beam electron continues through the specimen after losing energy and leaves the atom in an excited state, which we describe as ionized. Subsequently, the atom will return to its ground state by filling the hole with an electron from one of the outer shells. When an outer-shell electron falls into the inner shell, a photon can be released with an energy equivalent to the difference between the outer shell and the inner shell involved in this transition. Since each chemical element has a specific set of energy levels, this energy difference will be characteristic to the element involved.

Secondary electrons Secondary electron emission happens when the beam electron ejects electrons from the sample. Outer-shell electrons from the conduction and valence bands are more easily ejected, since their binding energies are less than 50 eV, while core electrons require higher energies (e.g. 8.9 keV for Cu) and often lead to characteristic x-ray generation. However, the energy when a core hole is filled is not always released in the form of a photon, but can be transferred to another electron, which is then ejected from the atom. This second emitted electron is called an Auger electron. Secondary electrons can be used as an imaging technique to study the surface of materials (especially in scanning electron microscopy) or for elemental identification.

Plasmons A plasma is a gas of charged particles, but a metal can also be seen as a sort of "metallic" plasma due to the confined nuclei and the "sea" of free electrons. In a metal we have nuclei screened by the core electrons and free electrons that move around. On average, the system will be neutral, but when the electron beam interacts with the free-electron sea, sometimes there will be a charge separation between the free electrons and the positively charged nuclei. Because we have a charge separation, there will be an electrostatic force acting between the electrons and

the nuclei. Since the nuclei are stationary and the electrons are so much lighter, they will start moving towards the nuclei, gaining kinetic energy and reaching a maximum as they pass them, and then will be slowed down, caught again by the electrostatic force and move back towards the nuclei. This exchange between the electrostatic Coulomb force and the kinetic energy is what we call plasma oscillations. Just like photons are the quanta of electromagnetic oscillations, plasmons are the quanta of plasma oscillations.

Ionization damage and radiolysis Inelastic excitations may lead to damage especially in molecules and organic materials in a phenomenon called radiolysis. Radiolysis is a process where an excited state can be converted to momentum and directly break bonds. While in inorganic solids such as hexagonal boron nitride (hBN) and molybdenum disulfide (MoS_2), direct radiolysis is not possible, a covalently bound atom may be easier displaced if the excitonic relaxation time is long enough to weaken the chemical bonds and lower its displacement threshold energy [74]. By contrast, in pristine graphene, electronic excitations reach the ground state before any changes in the structure may occur. Graphene is one of the most studied 2D materials and its ionization lifetimes have been well characterized: holes in the valence band are neutralized within 10^{-15} s and core holes within 10^{-14} s, whereas collective excitations such as plasmons are damped within 10^{-13} s and phonons in 10^{-12} s [75–77]. In a STEM with a typical electron dose rate of 10^{9} $e^{-}s^{-1}$, a single electron will interact with the sample every 10^{-9} s, so ionization damage is unlikely to happen since the electron will always find the sample in the ground state, as experiments also seem to show [24]. On the other hand, excitation lifetimes in MoS_2 and hBN are much longer, 10^{-12} s for MoS_2 and even longer 10^{-9} s for hBN [77–79], which increases the possibility of ionization damage. While excitation effects may indirectly contribute to damage due to weakening or breaking of chemical bonds, the most prominent and direct damage mechanism in 2D materials is caused by the elastic interactions between electrons and atoms that leads to knock-on damage. The mechanisms of this process can be studied via molecular dynamics simulations.

1.6 Molecular dynamics

Molecular dynamics (MD) is a computational method used to study many-body condensed matter systems and biomolecular congregations. The aim of MD is to give insight into atomic processes and validate experimental observations, bridging the gap between the macroscopic world and the microscopic length and time scales. There are two major types of simulations for many-body systems, stochastic and deterministic, which are covered by the Monte Carlo (MC) and the MD methods, respectively. Monte Carlo explores configurations by trial moves of atoms as a result of random perturbations to the system (see Section 1.8) but does not provide information on the time evolution of the system [80]. Molecular dynamics simulations on the other hand can study the temporal evolution of a given system.

We can distinguish between three types of MD in terms of the amount of empirical input and accuracy: classical, semi-ab-initio and ab-initio MD. We will concentrate on what they all have in common: all consist of the step-by-step numerical solution of classical equations of motion [81] [82], which in the Newton formalism are

$$m_i \ddot{\mathbf{r}}_i = \mathbf{f}_i \quad \text{and} \quad \mathbf{f}_i = -\frac{\partial}{\partial \mathbf{r}_i} U\left(\mathbf{r}^N\right), \tag{1.4}$$

where $\mathbf{f}_i$ is the force acting on atom i with mass m_i, which is derived from the potential energy $U\left(\mathbf{r}^N\right)$, where $\mathbf{r}^N = (\mathbf{r}_1,\ \mathbf{r}_2, ...\mathbf{r}_N)$ represents the complete set of $3N$ atomic coordinates.

For classical MD and semi-ab-initio calculations, the part of the potential energy U from interactions between atoms in the same molecule and those in other molecules is commonly split into one-body, two-body, and three-body terms with the form:

$$U(\mathbf{r}^N) = \sum_i u\left(\mathbf{r}_i\right) + \sum_i \sum_{j>i} v\left(\mathbf{r}_i, \mathbf{r}_j\right) + \sum_i \sum_{j,k>i} v\left(\mathbf{r}_i, \mathbf{r}_j, \mathbf{r}_k\right) + \ldots\ . \tag{1.5}$$

The term $u\left(\mathbf{r}\right)$ represents an externally applied potential field, and it is common to focus on the pair potential $v\left(\mathbf{r}_i, \mathbf{r}_j\right)$. The most commonly used form of pair potential is the Lennard-Jones two-body potential

$$v^{LJ} = 4\epsilon \left[\left(\frac{\sigma}{r}\right)^{12} - \left(\frac{\sigma}{r}\right)^{6} \right], \tag{1.6}$$

which is used to describe the interaction between a pair of neutral atoms or molecules. One

parameter, ϵ, is the depth of the potential well, which describes the region surrounding the lowest potential energy point. σ describes the distance where the particle-particle interaction is null, while r is the distance between the particles. The r^{-12} term stands for the repulsion at short ranges between the particles caused by the overlapping of electron orbitals [83], and the r^{-6} term accounts for the long-range attraction. This potential was used in the earliest studies and gave a very good approximation on the equilibrium state of argon [84]. Having defined the potential energy function $U\left(\mathbf{r}^N\right)$, the atomic forces can be calculated using Eq. 1.4. For simplicity, we can describe a structure composed of atoms with potential energy $U\left(\mathbf{r}^N\right)$ and coordinates $\mathbf{r}^N = (\mathbf{r}_1,\ \mathbf{r}_2, ...\mathbf{r}_N)$ also in terms of kinetic energy $K\left(\mathbf{p}^N\right) = \sum_{i=1}^{N} \mid \mathbf{p}_i \mid^2 /2m_i$ with atomic momenta $\mathbf{p}^N = (\mathbf{p}_1,\ \mathbf{p}_2, ...\mathbf{p}_N)$. The total energy or the Hamiltonian can be written as the sum of the kinetic and potential energy $H = K + U$. Now if we write the classical equations of motion as

$$\dot{\mathbf{r}}_i = \dot{\mathbf{p}}_i/m_i \quad \text{and} \quad \dot{\mathbf{p}}_i = \mathbf{f}_i, \tag{1.7}$$

we get a system of coupled ordinary differential equations. These equations need to be numerically integrated step-by-step by the MD algorithm. The integration time step δt must not be too large, since this may produce inaccurate results. A good example of an algorithm which allows the use of longer timesteps without putting the accuracy of the simulations at risk is the 'velocity Verlet' algorithm [85]. The main attributes of the Verlet algorithm are that it is time reversible, it requires just one force evaluation per step, and it is easy to program. Concerning MD, the main ingredients needed to start are:

- a model to describe the interaction between atoms, molecules etc;
- a integrator that shifts particle positions and velocities from time t to $t + \delta t$;
- a microcanonical ensemble (NVE),

where a NVE is an isolated statistical system of particles N where the energy conservation does not change with time. These three essential quantities define a MD simulation. The ab-initio MD method will be introduced in detail in the next section.

1.7 Ab-initio molecular dynamics

1.7.1 Many-body problem

The "ab-initio" method, in latin "from beginning", is a theoretical approach to finding solutions to the equation that describes the quantum behaviour of atoms, the Schrödinger equation. In a many-body system, electrostatic interactions between the particles, such as the electron-electron repulsion, electron-nuclei attraction and nuclei-nuclei repulsion, need to be accounted for. The non-relativistic, time-independent Schrödinger equation can describe such a system as

$$\hat{H}\psi\left(r_i, R_i\right) = E\psi\left(r_i, R_i\right), \tag{1.8}$$

where E is the total energy of the system and $\psi\left(r_i, R_i\right)$ the wave function dependent on the positions of the electrons and nuclei r_i and R_i, respectively. In the absence of external fields, the Hamiltonian operator $\hat{H}$, which contains information regarding the kinetic and potential energies of all the particles in the system, takes the form

$$\hat{H} = T_{\mathrm{e}} + T_{\mathrm{n}} + V_{\mathrm{e-n}} + V_{\mathrm{e-e}} + V_{\mathrm{n-n}}, \tag{1.9}$$

where T_{e} is the kinetic energy of the electrons, T_{n} the kinetic energy of the nuclei, $V_{\mathrm{e-n}}$ the Coulomb attraction between electrons and nuclei, $V_{\mathrm{e-e}}$ the Coulomb repulsion between electrons, and $V_{\mathrm{n-n}}$ the Coulomb repulsion interaction between the nuclei. The terms in Eq. 1.9 can be written as

$$\hat{H} = -\frac{1}{2}\sum_{i=1}^{N}\nabla_i^2 - \frac{1}{2}\sum_{A=1}^{M}\frac{1}{M_A}\nabla_A^2 - \sum_{i=1}^{N}\sum_{A=1}^{M}\frac{Z_A}{r_{iA}} + \sum_{i=1}^{N}\sum_{j>1}^{N}\frac{1}{r_{ij}} + \sum_{A=1}^{M}\sum_{B>A}^{M}\frac{Z_A Z_B}{R_{AB}}. \tag{1.10}$$

For simplicity the Hamiltonian in Eq. 1.10 is shown in atomic units, where the mass of the electron m_{e}, the charge e, the reduced Planck's constant $\hbar$ and the permitivitty of free space $4\pi\epsilon_0$ are all set to unity. M_A is the mass of nucleus A and Z_{A} its charge. The indices in the summation

terms i and j run over the N electrons, and the indices A and B run over the M nuclei of the system. The first two terms represent the kinetic energy of the electrons and nuclei, respectively, while the other three are potential energy terms. These arise from the electrostatic interaction between the nuclei and electrons, the repulsive electron-electron and nucleus-nucleus interations in this particular order as seen in Eq. 1.10. r represents the distance between an electron and another particle, be it an electron or a nucleus, while R_{AB} represents the distances between the nuclei.

It is quite difficult to try and find a solution which takes into account all these interactions, as we need to consider the interaction contribution of all the electrons and nuclei simultaneously. However, an important simplification of this problem can be obtained by the simple observation of the difference between the mass of an electron and that of a given nucleus. The electrons are three orders of magnitude lighter than nuclei, and as a consequence, they travel three orders of magnitude faster than the nuclei given the same amount of kinetic energy. In other words, to the electrons it appears as if the nuclei are fixed in place, while to the nuclei, the positions of the electrons appear to update instantaneously to their every move. As a result, the system can be simplified by separating the electronic from the nuclear motion, and look for solutions of the wave function in the form

$$\psi\left(r_i, R_i\right) = x\left(R_i\right)\psi\left(r_i\right), \tag{1.11}$$

where $x\left(R_i\right)$ and $\psi\left(r_i\right)$ are the nuclear and electronic wave functions. This simplification is known as the Born-Oppenheimer approximation [86]. Under this approximation, the kinetic energy term of the nuclei becomes 0, as the nuclei are not allowed to move, and thus the potential energy term describing the nuclei-nuclei repulsion becomes a constant. If we only focus on the electronic part of the problem, the Hamiltonian will take the form

$$\hat{H}_{\mathrm{elec}} = -\frac{1}{2}\sum_{i=1}^{N}\nabla_i^2 - \sum_{i=1}^{N}\sum_{A=1}^{M}\frac{Z_A}{r_{iA}} + \sum_{i=1}^{N}\sum_{j>1}^{N}\frac{1}{r_{ij}}, \tag{1.12}$$

and now the Schrödinger equation for the electronic part, where the electronic wave function Ψ_{elec}

depends only on the electron spatial coordinates, becomes

$$\hat{H}_{\text{elec}}\psi\left(\vec{r}_i,...,\vec{r}_N\right)=E_{\text{elec}}\psi\left(\vec{r}_i,...,\vec{r_N}\right), \tag{1.13}$$

where E_{elec} are eigenvalues. The wave function solution for this system that gives the lowest energy is called the ground state, and the eigenvalue of the ground state is called the ground-state energy.

However, it is still not easy to get a solution for the ground-state energy, mainly because of the electron-electron repulsion term in Eq. 1.12, since each electron simultaneously experiences an electrostatic repulsion due to the presence of every other electron in the system. It is worth mentioning that the wave function itself cannot be directly observed. What can be instead measured is the probability density that N electrons are at a set of coordinates $r_1, r_2...r_N$,

$$|\psi\left(r_1,...r_N\right)|^2=\psi^*\left(r_1,...r_N\right)\psi\left(r_1,...r_N\right), \tag{1.14}$$

where the asterisk denotes a complex conjugate. However, the wave function is still a function of $3N$ coordinates. For a C atom, which has 6 electrons, the wave function would be a function of 18 dimensions (3×6 electrons). Given the fact that there is no way of distinguishing between the electrons, the wave function $\psi\left(\vec{r}_i,...,\vec{r}_N\right)$ can be approximated as a product of *N* single-electron wave functions, also called the Hartree product, to overcome the dimensional obstacle:

$$\psi\left(\vec{r}_i,...,\vec{r}_N\right)\approx\psi_1\left(\vec{r}\right)\psi_2\left(\vec{r}\right)...\psi_N\left(\vec{r}\right). \tag{1.15}$$

Now we can calculate the electron density by counting how many electrons will on average be found at position $\vec{r}$ by summing over all the probabilities that an electron in the wave function $\psi_i\left(\vec{r}\right)$ will be located at the position $\vec{r}$:

$$n\left(\vec{r}\right)=2\sum_i^N\psi_i^*\left(\vec{r}\right)\psi_i\left(\vec{r}\right), \tag{1.16}$$

where the factor 2 is a consequence of the electrons having spin and of the Pauli exclusion principle, which states that two electrons occupying an orbital must have opposite spin. The electron density is a function of only three spatial coordinates compared to 3N coordinates of the wave function. In the next section we will discuss how we can use the electron density to obtain solutions to the Schrödinger equation.

1.7.2 Density functional theory

Density functional theory (DFT) rests on two theorems proved by Hohenberg and Kohn [87], and on a set of equations by Kohn and Sham [88]. The first theorem states that the ground-state energy E_0 is a unique functional of the ground-state electron density $n_0(\vec{r})$:

$$E[n_0(\vec{r})] = E_0. \tag{1.17}$$

The second theorem states that the ground-state energy can be obtained variationally. The functional that delivers the ground-state energy of the system can only deliver the lowest energy if the input density is the true ground-state electron density corresponding to the solution of the Schrödinger equation.

Kohn and Sham proved that the right electron density can be found by a set of equations, which only involve single electrons ψ_i [88]:

$$\left[\frac{1}{2}\nabla + V(\vec{r}) + V_H(\vec{r}) + V_{xc}(\vec{r})\right]\psi_i(\vec{r}) = \epsilon_i\psi_i(\vec{r}), \tag{1.18}$$

where the first term is the kinetic energy of the electron, the second term $V(\vec{r})$ defines the potential due to the electron interaction with the nuclei, $V_H(\vec{r})$ is the Hartree potential that describes the Coulomb repulsion between the electron and the electron density of all the other electrons in the system, and $V_{xc}(\vec{r})$ is an exchange-correlation potential that accounts for the Pauli repulsion and for how much the movement of one electron is influenced by the presence of all other electrons.

To solve the Kohn-Sham equations, the Hartree potential needs to be defined, and that requires knowing the electron density. However, the electron density can only be found if we know the

single-electron wave functions, and that means we have to solve the Kohn-Sham equation. This problem can be treated iteratively in the following way:

1. Define an initial, trial electron density $n(\vec{r})$.
2. Find the single-electron wave functions $\psi_i(\vec{r})$ by solving the Kohn-Sham (KS) equations using the trial electron density.
3. Calculate the electron density using the Kohn-Sham single-electron wave functions from step 2, $n_{\mathrm{KS}}(\vec{r}) = 2\sum_i \psi_i^*(\vec{r})\,\psi_i(\vec{r})$.
4. Compare the trial density $n(\vec{r})$ with the calculated electron density $n_{\mathrm{KS}}(\vec{r})$ and if they are equal, the ground state electron density has been found and the total energy can be calculated. If they differ, then the trial density needs to be updated and the process starts again at step 2.

A convenient aspect of DFT is that all the energy terms that can't be explicitly expressed are accounted for in the exchange-correlation potential $V_{xc}(\vec{r})$. Therefore, also the accuracy of the ground state energy depends on how well $V_{xc}(\vec{r})$ is approximated. The true form of the exchange-correlation functional is not generally known, though it can be derived exactly for the uniform electron gas, where the positive charges are uniformly distributed and so the electron density is a uniform quantity at any point in space, $n(\vec{r}) = \mathrm{const}$. This way the exchange-correlation potential at any position is known from the electron density at that position:

$$V_{xc}(\vec{r}) = V_{xc}^{\text{electron gas}}[n(\vec{r})]\,. \tag{1.19}$$

This is called the local density approximation (LDA) and it gives us a way to solve the KS equations, though it is an approximation that is not the true exchange-correlation and will not deliver the true solution to the Schrödinger equation in general. Another way to define the exchange-correlation functional is the generalized gradient approximation (GGA), which uses not only the local electron density but also the local gradient in the electron density, such as the Perdew-Wang (PW91) [89] or the Perdew-Burke-Ernzerhof (PBE) [90] functionals, which are commonly used for calculations involving solids. Despite its approximate nature, DFT provides a remarkably good description of most properties of many materials.

1.7.3 Density-functional tight-binding

While DFT calculations are often the most reliable point of reference for experiments, they are computationally expensive and slow for the purpose of describing large systems (hundreds of atoms) or for stochastic experiments. The density-functional based tight-binding (DFTB) method scales better for larger systems since the computational effort can be dramatically reduced, while maintaining reasonable accuracy [91–93]. DFTB is not an *ab-initio* method, since it is parametrized and the fundamental starting point is that the electrons are "tightly bound", which limits the complexity of their interaction, but is well suited to describe covalently bonded carbon structures [91, 94]. DFTB is based on a second-order Taylor-series expansion of the Kohn-Sham total energy (Eq. 1.17) in DFT. Instead of finding the electron density $n(\vec{r})$ that minimizes the energy, a reference density $n^0(\vec{r})$ is assumed and perturbed with some fluctuations:

$$n(\vec{r}) = n^0(\vec{r}) + \delta n(\vec{r}). \tag{1.20}$$

The total energy is expanded into a Taylor series up to the third term as

$$E[n^0(\vec{r}) + \delta n(\vec{r})] = E^0[n^0(\vec{r})] + E^1[n^0(\vec{r}), \delta n(\vec{r})] + E^2[n^0(\vec{r}), (\delta n(\vec{r}))^2] + E^3[n^0(\vec{r}), (\delta n(\vec{r}))^3], \tag{1.21}$$

where the first two terms contribute to the non-self-consistent DFTB method [91, 92], and the rest to so-called self-consistent charge (SCC) DFTB [93, 95] methods.

1.8 Monte Carlo method

Monte Carlo methods are computational algorithms that are based on repeated random sampling to obtain results. Within the Metropolis algorithm [96], the atomic configuration is tested by trial moves of particles, and the energy change from one step to the other is used as a trigger to accept or reject the new configuration. In material science, these methods can be applied to model the dynamic behaviour of atoms and are commonly called kinetic Monte Carlo (KMC). KMC is considered as a form of coarse graining in the context of molecular dynamics, since it bridges the motion of individual atoms occuring on a pico- to femtosecond timescale with events that may require even seconds to occur within an ensemble of multiple possible processes [97]. In KMC

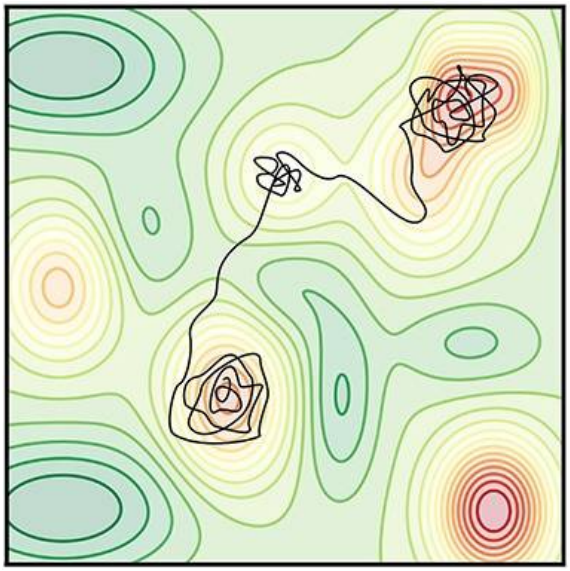

Figure 1.14: A typical kinetic Monte Carlo MD trajectory (black) on a potential energy surface, with red regions representing lower energy basins. Figure adapted from Ref. [97] (CC-BY).

all transitions are Poisson-distributed, independent of the system's history, and only high-barrier events are of interest (e.g. atom jumps, adsorption and desorption). In Fig. 1.14 we see a possible MD trajectory (black) of an atom on a potential energy surface (PES), where the red regions represent the system's lower energy basins. After many random trials, the atom finds a route to escape to the next basin. Most transitions are filled with time spent around PES minima, as the event-relevant transitions only occur occasionally.

Originally the KMC method was used to study vacancy diffusion in alloys [98], but it can be used for predicting surface diffusion, dislocation mobility [99] and other phenomena. In this study it is used to study the diffusion of N adatoms near the graphene vacancy.

Chapter 2

Methods

Here, we introduce the concept of the displacement cross section used for quantifying knock-on displacements caused by electron irradiation. We compare static and non-static models, and show how to account for the effects of atomic vibrations in the cross-section calculations. Further, we describe the acquisition of the experimental data with STEM and introduce the computational tools used to model atom displacements in materials under the electron beam.

2.1 Predicting the displacement cross section

To predict and quantify the damage created through electron irradiation, we calculate the displacement cross section σ. Conceptually the displacement cross section is the effective area of collisions that will lead to the displacement of an atom and is measured in units of barn (10^{-28} m^2). The elastic scattering of a relativistic electron by a nucleus was first derived by N. Mott [19] as a solution to the Dirac equation [100], since Dirac was the first to account for special relativity in the context of quantum mechanics. McKinley and Feschbach built on Mott's work [20], providing an analytical solution to describe cross sections for elements up to a medium Z:

$$\sigma = \sigma_{\mathrm{R}} \left[1 - \beta^2 \sin^2 \theta/2 + \pi Z \alpha \beta \sin \theta/2 \left(1 - \sin \theta/2\right)\right], \tag{2.1}$$

where θ is the electron scattering angle, Z is the atomic number, α is the fine structure constant, and $\beta = v/c$ is the ratio of the electron velocity with the speed of light. We can express β in

terms of the acceleration voltage as

$$\beta = \sqrt{1 - \frac{1}{\left(E_\mathrm{e}/mc^2 + 1\right)^2}}, \tag{2.2}$$

where $E_\mathrm{e}\,(= E_\mathrm{kin})$ is the acceleration voltage. In Eq. 2.1, σ_R is the classical Rutherford scattering cross-section

$$\sigma_\mathrm{R} = \left(\frac{Ze^2}{4\pi\epsilon_0 2mc^2}\right)^2 \frac{1-\beta^2}{\beta^4}\csc^4(\theta/2), \tag{2.3}$$

where ϵ_0 is the vacuum permittivity, e the electron charge and m the mass of the electron. To obtain the total displacement cross section, one needs to integrate Eq. 2.1 over all possible electron scattering angles θ for which the transferred energy to the nucleus $\tilde{E}_\mathrm{n}$ is higher than its displacement threshold energy E_d. In the static approximation, where the atoms are assumed to be stationary, the integral is:

$$\sigma_\mathrm{static} = \int_{\theta=0}^{\theta=\pi} \mathcal{H}\left(\tilde{E}_\mathrm{n}\left(E_\mathrm{e},\theta\right) - E_\mathrm{d}\right)\,\sigma\left(E_\mathrm{e},\theta\right)\mathrm{d}\theta. \tag{2.4}$$

We are using the Heaviside step function $\mathcal{H}$, which can take the values 1 or 0 depending on whether or not the transferred energy $\tilde{E}_\mathrm{n}\left(E_\mathrm{e},\theta\right)$, as in Eq. 3.18, exceeds the displacement threshold energy E_d. The highest energy transfer occurs when the electron backscatters at $\theta = \pi$ (see Eq. 3.18).

Vibration-assisted displacement cross section

In the non-static approach discussed in [22, 24, 25], the out-of-plane velocity v_z of the target atom is included as a parameter to the transferred energy in addition to the electron scattering angle θ. Essentially this is due to the fact that if an atom happens to vibrate along the direction of the electron beam, the energy transfer will be higher than if it was at rest. In any real material the atoms will never be at rest due to thermal vibrations. Meyer et al. [22] calculated the out-of-plane velocities for graphene in the framework of the Debye model to be able to match the experimentally observed displacement cross sections of graphene at voltages under 100 keV. This method was

further improved by Susi et al. [24], by using the phonon density of states to also account for quantum mechanical zero-point vibrations from first principles. The probability to find an atom vibrating at a certain velocity can be expressed in terms of a normal distribution:

$$P(v_z, \overline{v_z^2}) = \frac{1}{\sqrt{2\pi\overline{v_z^2}}} \exp\left(\frac{-v_z^2}{2\overline{v_z^2}}\right), \tag{2.5}$$

where the mean-squared velocity $\overline{v_z^2}$ is the variance. For example, an electron beam of 100 keV can only transfer 20.05 eV to a C atom at rest, whereas if the atom is vibrating at a velocity equivalent to three times the standard deviation (square root of the variance) of the velocity distribution Eq. 2.5 it will transfer 24 eV, which is almost 4 eV more (the formulas will be given in Sec. 3.1.2). While this boost in energy transfer may be negligible for acceleration voltages above 120 keV, it will make a decisive difference when operating the electron microscope around or below the displacement threshold limit.

To estimate the total cross section, we now integrate over all possible velocity combinations as in Ref. [25]:

$$\sigma_{\mathrm{v_z}} = \int_{-v_{\mathrm{z}}^{\max}}^{v_{\mathrm{z}}^{\max}} \int_{\theta=0}^{\theta=\pi} P(v_z, \overline{v_z^2}) \mathcal{H}\left(\tilde{E}_{\mathrm{n}}\left(E_{\mathrm{e}}, v_{\mathrm{z}}, \theta\right) - E_{\mathrm{d}}\right) \sigma\left(E_{\mathrm{e}}, \theta\right) \mathrm{d}v_{\mathrm{z}} \mathrm{d}\theta. \tag{2.6}$$

To date, vibrations have only been treated in the out-of-plane direction. However, if we want to quantify the emission of atoms in arbitrary directions or describe events such as the in-plane pyridinic N jump, we need to be able to account for vibrations and emission to arbitrary directions and limit the cross-section to an angular sector of interest, as will be discussed in Sec. 3.2.

2.1.1 Atomic mean-square velocities

Atomic vibrations of the lattice are caused by the excitation of phonons. Here, they are described by normal distributions of in- and out-of-plane velocities distinguished by their mean-square widths $\overline{v^2}_{xyz}$. The widths were derived from the phonon density of states thanks to our collaborators Nicholas A. Pike and Matthieu J. Verstraete (see Supplemental information of Ref. [57]). Briefly, the phonon dispersion is calculated, a displacement-weighted phonon density of states is con-

structed for each atom using Gaussian smearing of 0.6 meV, and populated with Bose-Einstein thermal factors at 300 K. In the end, within a harmonic model, the mean-square velocity is related directly to the mean-square displacement by the mode frequency [27].

2.2 Analysis of experimental cross-section data

To quantify electron beam-induced effects, we need to estimate the experimental displacement cross section. Commercial monolayer graphene (Easy Transfer, Graphenea) and CVD-grown samples were used to determine the cross sections of graphene [24] and graphene with impurities. The graphene samples that had Si impurity atoms, were synthesized by CVD on 25μm thick Cu foils in a furnace made out of quartz. The Cu foils are annealed for $<$ 1h under constant CH_4 methane and Ar/H_2 flow at 960° and a pressure of 10 mbar. During this process the C atoms from methane recombine on the Cu foil to form graphene. In the end, the graphene is transferred onto holey amorphous carbon on a TEM support grid. The exact origins of the Si impurities is not known, but are believed to be either introduced during the annealing process, since the furnace is made of quartz, but may also stem from the transfer process [51, 64] as Si is one of the most abundant elements on earth and present in laboratory glasswear. While N impurities may be purposefully introduced in the graphene lattice, in our case they are also incidental.

The experimental data was acquired by colleagues scanning over specified areas using the Nion UltraSTEM100 scanning transmission electron microscope and recording images with a probe convergence semi-angle of 30 mrad and a medium-angle annular dark-field detector with a semi-angular range of 80–200 mrad [24]. The identity of the Si and N impurities was determined by electron energy-loss spectroscopy [101]. The electron beam was usually scanned across fields of view of 1×1 or $2\times2\ \mathrm{nm}^2$. Whenever a jump or a displacement event is observed, the accumulated areal dose ($e^-/$ Å^2) was calculated based on a nominal beam current of 30 pA and the number of continuous frames between events and their acquisition times. The ocurrence of one event does not affect the probability that another one will happen, and thus we consider the doses to be Poisson-distributed. The expectation value of the corresponding exponential distribution can be fitted as we will see later (Fig. 3.10) and the experimental cross-section evaluated as

$$\sigma_{\mathrm{exp}} = \frac{1}{\lambda}, \tag{2.7}$$

where λ is the expectation value of the Poisson distribution (in units of Å^{-2}).

2.3 Displacement simulations

To test the 3D model for vibration-assisted knock-on damage presented in Sec. 3.1.2 and Sec. 3.2, we ran DFT/MD simulations that allowed us to predict the displacement threshold energy $E_{\mathrm{d}}(\gamma, \delta)$ of atoms for the beam-induced dynamics observed experimentally in pristine graphene [24], graphene with Si impurities [27] and graphene with a pyridinic N site [28, 57].

For the purpose of setting up and conducting the displacement simulations, we used GPAW [102], a density functional theory code based on the projector-augmented wave (PAW) method [103, 104], with MD as implemented within the atomic simulation environment (ASE) [105]. ASE is a front-end software package for molecular dynamics also written in the Python programming language that uses the NumPy library [106] to perform simulation tasks; one can set up, perform and analyze simulations in ASE. Before we start the displacement simulations we need to set up a cell of atoms. We use the *Atoms* object in ASE to create a system of two carbon (C) atoms, set the distance between them and define the unit cell vector. We perform cell relaxation by minimizing the potential energy of the system and the inter-atomic forces while optimizing the overall geometry including the size of the cell. Once the unit cell structure is relaxed, we create a graphene supercell and start the DFT/MD simulations to determine the displacement threshold energy for the three systems mentioned above.

For *pristine graphene* we used ASE for Velocity-Verlet dynamics with a timestep of 0.3 fs in a 7×7×1 graphene supercell, with forces from a GPAW DFT calculator using the PBE [90] functional, a *dzp* basis-set, a 3×3×1 Monkhorst-Pack **k**-point grid, and a Fermi-Dirac smearing of 0.025 eV. For the *graphene with a Si impurity* and graphene with a *pyridinic N–C_2* site we used a 6×6×1 graphene supercell with a Si impurity located in the middle of the cell or a structure similar to a single vacancy but with the dangling-bond C atom replaced by N bonding to two C neighbors and stabilizing the defect, respectively. To model what happens in STEM experiments, where the incoming electron beam is perpendicular to the graphene sheet, we transfer momentum to a C atom, describing the kick it would receive from an elastic electron scattering event. We loop over a range of energies and atom emission angles until our stopping criteria is reached as will be

discussed in Chapter 3. A code example is provided in Appendix A.4 for displacement simulations on pristine graphene. The simulations for Si–C and N–C_2 are done in a similar fashion, since only the stopping criteria are different.

2.4 Temperature-dependent displacement simulations

We additionally used density-functional tight-binding (DFTB)-based MD to predict the displacement threshold of the Si-C and the pyridinic N systems at a temperature of 300 K. We opted for DFTB since it scales better computationally for the large cells and for gathering statistics. We used the non-self-consistent and non-spin-polarized DFTB+ calculator [107] and employed the "pbc-0-3" parameter set [108]. To thermalize the systems, we used the Maxwell-Boltzmann distribution with kinetic energies corresponding to 600 K as seen in Appendix A.2. Half of this energy goes into the potential energy of the atoms and the other half to their kinetic energy, hence resulting in a temperature of 300 K. The DFTB+ calculator runs for several thousand timesteps and one can save different thermalized states as a trajectory file, where information on positions, velocities and forces of all the atoms in the structure is contained. These configurations are then used to perform displacement simulations as discussed in Section 3.6. The same method was used to study the displacement threshold energy of pristine graphene at various temperatures by Chirita et al. [25].

Chapter 3

Results

In this chapter, we derive the 3D theoretical framework used to predict electron beam-induced dynamics that accounts for atomic vibrations in- and out-of-plane. We start from the energy and momentum conservation and derive a 3D formula to predict the transferred energy resulting from the elastic scattering of an electron to an atom. We introduce a method to describe the displacement cross section, which considers the atom velocities at the moment of impact and accounts for the anisotropy of the displacement threshold energy. This anisotropy is evaluated by DFT/MD simulations and used to predict displacement cross sections in an attempt to bridge the gap between theory and experimental observations.

3.1 Derivation of the 3D electron-atom elastic interaction

3.1.1 Basic notions of relativity

Before we dive deeper into how to derive the 3D model for the electron energy transfer, it is important to cover some notions of relativity, since the electron accelerated to TEM energies is a relativistic particle. The fraction of the speed of light c at which a relativistic particle with velocity v moves is denoted by

$$\beta = \frac{v}{c}. \tag{3.1}$$

The relativistic total energy E_{tot} is expressed as the sum of the kinetic E_{kin} and rest energies E_{rest}

of the particle:

$$E_{\text{tot}} = E_{\text{kin}} + E_{\text{rest}} = \gamma mc^2 \tag{3.2}$$

$$E_{\text{kin}} + mc^2 = \gamma mc^2 \tag{3.3}$$

$$E_{\text{kin}} = (\gamma - 1)\, mc^2 \tag{3.4}$$

$$\gamma = E_{\text{kin}}/mc^2 + 1, \tag{3.5}$$

where m is the mass of the particle and γ is known as the Lorentz factor, which quantifies the change in properties of a particle moving close to the speed of light (relativistic speeds):

$$\gamma = \frac{1}{\sqrt{1-\beta^2}}. \tag{3.6}$$

We can also recover Eq. 2.2 by substituting Eq. 3.5 in Eq. 3.6. At this point it is worth mentioning that for $v << c$ (e.g. atoms), the binomial expansion of γ gives

$$\gamma = 1 + \frac{v^2}{2c^2} \quad \rightarrow \quad \gamma - 1 = \frac{v^2}{2c^2}, \tag{3.7}$$

which leads to the classical expression:

$$E_{\text{kin}} = \frac{v^2}{2\cancel{c^2}} m\cancel{c^2} = \frac{mv^2}{2}. \tag{3.8}$$

The relativistic energy-momentum relation, also called the dispersion relation, can be derived from the expression of the effective mass:

$$m = \gamma m_0 \quad \rightarrow \quad m = \frac{m_0}{\sqrt{1-\frac{v^2}{c^2}}}, \tag{3.9}$$

where m_0 is the rest mass of the particle. We next square the expression, bring it to the same

denominator and then multiply by c^4:

$$m^2 - \frac{m^2 v^2}{c^2} = m_0^2 \quad \rightarrow \quad m^2 c^4 - m^2 v^2 c^2 = m_0^2 c^4 \tag{3.10}$$

$$m^2 c^4 = m_0^2 c^4 + m^2 v^2 c^2. \tag{3.11}$$

The momentum is the product of mass times velocity, $p = mv$, and the total energy is $E = mc^2$. Using these two identities we end up with

$$E^2 = \left(E_{\mathrm{kin}} + m_0 c^2\right)^2 = m_0^2 c^4 + p^2 c^2, \tag{3.12}$$

which is an important relation that will be used in the energy and momentum conservation equations presented in the next section.

3.1.2 3D energy and momentum conservation

To derive a three-dimensional model for the electron-atom energy transfer, we consider the electron as a relativistic projectile scattering from a moving, non-relativistic target, the nucleus, in a Cartesian coordinate system. Our goal is to determine the amount of kinetic energy transferred to the atom after scattering. Since this is an elastic scattering event, the total energy and momentum of the system will be conserved:

$$E_{\mathrm{e}} + E_{\mathrm{n}} = \tilde{E}_{\mathrm{e}} + \tilde{E}_{\mathrm{n}}, \tag{3.13}$$

$$\mathbf{p}_{\mathrm{e}} + \mathbf{p}_{\mathrm{n}} = \tilde{\mathbf{p}}_{\mathrm{e}} + \tilde{\mathbf{p}}_{\mathrm{n}}, \tag{3.14}$$

where the quantities $\tilde{E}_{\mathrm{e}}$, $\tilde{E}_{\mathrm{n}}$ and $\tilde{\mathbf{p}}_{\mathrm{e}}$, $\tilde{\mathbf{p}}_{\mathrm{n}}$ represent the total energies and momenta after the collision of the electron and nucleus, respectively. We can use the dispersion relation derived in Eq. 3.12

with $E_{\mathrm{kin}} = E_e$ to express $\tilde{\mathbf{p}}_{\mathrm{e}}$ as

$$|\tilde{\mathbf{p}}_{\mathrm{e}}| = \sqrt{\tilde{E}_{\mathrm{e}}\left(\tilde{E}_{\mathrm{e}} + 2mc^2\right)/c^2} = \sqrt{\left(E_{\mathrm{e}} + E_{\mathrm{n}} - \tilde{E}_{\mathrm{n}}\right)\left(\left(E_{\mathrm{e}} + E_{\mathrm{n}} - \tilde{E}_{\mathrm{n}}\right) + 2mc^2\right)/c^2}, \quad (3.15)$$

where c is the speed of light and m the rest mass of the electron. At this point, to reach an analytic solution we make the approximation $E_{\mathrm{e}} + E_{\mathrm{n}} - \tilde{E}_{\mathrm{n}} \approx E_{\mathrm{e}}$, since the energy of the electron (e.g. $E_{\mathrm{e}} = 90$ keV) is much higher than that of the nucleus before or even after the collision (e.g. for $^{12}\mathrm{C}$, $E_{\mathrm{n}} \approx 25$ meV and $\tilde{E}_{\mathrm{n}} \approx 10$ eV). The amount of energy that the electron loses due to the interaction with the atom is negligible and so we can approximate $|\mathbf{p}_{\mathrm{e}}| \approx |\tilde{\mathbf{p}}_{\mathrm{e}}|$, which will deliver an analytical solution [25].

After decomposing the momentum vectors in terms of their magnitude and direction (e.g. $\mathbf{p}_{\mathrm{e}} = p_{\mathrm{e}}\hat{\mathbf{p}}_{\mathrm{e}}$, $\mathbf{p}_{\mathrm{n}} = p_{\mathrm{n}}\hat{\mathbf{p}}_{\mathrm{n}}$) and using Eq. 3.15, we rewrite the momentum conservation equation as

$$\sqrt{E_{\mathrm{e}}\left(E_{\mathrm{e}} + 2mc^2\right)/c^2}\ \hat{\mathbf{p}}_{\mathrm{e}} + \sqrt{2ME_{\mathrm{n}}}\ \hat{\mathbf{p}}_{\mathrm{n}} = \sqrt{E_{\mathrm{e}}\left(E_{\mathrm{e}} + 2mc^2\right)/c^2}\ \hat{\tilde{\mathbf{p}}}_{\mathrm{e}} + \sqrt{2M\tilde{E}_{\mathrm{n}}}\ \hat{\tilde{\mathbf{p}}}_{\mathrm{n}}, \quad (3.16)$$

where $\hat{\mathbf{p}}_{\mathrm{e,n}}$ and $\hat{\tilde{\mathbf{p}}}_{\mathrm{e,n}}$ are vectors of unit length that give the direction of the electron and atom before and after the collision, respectively. We denote $|\mathbf{p}_{\mathrm{e}}| = p_{\mathrm{e}} = \sqrt{E_{\mathrm{e}}\left(E_{\mathrm{e}} + 2mc^2\right)/c^2}$ and $|\mathbf{p}_{\mathrm{n}}| = p_{\mathrm{n}} = \sqrt{2ME_{\mathrm{n}}} = Mv$ for brevity, where M is the mass of the nucleus. Our goal is to determine the energy of the nucleus after the collision, $\tilde{E}_{\mathrm{n}}$. Shifting the third term to the left side of Eq. 3.16 and then squaring results in

$$|\tilde{E}_{\mathrm{n}}| = \frac{\left((\mathbf{p}_{\mathrm{e}} - \tilde{\mathbf{p}}_{\mathrm{e}}) + \mathbf{p}_{\mathrm{n}}\right)^2}{2M} = \frac{\left(\mathbf{p}_{\mathrm{e}} - \tilde{\mathbf{p}}_{\mathrm{e}}\right)^2 + 2\left(\mathbf{p}_{\mathrm{e}} - \tilde{\mathbf{p}}_{\mathrm{e}}\right)\mathbf{p}_{\mathrm{n}} + \mathbf{p}_{\mathrm{n}}^2}{2M}. \quad (3.17)$$

Static approximation Eq. 3.17 is the general representation of the elastic scattering of an electron from a moving target atom for arbitrary directions. We can recover the static limit [21] as used in Eq. 2.4, where the atom is considered to be at rest at the moment of impact, by setting

$p_\mathrm{n} = 0$, and $\mathbf{p}_\mathrm{e} = p_\mathrm{e}\,(0,0,1)$ (assuming the electrons impinge perpendicular to a sample surface in the x-y plane) in equation 3.17:

$$\tilde{E}_\mathrm{n} = \frac{p_\mathrm{e}^2\left(\hat{\mathbf{p}}_\mathrm{e}^2 + \hat{\tilde{\mathbf{p}}}_\mathrm{e}^2 - 2\hat{\mathbf{p}}_\mathrm{e}\cdot\hat{\tilde{\mathbf{p}}}_\mathrm{e}\right)}{2M} = \frac{p_\mathrm{e}^2\,(2-2\cos\theta)}{2M} \overset{\theta=\pi}{=} \frac{2E_\mathrm{e}\,(E_\mathrm{e}+2mc^2)}{Mc^2}, \tag{3.18}$$

where the angle θ arising from the product between the initial and final electron momenta coincides with the spherical coordinate polar angle, and the last substitution yields the maximum energy transfer for electron backscattering ($\theta = \pi$).

Out-of-plane vibration-assisted energy transfer If the atom is vibrating only in the out-of-plane z direction at the moment of impact, we may instead set $\mathbf{p}_\mathrm{n} = p_\mathrm{n}\,(0,0,1)$ for the nucleus (as the momentum transfer will be increased only if the nucleus is moving in the same direction as the electron, although the other direction may also contribute to a finite cross section if the incoming electron energy is well above the threshold). The product $\hat{\mathbf{p}}_\mathrm{n}\cdot\hat{\mathbf{p}}_\mathrm{e}$ yields unity since $\hat{\mathbf{p}}_\mathrm{n} = \hat{\mathbf{p}}_\mathrm{e} = (0,0,1)$, leading to $\hat{\tilde{\mathbf{p}}}_\mathrm{e}\cdot\hat{\mathbf{p}}_\mathrm{n} = \hat{\tilde{\mathbf{p}}}_\mathrm{e}\cdot\hat{\mathbf{p}}_\mathrm{e} = \cos\theta$. Substituting these terms in equation 3.17 results in the v_z-dependent energy transfer that was previously discussed in Refs. [25, 73]

$$\begin{aligned}
\tilde{E}_\mathrm{n}\,(E_\mathrm{e}, v_\mathrm{z}, \theta) &= \frac{p_\mathrm{e}^2\,(2-2\cos\theta) + 2p_\mathrm{e}p_\mathrm{n}\,(1-\cos\theta) + p_\mathrm{n}^2}{2M} \\
&= \frac{2\,(1-\cos\theta)\left(E_\mathrm{e}\,(E_\mathrm{e}+2mc^2) + Mv_\mathrm{z}c\sqrt{E_\mathrm{e}\,(E_\mathrm{e}+2mc^2)}\right) + (Mv_\mathrm{z}c)^2}{2Mc^2} \\
&\overset{\theta=\pi}{=} \frac{\left(2\sqrt{E_\mathrm{e}\,(E_\mathrm{e}+2mc^2)} + Mv_\mathrm{z}c\right)^2}{2Mc^2}.
\end{aligned} \tag{3.19}$$

Maximum energy transfer is again obtained for electron backscattering, where the initial nuclear momentum is antiparallel to the final electron momentum.

3D-vibration assisted energy transfer To derive the full 3D description of the energy transfer we use a spherical coordinate system (see Fig. 3.1 for a graphical representation). Assuming that the incoming electron has an initial momentum along the z-axis, its direction vector is $\mathbf{p}_\mathrm{e} =$

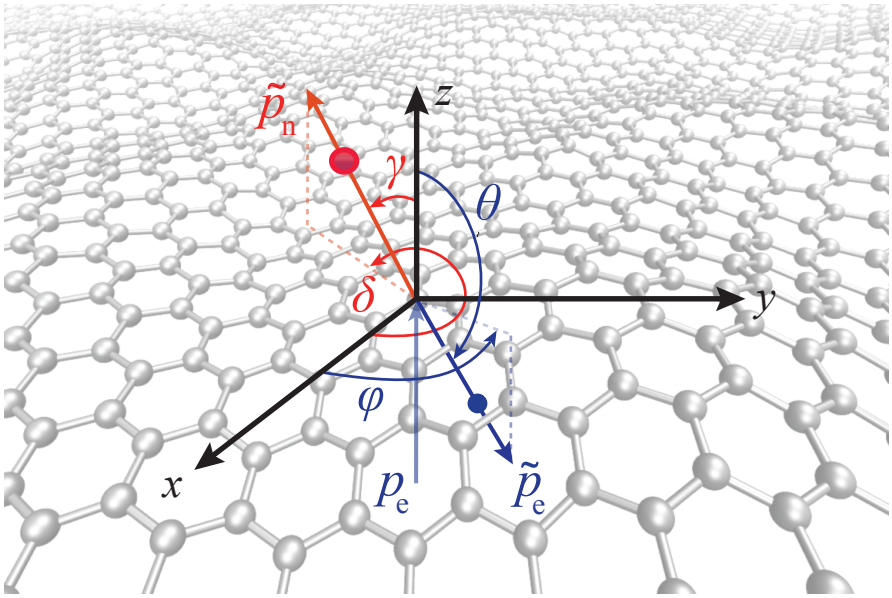

Figure 3.1: The three-dimensional electron-atom scattering geometry adapted for pristine graphene. φ and θ are the azimuthal and polar electron scattering angles after the collision (blue), whereas δ and γ are the azimuthal and polar emission angles of the atom (red).

$p_e\,(0,0,1)$. Since we know the initial momenta of the nucleus when the scattering occurs, which are later treated statistically, we denote $\mathbf{p}_n = M\,(v_x, v_y, v_z)$. The electron can scatter into any angle after the collision, $\tilde{\mathbf{p}}_e = |\mathbf{p}_e|\,(\sin\theta\cos\varphi, \sin\theta\sin\varphi, \cos\theta)$ and so can the atom, $\tilde{\mathbf{p}}_n = |\tilde{\mathbf{p}}_n|\,(\sin\gamma\cos\delta, \sin\gamma\sin\delta, \cos\gamma)$, where θ and φ are the polar and azimuthal electron scattering angles, and γ and δ the polar and azimuthal atom emission angles. Substituting these terms in Eq. 3.17 and using the trigonometric identity $\sin^2 + \cos^2 = 1$ results in the 3D energy transfer:

$$
\begin{aligned}
&\tilde{E}_n\,(E_e, v_{x,y,z}, \theta, \varphi) \\
&= \frac{p_e^2\,(2-2\cos\theta) + 2p_e M\,(v_z - v_x\sin\theta\cos\varphi - v_y\sin\theta\sin\varphi - v_z\cos\theta)}{2M} + \frac{M^2\left(v_x^2+v_y^2+v_z^2\right)}{2M} \\
&= \frac{M\left(v_x^2+v_y^2+v_z^2\right)}{2} + (1-\cos\theta)\,\frac{E_e\,(E_e+2mc^2) + Mcv_z\sqrt{E_e\,(E_e+2mc^2)}}{Mc^2} - \\
&\quad \frac{\sin\theta}{c}\,(v_x\cos\varphi + v_y\sin\varphi)\,\sqrt{E_e\,(E_e+2mc^2)}.
\end{aligned}
\tag{3.20}
$$

Setting $\theta = \pi$ and the in-plane components $v_{x,y} = 0$ will recover the out-of-plane vibration-assisted

energy transfer Eq. 3.19.

Although the scattering problem is naturally expressed in terms of the electron scattering angles θ and φ and Eq. 3.20 provides that information, the emission of the atom is often of greater interest as it is something that can be simulated. We thus need to derive a connection with the atom emission angles γ and δ to describe the emission of the atom after the collision. We decompose the momentum conservation condition Eq. 3.14 to its Cartesian components as

$$p_{\mathrm{n}}^{x} = p_{\mathrm{e}} \sin\theta \cos\varphi + \tilde{p}_{\mathrm{n}} \sin\gamma \cos\delta, \tag{3.21}$$

$$p_{\mathrm{n}}^{y} = p_{\mathrm{e}} \sin\theta \sin\varphi + \tilde{p}_{\mathrm{n}} \sin\gamma \sin\delta, \tag{3.22}$$

$$p_{\mathrm{n}}^{z} + p_{\mathrm{e}} = p_{\mathrm{e}} \cos\theta + \tilde{p}_{\mathrm{n}} \cos\gamma. \tag{3.23}$$

We can use Eqs. 3.21-3.23 to derive expressions for the atom emission angles. To express the angle δ, we solve equation 3.22 for $\tilde{p}_{\mathrm{n}}$ as

$$\tilde{p}_{\mathrm{n}} = \frac{p_{\mathrm{n}}^{y} - p_{\mathrm{e}} \sin\theta \sin\varphi}{\sin\gamma \sin\delta}, \tag{3.24}$$

substitute this in equation 3.21

$$p_{\mathrm{n}}^{x} - p_{\mathrm{e}} \sin\theta \cos\varphi = \frac{(p_{\mathrm{n}}^{y} - p_{\mathrm{e}} \sin\theta \sin\varphi) \cancel{\sin\gamma} \cos\delta}{\cancel{\sin\gamma} \sin\delta}, \tag{3.25}$$

and then solve for δ:

$$\begin{aligned} \delta\left(E_{\mathrm{e}}, v_{\mathrm{x}}, v_{\mathrm{y}}, v_{\mathrm{z}}, \varphi, \theta\right) &= \arctan\left(\frac{p_{\mathrm{n}}^{y} - p_{\mathrm{e}} \sin\theta \sin\varphi}{p_{\mathrm{n}}^{x} - p_{\mathrm{e}} \sin\theta \cos\varphi}\right) \\ &= \arctan\left(\frac{M v_{\mathrm{y}} - \sqrt{E_{\mathrm{e}}\left(E_{\mathrm{e}} + 2mc^2\right)/c^2}\, \sin\theta \sin\varphi}{M v_{\mathrm{x}} - \sqrt{E_{\mathrm{e}}\left(E_{\mathrm{e}} + 2mc^2\right)/c^2}\, \sin\theta \cos\varphi}\right). \end{aligned} \tag{3.26}$$

To obtain the atom emission angle γ, we solve equation 3.21 for $\cos\delta$:

$$\cos\delta = \frac{p_{\mathrm{n}}^{x} - p_{\mathrm{e}}\sin\theta\cos\varphi}{\tilde{p}_{\mathrm{n}}\sin\gamma}. \tag{3.27}$$

Using the trigonometric identity $\sin\delta^2 + \cos\delta^2 = 1$ we can rewrite Eq. 3.27 as

$$\sin\delta = \sqrt{1 - \frac{\left(p_{\mathrm{n}}^{x} - p_{\mathrm{e}}\sin\theta\cos\varphi\right)^2}{\tilde{p}_{\mathrm{n}}^2\sin\gamma^2}}, \tag{3.28}$$

and substitute the $\sin\delta$ term in equation 3.22 to obtain

$$p_{\mathrm{n}}^{y} - p_{\mathrm{e}}\sin\theta\sin\varphi = \sqrt{\tilde{p}_{\mathrm{n}}^2\sin\gamma^2 - \left(p_{\mathrm{n}}^{x} - p_{\mathrm{e}}\sin\theta\cos\varphi\right)^2}. \tag{3.29}$$

Next, we square both sides,

$$\tilde{p}_{\mathrm{n}}^2\sin\gamma^2 = \left(p_{\mathrm{n}}^{x} - p_{\mathrm{e}}\sin\theta\cos\varphi\right)^2 + \left(p_{\mathrm{n}}^{y} - p_{\mathrm{e}}\sin\theta\sin\varphi\right)^2, \tag{3.30}$$

solve equation 3.23 for $\tilde{p}_{\mathrm{n}}$,

$$\tilde{p}_{\mathrm{n}} = \frac{p_{\mathrm{n}}^{z} + p_{\mathrm{e}}\left(1 - \cos\theta\right)}{\cos\gamma}, \tag{3.31}$$

and substitute it in Eq. 3.30 to solve for γ:

$$\begin{aligned}
\gamma\left(E_{\mathrm{e}}, v_{\mathrm{x}}, v_{\mathrm{y}}, v_{\mathrm{z}}, \varphi, \theta\right) &= \arctan\left(\frac{\sqrt{\left(p_{\mathrm{n}}^{x} - p_{\mathrm{e}}\sin\theta\cos\varphi\right)^2 + \left(p_{\mathrm{n}}^{y} - p_{\mathrm{e}}\sin\theta\sin\varphi\right)^2}}{p_{\mathrm{n}}^{z} + p_{\mathrm{e}}\left(1 - \cos\theta\right)}\right) \\
&= \arctan\Bigg(\Bigg[\left(Mv_{\mathrm{x}} - \sqrt{E_{\mathrm{e}}\left(E_{\mathrm{e}} + 2mc^2\right)/c^2}\,\sin\theta\cos\varphi\right)^2 + \\
&\quad \left(Mv_{\mathrm{y}} - \sqrt{E_{\mathrm{e}}\left(E_{\mathrm{e}} + 2mc^2\right)/c^2}\,\sin\theta\sin\varphi\right)^2\Bigg]^{1/2} / \\
&\quad \left(Mv_{\mathrm{z}} + \sqrt{E_{\mathrm{e}}\left(E_{\mathrm{e}} + 2mc^2\right)/c^2}\,\left(1 - \cos\theta\right)\right)\Bigg).
\end{aligned} \tag{3.32}$$

We can also use momentum and energy conservation equations to calculate the transferred energy $\tilde{E}_{\mathrm{n}}\left(E_{\mathrm{e}}, v_{\mathrm{x}}, v_{\mathrm{y}}, v_{\mathrm{z}}, \gamma, \delta\right)$ in terms of the atom emission angles γ and δ (see Fig. 3.3 for its behaviour against γ in pristine graphene). However, the solution to this equation is quite complicated and was only solved in Mathematica. The solutions are listed in Appendix A.4 and in our supplementary Mathematica notebook to Ref. [57] as functions named *Tmaxcase11* and *Tmaxcase12*. Now, not only can we predict the amount of energy transferred to an arbitrarily moving atom, but can also predict its emission in any arbitrary direction as a result of the elastic scattering with an electron.

3.2 Cross section for displacements in 3D

Here, we further introduce a three-dimensional theoretical approach to describing the displacement cross section for arbitrarily moving atoms emitted in arbitrary directions. This takes into consideration the atom velocities at the moment of impact as described by Eq. 3.20, but also accounts for changes in the displacement threshold energy of the atom, either due to variaton with respect to the atom emission angles or thermal perturbations [25]. Both are effects that can be quantified employing molecular dynamics as we will see in the next sections. Taking into account the anisotropy of the displacement threshold energy and the atomic vibrations in 3D, we integrate Eq. 2.1 as follows:

$$\sigma_{\mathrm{3D}}^{T}=\int\int\prod_{i=\{x,y,z\}}\int_{-v_i^{\max}}^{v_i^{\max}}P(v_i,\overline{v_i^2})\,P(E_{\mathrm{d}},w(T))\,\mathcal{H}(\tilde{E}_{\mathrm{n}}-\xi E_{\mathrm{d}}\left(\gamma,\delta\right))\,\sigma(E_{\mathrm{e}},\theta)\,\mathrm{d}v_i\,\sin\theta\,\mathrm{d}\theta\,\mathrm{d}\varphi, \tag{3.33}$$

where $P(v_i,\overline{v_i^2})$ with $i=x,y,z$ are the normal distributions of velocities of the target atom with mean-square velocities (variances) $\overline{v_i^2}$ derived from the phonon density of states [24] and integrated over e.g. $\pm 3v_i^{max}$ covering the variation of velocities, $P(E_{\mathrm{d}},w(T))$ is a normal distribution accounting for the thermal variation of E_{d} at temperature T [25], where $w(T)$ is the standard deviation, $\mathcal{H}$ is the Heaviside step function ensuring the transferred energy $\tilde{E}_{\mathrm{n}}$ exceeds $E_{\mathrm{d}}\left(\gamma,\delta\right)$ and ξ is a fitting factor multiplying the simulated $E_{\mathrm{d}}\left(\gamma,\delta\right)$ to help match the experimentally

observed displacement cross-sections. Introducing the factor ξ is a necessity since the simulated displacement threshold energies do not always match with the ones resulting from experimental data. As a measure of goodness of the fit and for finding ξ, we calculate a weighted mean-square error (WMSE) as

$$\mathrm{WMSE}\left(\xi\right) = \frac{\left[\sigma_{\mathrm{theory}}\left(\xi E_{\mathrm{d}}\left(\gamma,\delta\right)\right) - \sigma_{\mathrm{exp}}\right]^2}{\epsilon_{\mathrm{exp}}}, \tag{3.34}$$

where σ_{theory} can be any theoretical model used to describe the cross-section (e.g. σ_{3D}), σ_{exp} is the experimentally observed displacement cross section and ϵ_{exp} its corresponding measurement uncertainty (typically standard error of the mean). The closer ξ is to unity, the better the simulated $E_{\mathrm{d}}\left(\gamma,\delta\right)$ matches experimental data.

To describe the dependence of E_d on the atom emission angles and to exclude the angles that do not contribute to the cross section, we use an interpolation function defined piece-wise as follows:

$$E_{\mathrm{d}}\left(\gamma,\delta\right) = \begin{cases} E_{\mathrm{d}}\left(\gamma,\delta\right) & \gamma_1 \leq \gamma \leq \gamma_2 \text{ and } \delta_1 \leq \delta \leq \delta_2 \\ 50 \text{ eV} & \end{cases}, \tag{3.35}$$

where the polar atom emission angles γ_1, γ_2 and the azimuthal atom emission angles δ_1, δ_2 represent the lower and upper ranges of the angular sector of the simulated displacement threshold energies. The value of 50 eV is chosen large enough for our range of primary beam energies to avoid any incorrect extrapolation. Using an interpolation function allowed us to sample displacement threshold energies within a specific range and perform accurate numerical integrations.

3.2.1 Numerical integration of the displacement cross section

To estimate the total displacement cross section we have to integrate Eq. 3.33, which depending whether we take temperature variation of E_{d} into account or not, will have 5 or 6 dimensions. This demanding multi-dimensional integral had to be integrated with numerical methods. We tried several methods using Python's scipy [109] library as well as "brute-force" approaches, which did not yield a converged result in any reasonable amount of time; scipy's `quad` function never yielded

any result, even after letting it run for several days. Mathematica features a large number of advanced integration methods and we have trialed most of them. Adaptive algorithms and Monte Carlo methods, such as the `AdaptiveMonteCarlo` delivered inconsistent results, while some others would take unreasonable amounts of time to compute and still be inconsistent. However, the `GlobalAdaptive` algorithm [110] as implemented in Mathematica proved to be the only method to deliver consistent results. To ensure the numerical precision of the integrals to two decimal places we used the option `PrecisionGoal=2`, and for a finer subdivision of the integration region, especially in areas where the cross section is small, we opted for `MinRecursion=4`. To calculate a cross section for a single acceleration voltage point to this degree of accuracy usually takes one minute on a modern CPU, and one can parallelize the computation over available cores using `ParallelTable`.

3.3 Pristine graphene

To evaluate our 3D theory, we first turned to the best-characterized system, namely knock-on damage of pristine graphene. We performed displacement simulations for a C atom in pristine graphene covering the polar atom emission angle $0° \leq \gamma \leq 30°$ in $5°$ steps, and azimuthal angle $0° \leq \delta \leq 60°$ in $10°$ steps, which by symmetry allows us to predict $E_\mathrm{d}(\gamma, \delta)$ for all azimuthal angles δ as pictured in Fig. 3.2. We found that the displacement threshold energy E_d lies within the range $[22.55, 23.25]$ eV (tested in steps of 0.05 eV) and can see that $E_\mathrm{d}(\gamma, \delta)$ increases for $\gamma > 0°$ (as also noted earlier in [72]). With increasing angle γ, also the energy transfer becomes smaller because the electron scattering angle θ is also smaller than π (backscattering) and with it the amount of energy transferred is reduced from the maximum. This is the reason why we only simulated emissions up to $\gamma = 30°$, since the reduced energy transfer cannot overcome the increasing displacement threshold energy. To confirm this, we plotted (Fig. 3.3) the transferred energy $\tilde{E}_\mathrm{n}(E_\mathrm{e}, v_\mathrm{x}, v_\mathrm{y}, v_\mathrm{z}, \gamma, \delta)$ (see Appendix A.4 for the complete formula) with respect to the atom emission angle γ at an acceleration voltage $E_\mathrm{e} = 100$ keV for different velocities and azimuthal angles δ and compared it to the displacement threshold energies $E_\mathrm{d}(\gamma, \delta)$. While certain energy transfers for $\gamma > 30°$ can be significant (Fig. 3.3), they will not contribute to the total cross section since the probability of the required large velocities is very low (due to multiplication with the velocity normal distributions in Eq. 3.33).

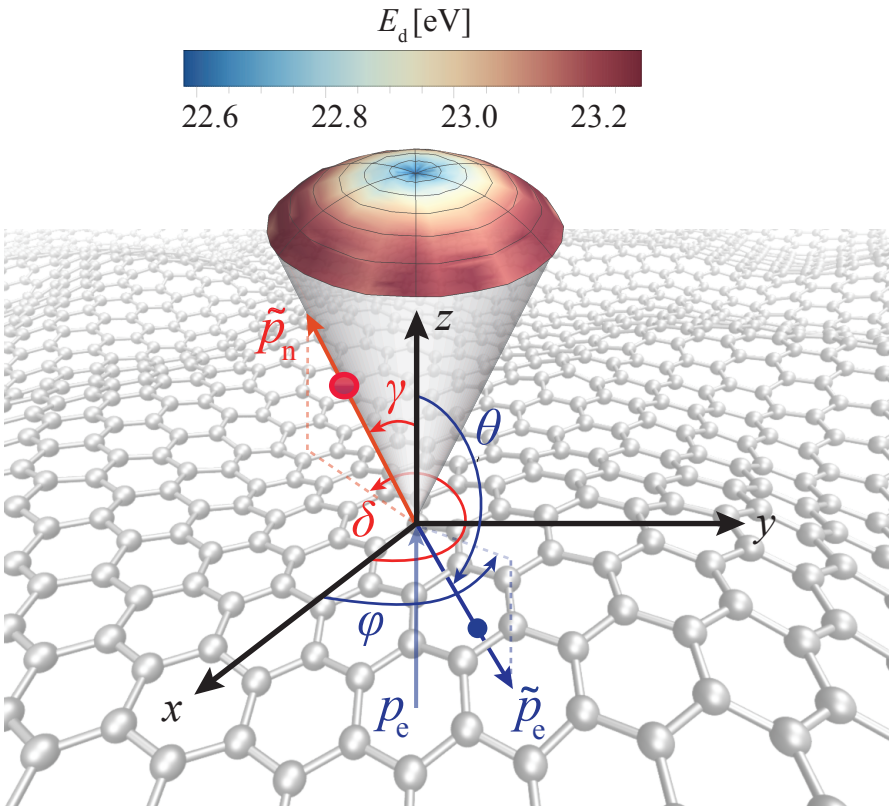

Figure 3.2: The three-dimensional electron-atom scattering geometry adapted for pristine graphene. φ and θ are the azimuthal and polar electron scattering angles after the collision (blue), whereas δ and γ are the azimuthal and polar emission angles of the atom (red). The colored dome indicates the calculated and interpolated angular variation of the displacement threshold energy E_d for pristine graphene calculated with DFT/MD. Figure reproduced from ref. [57] (CC-BY 4.0).

To test our theory, we compared it to the experimental cross-section data for knock-on acquired by colleagues [24]. In Table 3.1 we present the data points at acceleration voltages $E_e = 85$, 90, 95 and 100 keV and also their corresponding fits using the theoretical models for the out-of-plane velocity cross section σ_{v_z} (see Eq. 2.6) and the full 3D cross section σ_{3D} (see Eq. 3.33 without the temperature component), and plot the two models and the experimental data in Fig. 3.4. There is no significant difference between the two theoretical models, as they both fit the experimental data to the same extent. The fitting was done using Eq. 3.34, and the scaling factor ξ required to multiply the simulated displacement thresholds yielded values of $\xi_{v_z} = 0.938$ and $\xi_{3D} = 0.932$ for the σ_{v_z} and σ_{3D} cross-section models, respectively. Also, in terms of error, these two models were very similar with WSME values (Eq. 3.34) yielding 0.005 and 0.004 for the σ_{v_z} and σ_{3D} models, respectively. Thus, this not only shows that the vz-only model is sufficient to describe knock-on damage of pristine graphene, but also provides the first test of the validity of our 3D model.

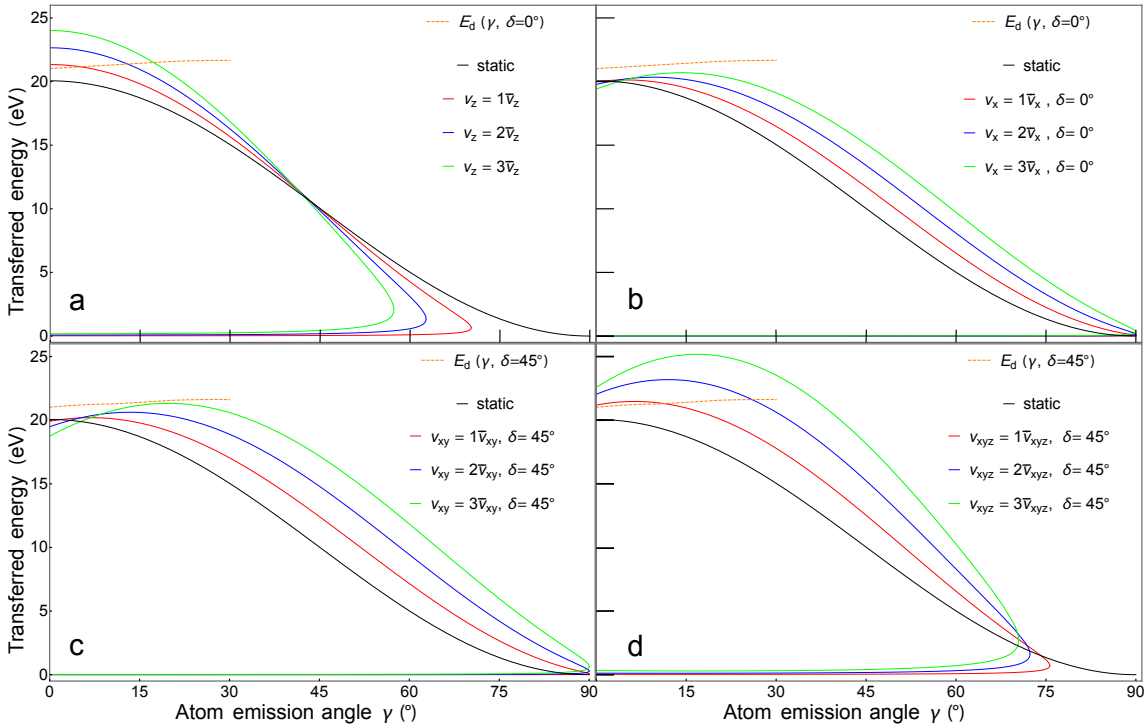

Figure 3.3: Transferred energy $\tilde{E}_{\mathrm{n}}$ as a function of atom polar emission angle γ for graphene for different initial velocities and azimuthal emission angles δ for an acceleration voltage of $E_{\mathrm{e}} = 100$ keV. The static approximation of the transferred energy (Eq. 3.18), where no initial velocity of the atom is taken into consideration, and the 3D model are compared to the DFT/MD displacement threshold energy $E_{\mathrm{d}}(\gamma, \delta)$, which is plotted as an orange dashed line. For the non-static cases, the energy curves are plotted for 1–3 standard deviations from the velocity mean for different combinations of initial velocities (a) z ($\overline{v}_z$); note that scattering in this case is isotropic as a function of the azimuthal atom scattering angle δ, (b) x ($\overline{v}_x$), (c) xy ($\overline{v}_x$ and $\overline{v}_y$), and (d) xyz ($\overline{v}_x$, $\overline{v}_y$, $\overline{v}_z$) directions, plotted for (b) $\delta = 0°$ or (c,d) $\delta = 45°$.

Table 3.1: Experimental cross sections for pristine graphene compared to the theoretical models $\sigma_{\mathrm{v_z}}$ and σ_{3D}. The experimental data is from Ref. [24].

E_{e} [keV]	Exp. cross section [barn]	$\sigma_{\mathrm{v_z}}$ [barn]	σ_{3D} [barn]
85	12.0×10^{-4}	2.0×10^{-4}	2.5×10^{-4}
90	10.9×10^{-3}	4.9×10^{-3}	5.7×10^{-3}
95	0.056	0.056	0.059
100	0.328	0.328	0.325

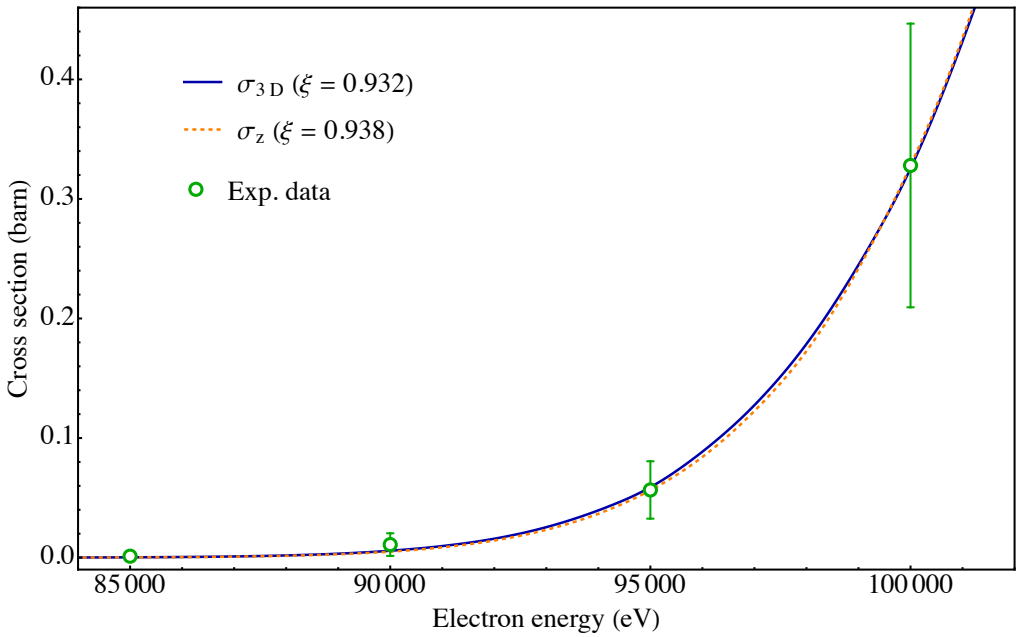

Figure 3.4: Comparison of experimental knock-on cross section for pristine graphene (green open circles) with the calculated ones for the full 3D (solid blue line) and the v_z-only (dashed orange line) velocity models. The experimental data points are from Ref. [24].

3.4 Si-doped graphene

We further performed displacement simulations for another experimentally quantified graphene system: the trivalent Si–C_3 impurity [27, 51, 64], where the impacted C atom exchanges places with the Si atom (yellow sphere in Fig. 3.5). We explored multiple pathways for the exchange process to happen, and calculated the displacement threshold energy $E_d(\gamma, \delta)$ that will lead to an exchange between the two atoms for $0° \leq \gamma \leq 30°$ in $5°$ steps, and $0° \leq \delta \leq 180°$ in $10°$ steps (due to symmetry only covering the half-dome shown in Fig. 3.5). The displacement energy was varied from 14 to 21 eV in steps of 0.25 eV until an exchange occured or the atom was ejected. Again we used Eq. 3.35 to create an interpolation function defined piecewise only for the ranges we simulated. The possible pathways for such a beam-driven exchange to happen are shown by the color-coded tiles of the half-dome in Fig 3.5. The uncolored tiles of the left half-dome represent angles at which no exchange between the atoms was observed. The displacement energies that lead to a silicon-carbon exchange vary from 14.25 to 20.25 eV. The lowest-energy exchange pathways lie in the direction of the Si-C bond, away from the Si atom. In this sector (blue to dark-blue in Fig. 3.5), E_d drops with increasing γ. On the other hand, if we orient the C displacement direction towards the Si atom, E_d will take higher values with increasing γ. The

reason is that the Si atom buckles out from the plane and is more likely to fall in the place of the ejecting carbon atom if it is displaced away from as opposed to towards the Si atom.

In Table 3.2 we present experimental cross-section data from Ref. [27] and yet unpublished data acquired by colleagues with the STEM at 55, 60, 65 and 70 keV, and the corresponding fits using the theoretical models σ_{v_z}, σ_{3D} and σ_{3D}^{T} (with and without the temperature variation of E_d). While the fitting using Eq. 3.34 apparently yielded scaling factors for the simulated displacement threshold energies very close to unity: $\xi_{v_z} = 0.987$, $\xi_{3D} = \xi_{3D}^{T} = 0.980$, we can tell by looking at Fig. 3.6 that all three theoretical models are a poor match to the experimental cross-section data, especially the points at 60 and 65 keV. This is also reflected in the large WSME values we get with Eq. 3.34 for all three cases: 7.85, 7.17, 6.47 for σ_{v_z}, σ_{3D}, σ_{3D}^{T}, respectively.

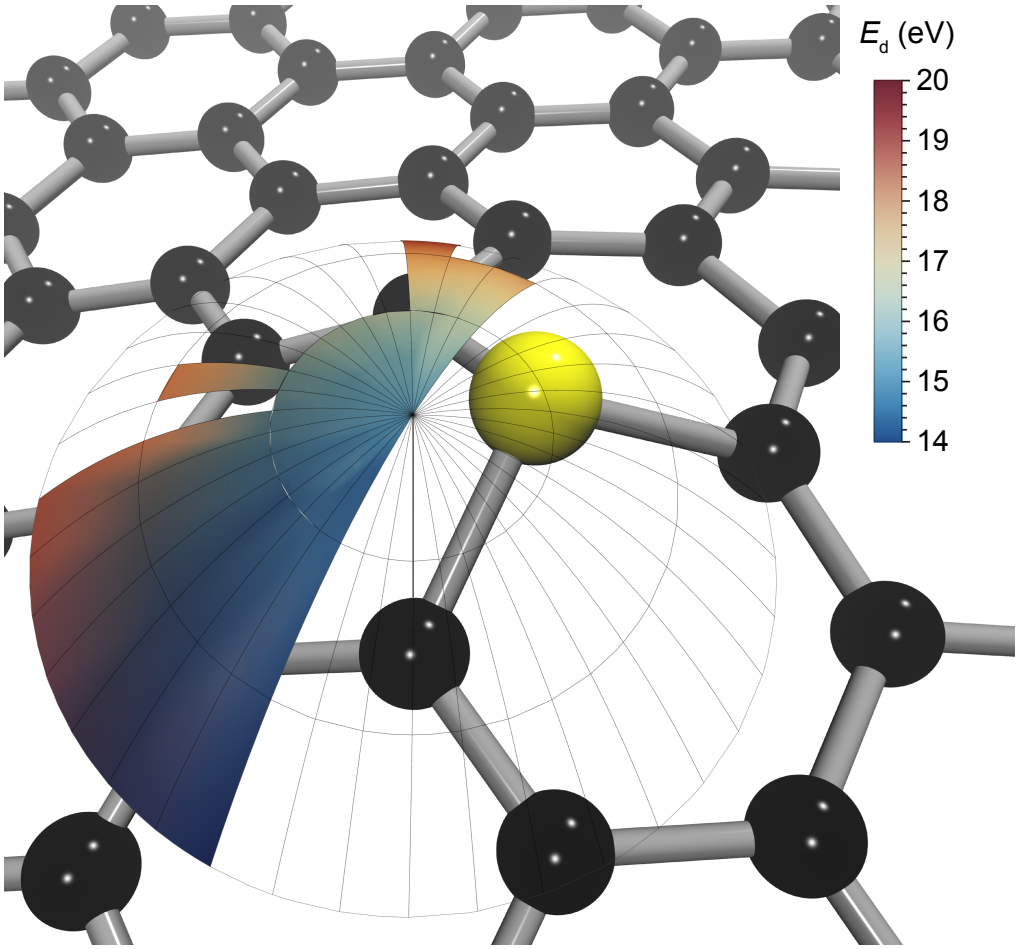

Figure 3.5: Graphene with a Si impurity (yellow sphere). The colored half-dome represents the variation of the displacement threshold energy $E_d(\gamma, \delta)$ of a carbon atom in the vicinity of the Si impurity that will lead to a Si-C inversion in graphene, estimated with DFT/MD and numerically interpolated. We left the other symmetric half-dome tiles uncolored for the clarity of the graphical representation.

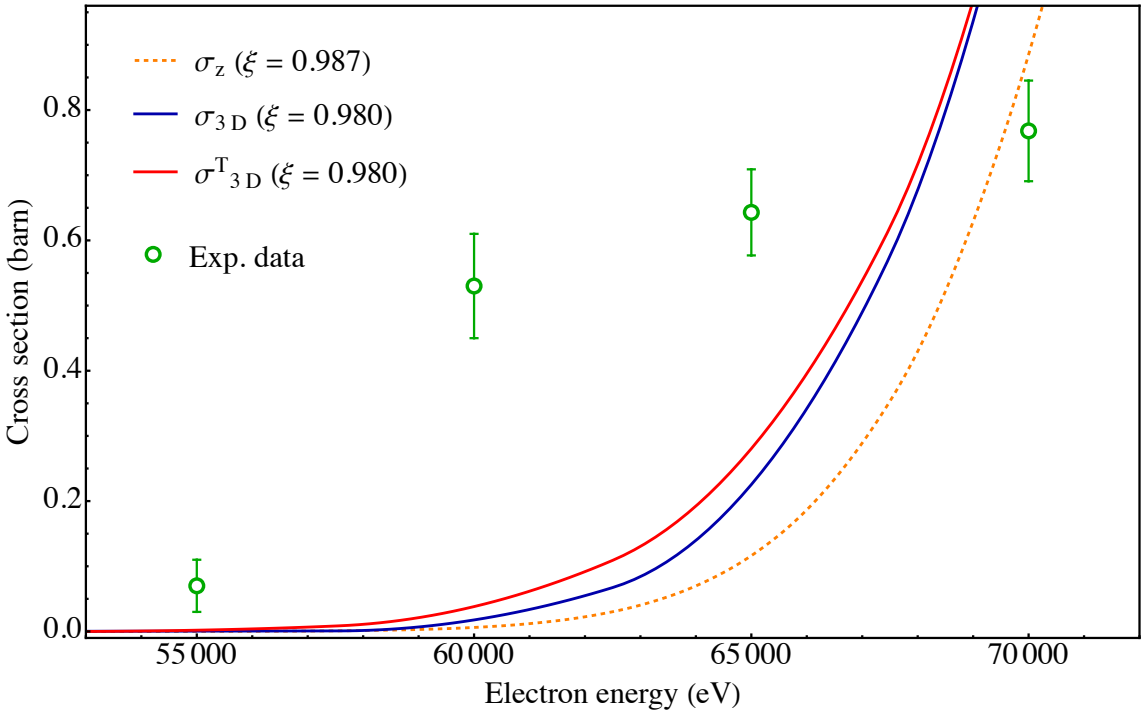

Figure 3.6: Comparison of experimental cross-section (green open circles) for the Si–C exchange events with the calculated ones for the full 3D with and without temperature effects (red and solid blue lines), the v_z-only (dashed orange line). The experimental data points are taken from Ref. [27] and yet unpublished data.

Table 3.2: Experimental cross sections for the Si–C inversion compared to the theoretical predictions calculated with the out-of-plane vibration model σ_{v_z}, the three-dimensional vibration model σ_{3D}, and the temperature-dependent three-dimensional vibration model σ^T_{3D}. The experimental data is from Ref. [27] and yet unpublished work.

E_e [keV]	Exp. cross section [barn]	σ_{v_z} [barn]	σ_{3D} [barn]	σ^T_{3D} [barn]
55	$0.07 \pm 4 \times 10^{-3}$	1×10^{-4}	4×10^{-4}	0.002
60	0.530 ± 0.08	0.006	0.017	0.038
65	0.643 ± 0.06	0.116	0.225	0.280
70	0.768 ± 0.07	0.885	1.263	1.287

3.4.1 Graphene doped with multiple Si atoms

We additionally ran another set of displacement simulations for larger cells ($7\times7\times1$) where there is more than one Si atom in the cell using the same computational methodology as for graphene with one Si impurity, however for $\gamma = 0°$ emissions only. The idea was to simulate local configurations that might come up in larger structures as shown in Fig. 3.7, and to check whether or not the exchange process will happen. Most of the displacements resulted in knocking out the C atom,

and some recombined to form pentagon or octagon-type defects. We found that the Si–C_3 will exchange only in three out of the nine configurations we trialed, namely configurations 1, 2 and 9 (see Fig. 3.8). The atoms marked with green were subject to displacement simulations (and are numbered same as in the simulation cell). Not all the marked C atoms in configurations 1,2,9 will result in an exchange with the Si atoms: only atom 62 of configuration 1 will undergo an exchange with its neighboring Si atom at $E_\mathrm{d} = 14.25$ eV, while in configuration 2, both atoms 35 and 48 will switch places with their neighboring Si atom for $E_\mathrm{d} = 15.0$ eV, as well as atom 35 of configuration 9 for $E_\mathrm{d} = 14.75$ eV. It is also worth noting that only C atoms which have a direct bond to the Si impurity can potentially lead to an exchange. The remaining of the marked C atoms have KO thresholds varying from 13.5 to 23 eV, depending on their position relative to the Si impurities. The lowest KO threshold, 13.5 eV, was found for the C atom in configuration 4, which has two Si atoms as its nearest neighbors (see Fig. 3.7), while the highest E_d (>22.0 eV)

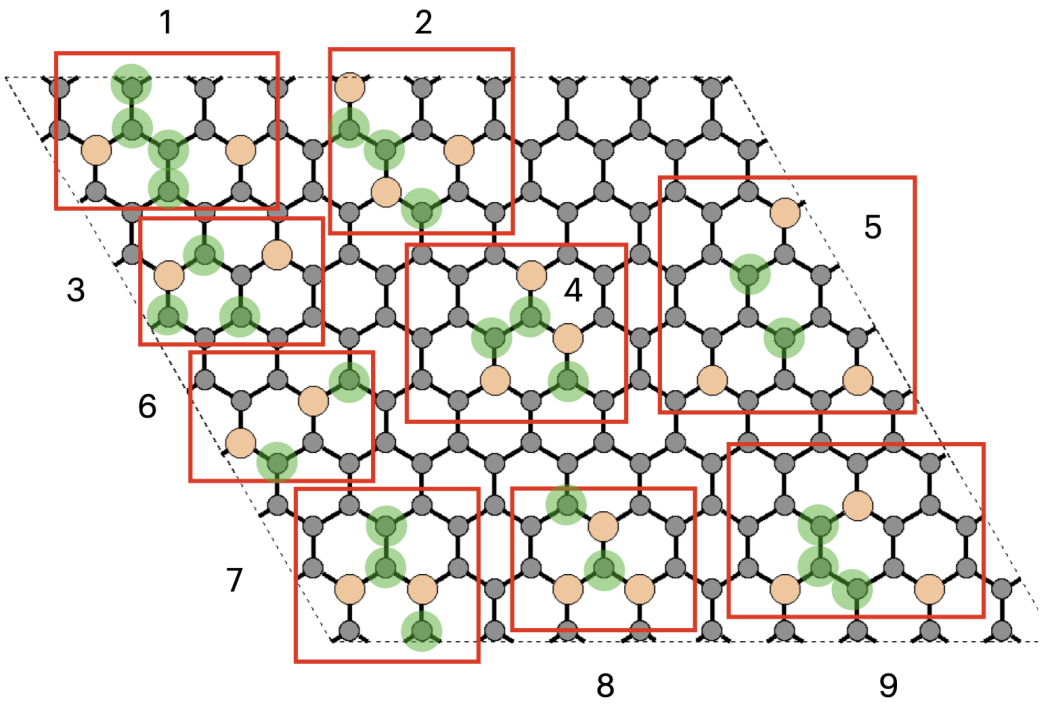

Figure 3.7: Sketch of different possible local Si–C_3 configurations that might occur in larger structures. Each red square, numbered from 1-9, represent distinct configurations that were independently simulated in separate supercells. The beige-colored atoms represent Si, and those highlighted in green are the C atoms which have been subject to displacement simulations, covering distinct local configurations by symmetry.

is found for atoms that do not have a Si atom as their neighbour.

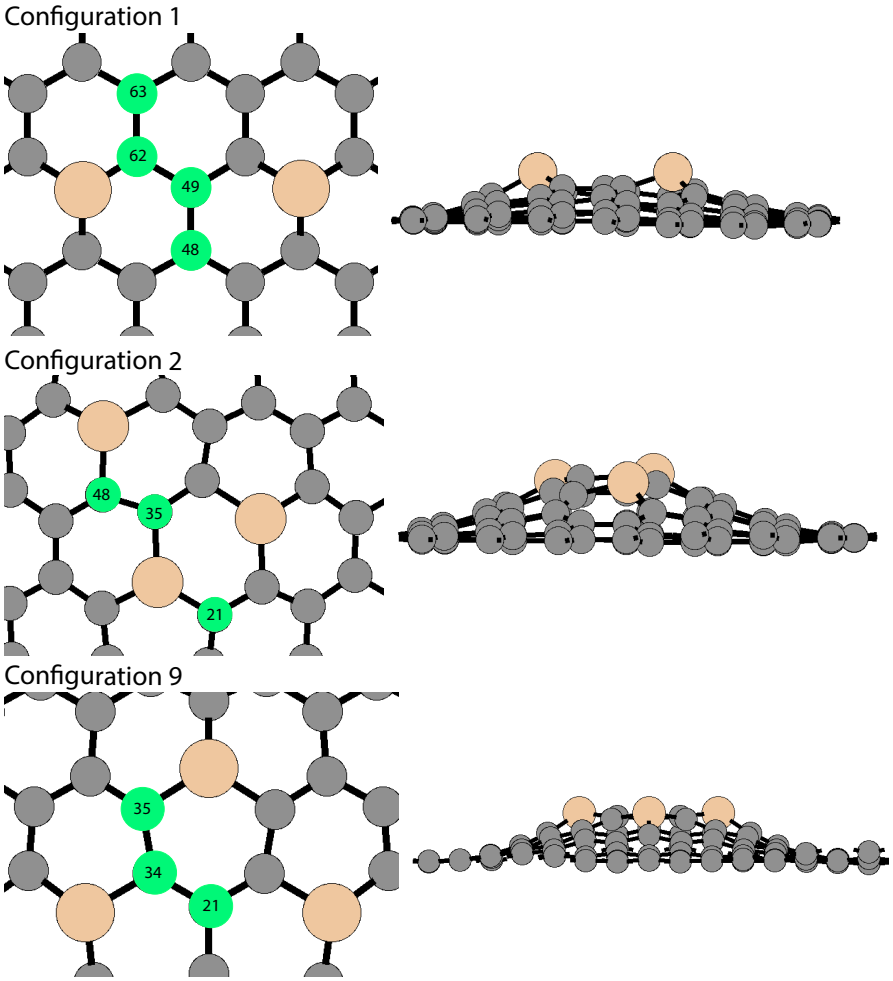

Figure 3.8: Close-up views on the configurations 1, 2 and 9, where a Si–C exchange was observed. The beige-colored atoms represent Si atoms, and the green marked ones are the C atoms which have been subject to displacement simulations (the atoms are numbered as in the structure files). Atom 62 of configuration 1 will change places with the neighboring Si atom at $E_\mathrm{d} = 14.25$ eV, atom 35 and 48 of configuration 2 will both change places with their neighboring Si atom at $E_\mathrm{d} = 15.0$ eV; and atom 35 of configuration 9 will change places with the neighboring Si atom at $E_\mathrm{d} = 14.75$ eV.

3.5 Pyridinic N

We further explored the implications of our 3D theory by running MD simulations for the reversible transformations of the pyridinic nitrogen impurity. The N can jump back and forth across the vacancy, as originally observed by Lin et. al. [28]. This configuration is similar to a single vacancy, but with the dangling-bond C atom replaced by N, bonding to two C neighbors and stabilizing the defect as presented in Fig. 3.9. We acquired statistical data for the reversible jumps at both 55 and 60 keV at room temperature (see Fig. 3.10g,h). Further, although two instances of N knock-out were also observed at 55 keV, this was not sufficient to obtain a reliable cross-section estimate and thus only the value at 60 keV based on eight observed events was estimated to be 1.54 barn.

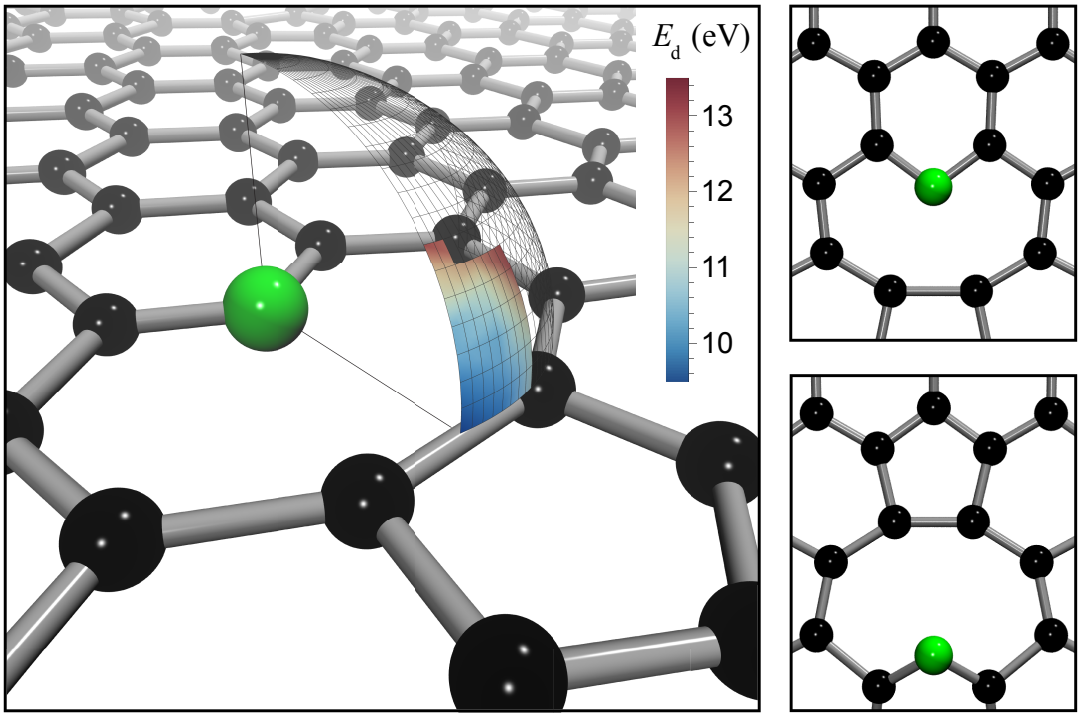

Figure 3.9: Graphene with a pyridinic N–C_2 impurity site. The color-coded quarter-dome is a representation of the possible N jump pathways with their corresponding energy thresholds E_d, estimated with DFT/MD and numerically interpolated. The uncolored tiles of the dome represent trialed ejection pathways of the N atom, which did not lead to jumping across the vacancy and bonding on the other side. For the purpose of having a clear representation of the defect site, we did not draw the other quarter-dome despite it being equivalent by symmetry.

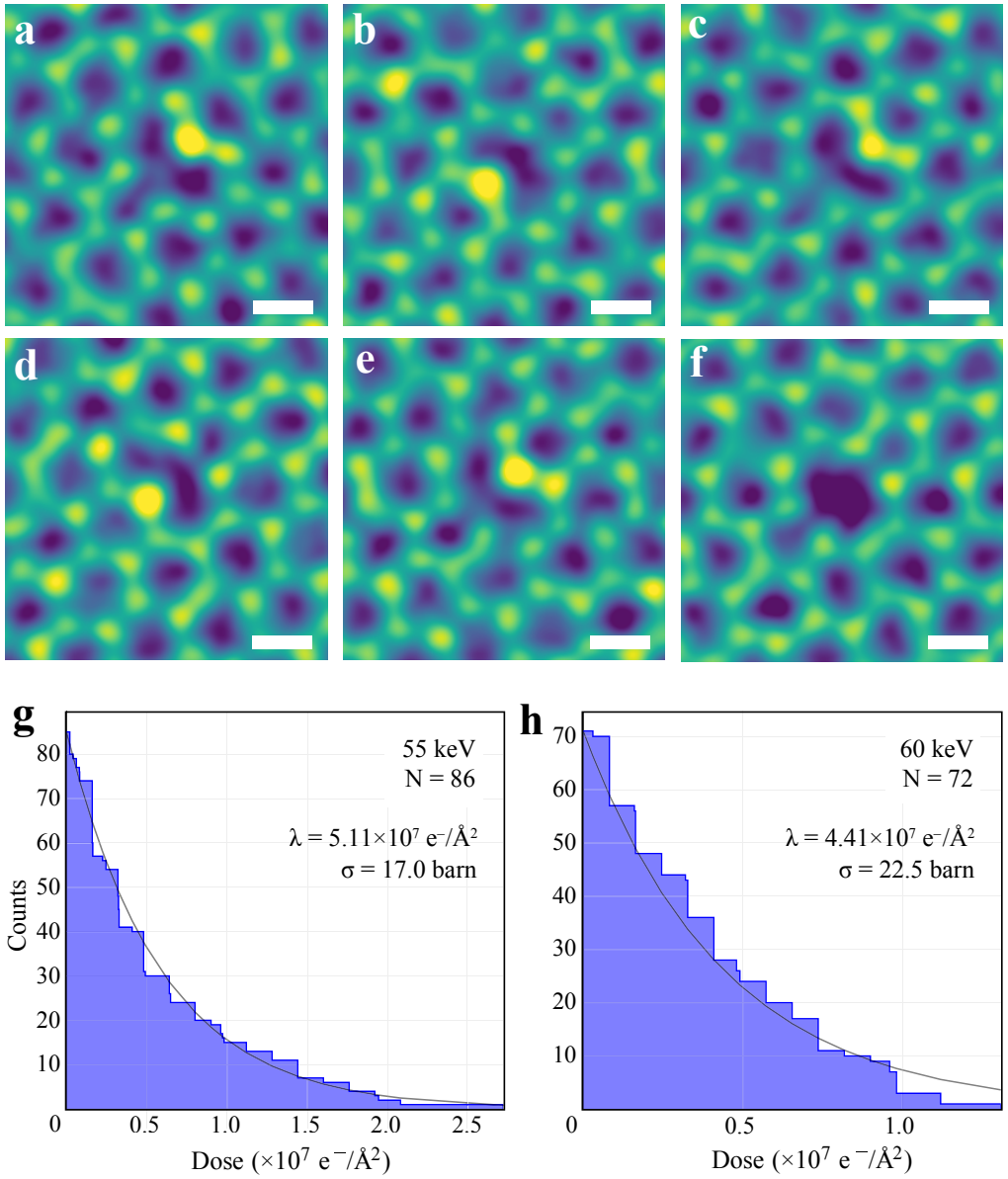

Figure 3.10: Reversible jumps of N across a vacancy in graphene. (a–f) Six selected frames from a medium-angle annular dark-field scanning transmission electron microscopy image series which contained a total of 17 jumps, recorded at 60 keV at room temperature, with the N atom finally ejected before the last frame. The scale bar is 2 Å. (g, h) Exponential distribution of jump doses (N events in total; each bin contains all the events that occurred at doses higher than the lower bin limit) fitted with the expected Poisson expectation value λ at (g) 55 keV (resulting cross section σ of 17.0 barn) and (h) 60 keV (22.5 barn).

We ran DFT/MD displacement simulations for various emission angles to determine under which conditions the N can cross the vacancy to bind with the C atoms on the other side. From the colored-coded area in Fig. 3.9, we can immediately tell that maximum energy transfers at or around $\gamma = 0°$ will not result in a jump, regardless of the angular orientation or how much initial momenta

the N atom receives. Instead, we found that effective emission directions where the N jumped and recombined across the vacancy lie in a narrow sector between $90° \leq \delta \leq 110°$ (and symmetrically towards the other side, where $\delta = 90°$ points directly across the vacancy) and at relatively large polar emission angles $55° \leq \gamma \leq 90°$, with $E_\mathrm{d}(\gamma, \delta)$ ranging from 10 to 13.5 eV (see color-coded area in Fig. 3.9; again a representation of the numerically interpolated displacement thresholds $E_\mathrm{d}(\gamma, \delta)$ taken from DFT/MD).

For other angles or energies, either no change in the site occurs due to the restoring force of the two C neighbours, or the N almost ejects from the lattice and is left as an adatom near its original position, which happens for a range of emission angles close to the surface normal at energies between 14–16 eV (Fig. 3.11). Although most such adatom configurations presumably recombine at the closest side of the defect, thus restoring the site to its original configuration, adatom migration at room temperature may allow some of them to recombine on the other side, which would be experimentally indistinguishable from a direct jump. At even higher transferred energies, which are increasingly unlikely at primary beam energies of 60 keV or below, the N can be entirely ejected from the lattice.

To explore the alternative pathway via an N adatom route (Fig. 3.11) and evaluate the probability for the adatom to recombine on either the original side of the vacancy, or the other side thus appearing as a jump, we ran Monte Carlo simulations [57] in three simulation cells: an open world, where an adatom can diffuse away from the defect, and closed periodic cells of two sizes modeling the potential energy well around the vacancy, where it always ends up recombining on either side. These constitute "best" and "worst" case estimates for the true probability with the assumption that all migration barriers are equal. Based on 10,000 simulations for each case,

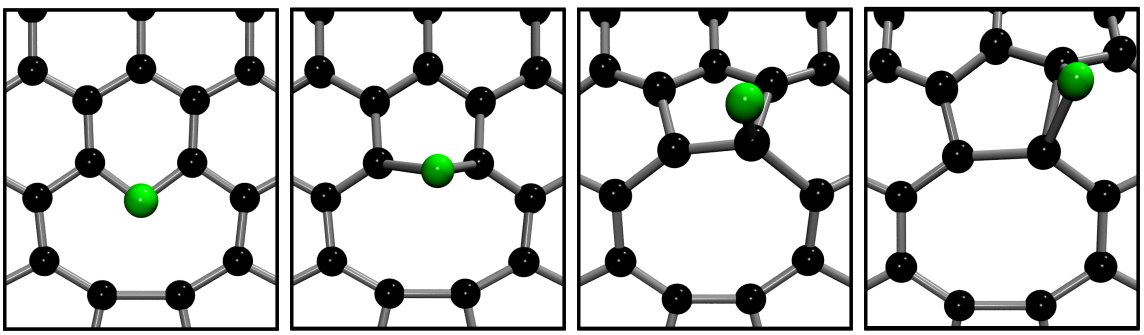

Figure 3.11: Selected top views from a DFT/MD trajectory of a higher-energy perpendicular ejection ($\gamma = 5°$, $\delta = 5°$, $\tilde{E}_\mathrm{n} = 15$ eV) resulting in an N adatom near its original location.

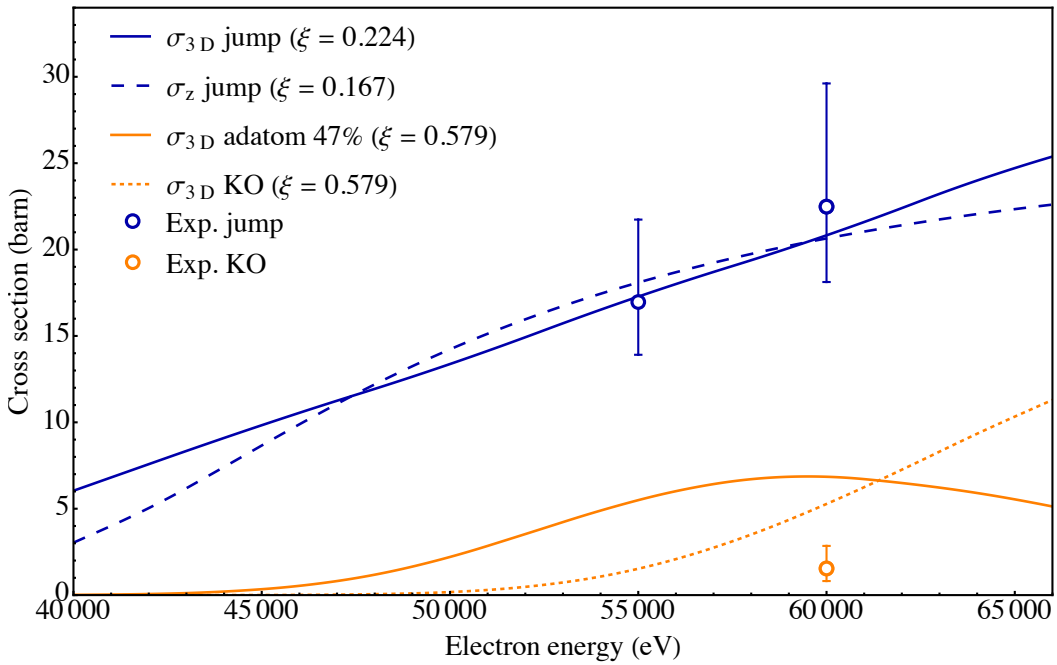

Figure 3.12: Comparison of experimental jump (blue open circles) and knock-on (KO, orange open circle) cross sections with the calculated ones for the full 3D (solid blue line) and z-only (dashed blue line) models for the direct jump pathway (Fig. 3.9), as well as the 3D model for displacement to an adatom (Fig. 3.11) followed by recombination on the other side at 47% probability (orange solid line), and direct knock-out corresponding to the same scaling factor ξ (orange dashed line). The error bars correspond to 2-sigma confidence intervals. The cross section values are presented also in Table 3.3

probabilities for the N adatoms to recombine on the other side range from 32% (open world, only considering those atoms that do not escape) to 47% (periodic 3×3×1 cell) [57]. The latter value is used in Fig. 3.12 to plot the limiting case for the apparent jump cross sections via an adatom-mediated route. To estimate this cross section, we multiply $\sigma_{3\mathrm{D}}$ by 0.47 when doing the fitting with Eq. 3.34. Both theoretical cross-section models σ_{v_z} and $\sigma_{3\mathrm{D}}$ can be fitted to match the experimental jump cross sections closely (see Fig. 3.12) with WMSE values of 1.18 and 0.55 barn, respectively. However, the scaling factors $\xi_{v_z} = 0.167$ and $\xi_{3\mathrm{D}} = 0.224$ are far below unity, and represent a 83.3% and 77.6% decrease, respectively, from the original DFT/MD threshold energy values E_{d}. In Fig. 3.13 we have plotted the amount of energy that can be transferred to a N atom in the static approximation and in the full 3D model for various initial velocity combinations of the atom with respect to the atom emission angle γ. We compared the energy transfers to the scaled $\xi E_{\mathrm{d}}(\gamma, \delta)$ (orange dots) for $\xi = 0.224$. Despite drastically scaling down $E_{\mathrm{d}}(\gamma, \delta)$ so that the N could receive sufficient energy to reach the other side of the vacancy against the restoring force of

its original two C neighbors, the static model would miss any possible jump above $\gamma \approx 60°$. Even though the jump trajectory is close to in-plane, the 3D model does not fare much better than the out-of-plane model (0.167 vs. 0.224 scaling factor ξ), and thus fails to describe the remarkably high experimentally observed jump rates. Without the scaling factor, the predicted jump cross-sections would be negligible for both elastic models. Finally, theoretical adatom and KO curves were simultaneously fit to match the jump and knock-out cross sections, and they deliver the best fit for $\xi = 0.579$. The σ_{3D} adatom curve is still far from matching the experimental data as can be seen in Fig. 3.12. By further lowering the scaling fator ξ, one would be able to match the jump cross section, but it would result in a too high probability to knock out the N atom, contradicting the experimental observations.

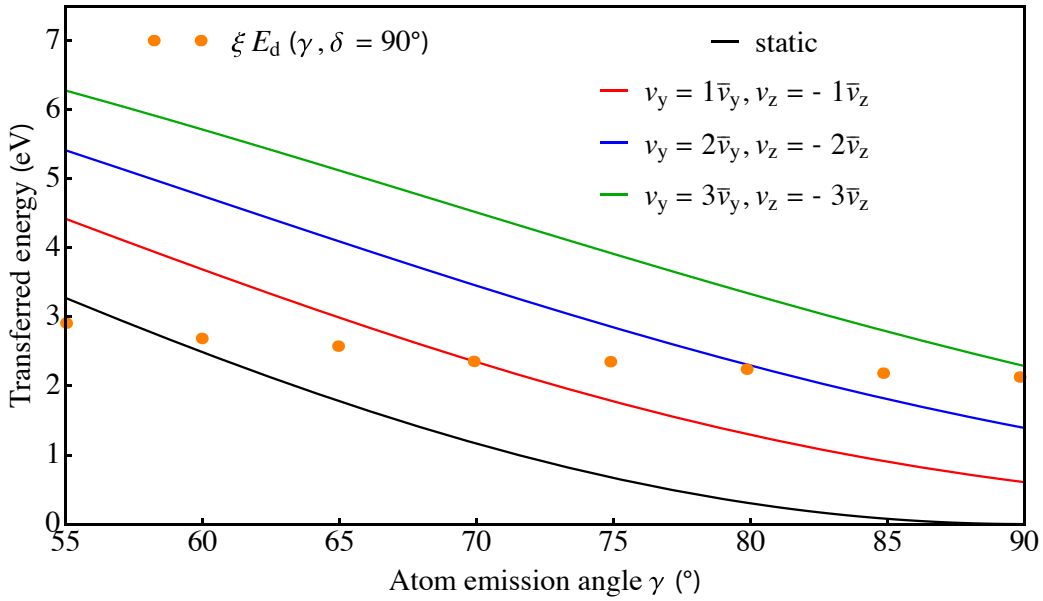

Figure 3.13: Energy transfer to a N atom from a 60-keV electron. Scaled displacement thresholds ξE_d (orange dots, $\xi = 0.224$) that will lead to a jump compared to transferred energies as a function of polar atom emission angle γ compared to transferred energies for different velocity components (solid lines). The energy transfer across the vacancy is greatest for positive $\overline{v}_y$ and negative $\overline{v}_z$ velocity components.

Table 3.3: Experimental cross-sections for the N–C_2 jumps compared to the out-of-plane σ_{v_z} and the 3D σ_{3D} vibrational theoretical models.

E_e [keV]	σ_{exp} jump [barn]	σ_{exp} KO [barn]	σ_{v_z} [barn]	σ_{3D} [barn]	σ_{3D} adatom [barn]
55	16.9 ± 3.0	-	18.08	17.27	7.01
60	22.4 ± 4.3	1.54 ± 0.72	20.64	20.82	12.12

3.6 Temperature-dependent displacement thresholds

Finally, we performed temperature-dependent DFTB/MD simulations for graphene with a Si impurity or a pyridinic N site using the methodology described in Section 2.4. For both systems we used a 15×15×1 graphene supercell with the respective impurities located in the middle of the cell. We sampled 212 trajectories at 300 K for the Si-C_3 system and 241 trajectories for the pyridinic N. We tested different angular ranges and noticed that in most cases the target atom either completely displaced or did not switch places with the Si atom, likely due to DFTB+ calculator not being as accurate in describing this process as DFT. Therefore we settled for just one ejection direction in both systems. The C atom next to the silicon impurity was always displaced in a direction away from the Si atom at an polar angle of $\gamma = 15°$. In the non-thermalized state, DFTB yielded a displacement threshold $E_\mathrm{d} = 13.6$ eV compared to 14.56 eV calculated with DFT. The nitrogen atom was displaced towards the center of the vacancy at an angle $\gamma = 90°$. Here DFTB+ yielded a displacement threshold of 9.1 eV for the non-thermalized case which is close to the 9.5 eV value calculated with DFT. Sampling different thermalized states, the histograms in Fig. 3.14 represent the spread of the displacement threshold energies and the red curves represent normal distributions fits. We tried to use the standard deviation w to evaluate the temperature-dependent cross-section integral described by Eq. 3.33 for the Si–C_3 system. However, due to the now 6-dimensional and piecewise-restrained numerical integral, the `GlobalAdaptive` algorithm of Mathematica could not provide us with a numerically stable cross-section value for the pyridinic N site.

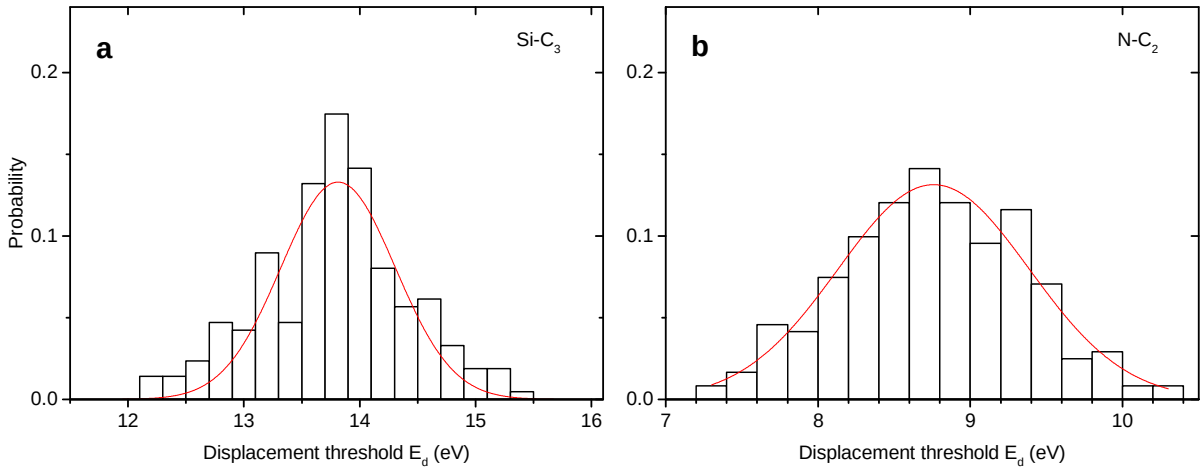

Figure 3.14: Histograms representing the distribution of displacement threshold energies for Si-C_3 (a) and N-C_2 (b) from temperature-dependent displacement simulations. The red curves are Gaussian fits with a standard deviation $w = 0.49$ eV for Si-C_3 and $w = 0.62$ eV for N-C_2.

Chapter 4

Conclusion

The electron beam is a powerful tool for imaging the atomic structure of materials. Often, it may damage them, but sometimes it can also induce interesting dynamics. The main mechanism for these events in graphene are elastic knock-on displacements. This work presents a complete description of knock-on between electrons and nuclei, and provides new insights into the physics of manipulating single atoms. The elastic interaction between an electron and a target atom has been accounted for the first time including atom vibrations in all directions. The energy transfer from an electron to a nucleus can be described as a function of both the polar and azimuthal electron scattering angles, which in turn determine the atom emission angles, as well as the three velocity components of the vibrating nucleus. The energy required to displace an atom, the displacement threshold energy, is not assumed to be isotropic, but to vary as a function of the atomic emissions angles, opening the way to studying beam-induced dynamics in arbitrary directions. We have tested this theory on pristine graphene, graphene with silicon impurities, and graphene with a pyridinic nitrogen impurity site.

For pristine graphene, the new model yielded a very similar result to the earlier out-of-plane velocity model. Since the difference between the two models is negligible and no major improvement to the predicted cross section is observed, we can conclude that the v_z-only model is sufficient for describing knock-on in graphene. There is little reason to expect that in-plane components would play a major role in the displacement of C atoms from pristine graphene.

In the case of Si-doped graphene, all the models we tested proved to be a poor match for the experimental data. Regardless of the choice of fitting parameters, none of the models could

explain the observed rates, especially at 60 and 65 keV. The pyridinic N site, which shows reversible jumping dynamics is one of the most stringent possible tests of our 3D elastic theory, as in-plane components should play a major role here. However, the predicted threshold energies were far from agreement with the experiment.

Since vibrations and the variation of the threshold energy as a function of emission angles are included, we conclude that the discrepancies must be caused by inelastic effects, which are not treated in this study, and have been shown to explain damage in other non-metallic 2D materials [73, 111]. It is surprising that they seem to also play an important role at impurity sites in metallic graphene. Future theoretical developments for describing inelastic excitations in combination with elastic knock-on can be expected to give valuable insights into the observed dynamics, and to be better able to describe the experimental data.

List of publications and conference contributions

Publications

Alexandru Chirita, Toma Susi and Jani Kotakoski. Influence of temperature on the displacement threshold energy in graphene, *Scientific Reports* 9, 12981 (2019).

Alexandru Chirita, Alexander Markevich, Mukesh Tripathi, Nicholas A. Pike, Matthieu J. Verstraete, Jani Kotakoski, and Toma Susi. Three-dimensional ab initio description of vibration-assisted electron knock-on displacements in graphene, *Physical Review B* 105, 235419 (2022). (Contribution: theoretical framework for the 3D electron-atom elastic interaction, MD simulations, and analysis of the results.)

Manuscripts in preparation

Andreas Postl, Alexandru Chirita, Nicholas A. Pike, Matthieu J. Verstraete, Jani Kotakoski, Toma Susi, *Electron irradiation cross sections for graphene's silicon impurities*. (Contribution: simulation of the 3D variation of the displacement threshold energy, and of the 3D contribution of vibrations to the elastic displacement cross section.)

Thuy An Bui, Gregor T. Leuthner, Jacob Madsen, Carsten Speckmann, Alexandru I. Chirita, Clemens Mangler, Jani Kotakoski, and Toma Susi, *Electron irradiation damage of hexagonal boron nitride*. (Contribution: modeling of the 3D contribution of vibrations to the elastic displacement cross section.)

Conference participation

Graphene Study Winter 2018, 5-10 February, Obergurgl, Austria.

Conference on Physics of Defects in Solids: *Quantum Mechanics Meets Topology 2018*, 9-13 July, Trieste, Italy.

Towards Reality in Nanoscale Materials IX Workshop, 12-14 February 2019, Levi, Finland.

Physics Boat, Atomic structure of nanosystems from first-principles simulations and microscopy experiments (AS-SIMEX 2019), 28-30 May 2019 , Helsinki, Finland - Stockholm, Sweden.

Towards understanding and modelling intense electronic excitations (TUMIEE) Training school, 23 September - 4 October 2019, Rethymno, Crete (Greece).

Conference proceedings

Alexandru Chirita, Alexander Markevich, Jani Kotakoski, and Toma Susi. "Atomistic Understanding of Damage and Beam-driven Dynamics in 2D Materials." *Microscopy and Microanalysis 26*, no. S2 (2020): 542-543.

Gregor Leuthner, Thuy An Bui, Georg Zagler, Bernhard Fickl, Mohammad Monazam, Alexandru Chirita, Toma Susi, and Jani Kotakoski. "Quantitative Measurement and Utilization of Electron Irradiation Effects in 2D Materials." *Microscopy and Microanalysis 26*, no. S2 (2020): 166-166.

Andreas Postl, Thuy An Bui, Fabian Kraft, Alexandru Chirita, Gregor Leuthner, Heena Inani, Clemens Mangler, Kimmo Mustonen, Jani Kotakoski, and Toma Susi. "Adventures in Atomic Resolution in situ STEM." *Microscopy and Microanalysis 28*, no. S1 (2022): 2342-2343.

Appendix A

Simulation codes

A.1 Unit cell construction of graphene

```
import numpy.math.sqrt as sqrt
from ase import Atoms, io

# add 2 Carbon atoms
a = Atoms('C2')

# nearest neighbour carbon-carbon distance
a0=1.42

#set the unit cell vectors and scaled positions
a.set_cell([[a0*3/2,a0*sqrt(3)/2,0],[a0*3/2,-a0*sqrt(3)/2,0],
[0,0,10]])
a.set_scaled_positions([[1./3,1./3,0],[2./3,2./3,0]])
io.write('graphene_unit_cell.POSCAR',a)
```

A.2 DFTB+ thermalization

```
import os
from ase import Atoms
from ase.calculators.dftb import Dftb
from ase.io import Trajectory
from ase import io
from ase.md.velocitydistribution import (MaxwellBoltzmannDistribution,Stationary)
from ase.md.verlet import VelocityVerlet
from ase import units
import numpy as np
import sys

fname = 'Si_gra_sc15'
system = io.read(sys.argv[1])

calc = Dftb(label='carbon',
            atoms=system,
            #run_manyDftb_steps=True,
            kpts=(1,1,1),
            #Driver_='VelocityVerlet',
            #Driver_MaxForceComponent='1E-4',
            #Driver_MaxSteps=1000,
            Hamiltonian_MaxAngularMomentum_='',
            Hamiltonian_MaxAngularMomentum_C='"p"',
            Hamiltonian_MaxAngularMomentum_Si='"p"')
system.set_calculator(calc)



temperature = 600
```

```
name=fname+"_MB_300Kelvin"
traj = Trajectory(name+".traj", 'w', system, properties={"energy",
"velocities", "forces"})

MaxwellBoltzmannDistribution(system, temperature_K = temperature)
Stationary(system) # so that the atoms dont drift in any direction

# We run MD with constant energy using the VelocityVerlet algorithm.
dyn = VelocityVerlet(system, 1 * units.fs)  # 1 fs time step.

dyn.attach(traj.write, interval=1)
dyn.run(5000)

traj.close()
```

A.3 DFTB+ temperature-dependent displacement simulations for Si-doped graphene

```
import sys, os, math
import numpy as np
from ase import io
from ase import Atom
from ase.calculators.dftb import Dftb
from ase.io.dftb import read_dftb_velocities, write_dftb_velocities
from ase.md.velocitydistribution import MaxwellBoltzmannDistribution
from ase.md.verlet import VelocityVerlet
from ase import units

from ase.io import Trajectory, read

#load the trajectories / thermalized structure frames
path = os.getcwd() #uses current working directory (cwd)
trajectories = []
for root, dirs, files in os.walk(path):
  for name in files:
    if name.endswith('.traj'):
     trajectories.append(name)



at = int(sys.argv[1])
delta = float(sys.argv[2])
gammaval = [-15]

#displacement threshold energy values
tdvalues = np.arange (13.4, 17.6, 0.1)
```

```
flog = open("displacement_log.txt",'w')



for f in trajectories:
  atoms = io.read(f)
  atoms2 = atoms.copy()
  name = os.path.splitext(f)[0]

  for gamma in gammaval :

    flog.write(name+", gamma= "+str(gamma)+", ")

    for E in tdvalues :

            atoms = atoms2.copy()

            outname = name + "_at" + str(at) + "_E" + str(E)
            #set DFTB

            calc = Dftb(label = 'carbon',
                        atoms = atoms2,
                        kpts=(1,1,1),
                        Hamiltonian_MaxAngularMomentum_= '',
                        Hamiltonian_MaxAngularMomentum_C= '"p"',
                        Hamiltonian_MaxAngularMomentum_Si= '"p"'
                        )


            atoms.set_calculator(calc)
```

```
dyn = VelocityVerlet(atoms, 0.3*units.fs)
traj = Trajectory(outname + '.traj', 'w',atoms)
dyn.attach(traj.write, interval=1)
dyn.run(1)

v = (2*float(E)/atoms[at].mass)**0.5

vx = v * math.sin(math.pi*gamma/180)*math.cos(math.pi*delta/180)
vy = v * math.sin(math.pi*gamma/180)*math.sin(math.pi*delta/180)
vz = v * math.cos(math.pi*gamma/180)

atoms[at].momentum[0]=atoms[at].mass * vx
atoms[at].momentum[1]=atoms[at].mass * vy
atoms[at].momentum[2]=atoms[at].mass * vz
dyn.run(850)

flog.write('\n')
traj.close()
if atoms[224].position[0] < 7.4 and atoms[224].position[2] < 3.3 :
   flog.write('E = '+str(E))
   flog.write('\n')
   break
elif atoms[at].position[2] > 5 :
   flog.write('ejected at = '+str(E))
   flog.write('\n')
   break
```

A.4 DFT-MD displacement simulations for pristine graphene

```
import sys, os, math
import numpy as np
from ase import io
from ase import Atom
from ase.units import Bohr
from gpaw import GPAW, FermiDirac
from gpaw import restart
from ase.md.velocitydistribution import MaxwellBoltzmannDistribution
from ase.md.verlet import VelocityVerlet
from ase import units
from ase.io import Trajectory, read

filename = str(sys.argv[1])
name = os.path.splitext(filename)[0]

atoms = io.read(filename)
atoms2 = atoms.copy()

at = int(sys.argv[2])
alpha = float(sys.argv[3]) # Spherical angle alpha

betaval = [20,30]
tdvalues = [22.85,22.9,22.95,23.0,23.05,23.1,23.15,23.2,23.25]
flog = open("displacement_log.txt",'a')

def checkejected(a=atoms):  # store a reference to atoms in the definition.

    if atoms[at].position[2] > 15.5 :
        flog.write('\n')
```

```
            flog.write(str(E))
            return False
        if atoms.get_velocities()[at,2] < 0 :
            flog.write("not ejected")
            return False
        else:
            return True

for beta in betaval :
    for E in tdvalues :

            flog.write("beta="+str(beta)+", E="+str(E)+",")
            atoms = atoms2.copy()

            outname = name + "_at" + str(at) + "_E" + str(E)
            #set gpaw
            myk=3
            calc = GPAW(mode='lcao',
                        xc = 'PBE',
                        basis='dzp',
                        kpts=(myk, myk, 1),
                        occupations=FermiDirac(0.025),
                        txt = 'out',
                        gpts=(80, 80, 96),
                        symmetry={'point_group': False},
                        parallel=dict(sl_auto=True, augment_grids=True, band=1),
                         )
```

```
atoms.set_calculator(calc)

MaxwellBoltzmannDistribution(atoms,1*units.kB)

dyn = VelocityVerlet(atoms, 0.3*units.fs)
traj = Trajectory(outname + '.traj', 'w',atoms)
dyn.attach(traj.write, interval=1)
dyn.run(1)
#attach the observer
dyn.attach(checkejected,interval=1)

v = (2*float(E)/atoms[at].mass)**0.5

vx = v * math.sin(math.pi*beta/180)*math.cos(math.pi*alpha/180)
vy = v * math.sin(math.pi*beta/180)*math.sin(math.pi*alpha/180)
vz = v * math.cos(math.pi*beta/180)

atoms[at].momentum[0]=atoms[at].mass * vx
atoms[at].momentum[1]=atoms[at].mass * vy
atoms[at].momentum[2]=atoms[at].mass * vz
while checkejected(atoms) == True:

      dyn.run(1)

flog.write("\n")
traj.close()
if atoms[at].position[2] > 15.5 :
   break
```

Solution to the energy transfer in terms of atom emission angles

```
In[•]:= M = MC (*Redefine symbol for the mass of C12 atom to simplify notation.*);

(*Solving for the transferred energy in terms of gamma and delta resulted in two solutions to the
 equation and therefore we have Tmaxcase11 and Tmaxcase12*)
Tmaxcase11[vx_, vy_, vz_, U_, delta_, gamma_] :=
 (-1/(2 c^2 M)) (-2 Te[U]^2 Cos[gamma]^2 - 4 c^2 Te[U] m Cos[gamma]^2 - 2 c^2 Sqrt[Te[U] (Te[U]/c^2 + 2 m)] M vz Cos[gamma]^2 -
    c^2 M^2 vz^2 Cos[gamma]^2 + c^2 M^2 vx^2 Cos[delta]^2 Cos[gamma]^2 + c^2 M^2 vy^2 Cos[delta]^2 Cos[gamma]^2 +
    c^2 M^2 vx^2 Cos[gamma]^2 Sin[delta]^2 + c^2 M^2 vy^2 Cos[gamma]^2 Sin[delta]^2 -
    4 c^2 Sqrt[Te[U] (Te[U]/c^2 + 2 m)] M vx Cos[delta] Cos[gamma] Sin[gamma] - 4 c^2 M^2 vx vz Cos[delta] Cos[gamma] Sin[gamma] -
    4 c^2 Sqrt[Te[U] (Te[U]/c^2 + 2 m)] M vy Cos[gamma] Sin[delta] Sin[gamma] - 4 c^2 M^2 vy vz Cos[gamma] Sin[delta] Sin[gamma] +
    2 c^2 Sqrt[Te[U] (Te[U]/c^2 + 2 m)] M vz Sin[gamma]^2 + c^2 M^2 vz^2 Sin[gamma]^2 - c^2 M^2 vx^2 Cos[delta]^2 Sin[gamma]^2 +
    c^2 M^2 vy^2 Cos[delta]^2 Sin[gamma]^2 - 4 c^2 M^2 vx vy Cos[delta] Sin[delta] Sin[gamma]^2 + c^2 M^2 vx^2 Sin[delta]^2 Sin[gamma]^2 -
    c^2 M^2 vy^2 Sin[delta]^2 Sin[gamma]^2 +
    1/4 c^2 Sqrt[-1/c^2 16 M^2 (4 Te[U]^2 vz^2 + c^2 (8 Te[U] m vz^2 + 4 Sqrt[Te[U] (Te[U]/c^2 + 2 m)] M vz (vx^2 + vy^2 + vz^2) + M^2 (vx^2 + vy^2 + vz^2)^2)) +
      1/c^4 16 ((2 Te[U]^2 + 4 c^2 Te[U] m + c^2 M (2 Sqrt[Te[U] (Te[U]/c^2 + 2 m)] vz - M (vx^2 + vy^2 - vz^2))) Cos[gamma]^2 +
        c^2 M ((-vz (2 Sqrt[Te[U] (Te[U]/c^2 + 2 m)] + M vz) + M (vx^2 - vy^2) Cos[2 delta] + 2 M vx vy Sin[2 delta]) Sin[gamma]^2 +
          2 (Sqrt[Te[U] (Te[U]/c^2 + 2 m)] + M vz) (vx Cos[delta] + vy Sin[delta]) Sin[2 gamma])^2))) / e;
Tmaxcase12[vx_, vy_, vz_, U_, delta_, gamma_] :=
 1/(2 c^2 M)
  (2 Te[U]^2 Cos[gamma]^2 + 4 c^2 Te[U] m Cos[gamma]^2 + 2 c^2 Sqrt[Te[U] (Te[U]/c^2 + 2 m)] M vz Cos[gamma]^2 + c^2 M^2 vz^2 Cos[gamma]^2 -
    c^2 M^2 vx^2 Cos[delta]^2 Cos[gamma]^2 - c^2 M^2 vy^2 Cos[delta]^2 Cos[gamma]^2 - c^2 M^2 vx^2 Cos[gamma]^2 Sin[delta]^2 -
    c^2 M^2 vy^2 Cos[gamma]^2 Sin[delta]^2 + 4 c^2 Sqrt[Te[U] (Te[U]/c^2 + 2 m)] M vx Cos[delta] Cos[gamma] Sin[gamma] +
    4 c^2 M^2 vx vz Cos[delta] Cos[gamma] Sin[gamma] + 4 c^2 Sqrt[Te[U] (Te[U]/c^2 + 2 m)] M vy Cos[gamma] Sin[delta] Sin[gamma] +
    4 c^2 M^2 vy vz Cos[gamma] Sin[delta] Sin[gamma] - 2 c^2 Sqrt[Te[U] (Te[U]/c^2 + 2 m)] M vz Sin[gamma]^2 -
    c^2 M^2 vz^2 Sin[gamma]^2 + c^2 M^2 vx^2 Cos[delta]^2 Sin[gamma]^2 - c^2 M^2 vy^2 Cos[delta]^2 Sin[gamma]^2 +
    4 c^2 M^2 vx vy Cos[delta] Sin[delta] Sin[gamma]^2 - c^2 M^2 vx^2 Sin[delta]^2 Sin[gamma]^2 + c^2 M^2 vy^2 Sin[delta]^2 Sin[gamma]^2 +
    1/4 c^2 Sqrt[-1/c^2 16 M^2 (4 Te[U]^2 vz^2 + c^2 (8 Te[U] m vz^2 + 4 Sqrt[Te[U] (Te[U]/c^2 + 2 m)] M vz (vx^2 + vy^2 + vz^2) + M^2 (vx^2 + vy^2 + vz^2)^2)) +
      1/c^4 16 ((2 Te[U]^2 + 4 c^2 Te[U] m + c^2 M (2 Sqrt[Te[U] (Te[U]/c^2 + 2 m)] vz - M (vx^2 + vy^2 - vz^2))) Cos[gamma]^2 + c^2
        M ((-vz (2 Sqrt[Te[U] (Te[U]/c^2 + 2 m)] + M vz) + M (vx^2 - vy^2) Cos[2 delta] + 2 M vx vy Sin[2 delta]) Sin[gamma]^2 +
          2 (Sqrt[Te[U] (Te[U]/c^2 + 2 m)] + M vz) (vx Cos[delta] + vy Sin[delta]) Sin[2 gamma])^2))) / e;
```

Figure A.1: Screenshot of the solution to the energy transfer in terms of atom emission angles γ and δ.

Bibliography

1. Sines, G. & Sakellarakis, Y. A. Lenses in antiquity. *American Journal of Archaeology,* 191–196 (1987).
2. Van Helden, A., Dupré, S. & van Gent, R. *The origins of the telescope* (Amsterdam University Press, 2010).
3. Hooke, R. *Micrographia: or some physiological descriptions of minute bodies made by magnifying glasses, with observations and inquiries thereupon* (Courier Corporation, 2003).
4. Van Leewenhoeck, A. Observations, communicated to the Publisher by Mr. Antony van Leewenhoeck, in a Dutch letter of the 9th of Octob. 1676. Here English'd: concerning little animals by him observed in rain-Well-Sea. And snow water; as also in water wherein pepper had lain infused. *Philosophical Transactions (1665-1678)* **12,** 821–831 (1665).
5. Abbe, E. Beiträge zur Theorie des Mikroskops und der mikroskopischen Wahrnehmung. *Archiv für mikroskopische Anatomie* **9,** 413–468 (1873).
6. Ruska, E. & Knoll, M. Die magnetische Sammelspule für schnelle Elektronenstrahlen. *The magnetic concentrating coil for fast electron beams.) Z. techn. Physik* **12,** 389–400 (1931).
7. Ruska, E., Binnig, G. & Rohrer, H. Nobel lecture. *The development of the electron microscope and of electron microscopy. Nobel Lecture, December* **8** (1986).
8. Broglie, L. d. A tentative theory of light quanta. *The London, Edinburgh, and Dublin Philosophical Magazine and Journal of Science* **47,** 446–458 (1924).
9. Scherzer, O. Spharische und chromatische korrektur von elektronen-linsen. *Optik* **2,** 114–132 (1947).

10. Zach, J. & Haider, M. Aberration correction in a low voltage SEM by a multipole corrector. *Nuclear Instruments and Methods in Physics Research Section A: Accelerators, Spectrometers, Detectors and Associated Equipment* **363,** 316–325 (1995).

11. Von Ardenne, M. Das elektronen-rastermikroskop. *Zeitschrift für Physik* **109,** 553–572 (1938).

12. Crewe, A. V., Isaacson, M. & Johnson, D. A simple scanning electron microscope. *Review of Scientific Instruments* **40,** 241–246 (1969).

13. Crewe, A. V., Wall, J. & Langmore, J. Visibility of single atoms. *Science* **168,** 1338–1340 (1970).

14. Krivanek, O., Dellby, N. & Lupini, A. Towards sub-Å electron beams. *Ultramicroscopy* **78,** 1–11 (1999).

15. Krivanek, O., Nellist, P., Dellby, N., Murfitt, M. & Szilagyi, Z. Towards sub-0.5 Å electron beams. *Ultramicroscopy* **96,** 229–237 (2003).

16. Novoselov, K. S. *et al.* Electric Field Effect in Atomically Thin Carbon Films. *Science* **306,** 666–669 (2004).

17. Meyer, J. C., Girit, C. O., Crommie, M. & Zettl, A. Imaging and dynamics of light atoms and molecules on graphene. *Nature* **454,** 319–322 (2008).

18. Rutherford, E. The scattering of α and β particles by matter and the structure of the atom. *The London, Edinburgh, and Dublin Philosophical Magazine and Journal of Science* **21,** 669–688 (1911).

19. Mott, N. F. The scattering of electrons by atoms. *Proceedings of the Royal Society of London. Series A, Containing Papers of a Mathematical and Physical Character* **127,** 658–665 (1930).

20. McKinley Jr, W. A. & Feshbach, H. The coulomb scattering of relativistic electrons by nuclei. *Physical Review* **74,** 1759 (1948).

21. Banhart, F. Irradiation effects in carbon nanostructures. *Reports on Progress in Physics* **62,** 1181 (1999).

22. Meyer, J. C. *et al.* Accurate measurement of electron beam induced displacement cross sections for single-layer graphene. *Physical Review Letters* **108,** 196102 (2012).

23. Komsa, H.-P. *et al.* Two-Dimensional Transition Metal Dichalcogenides under Electron Irradiation: Defect Production and Doping. *Physical Review Letters* **109,** 035503 (2012).

24. Susi, T. *et al.* Isotope analysis in the transmission electron microscope. *Nature Communications* **7,** 13040 (2016).

25. Chirita Mihaila, A. I., Susi, T. & Kotakoski, J. Influence of temperature on the displacement threshold energy in graphene. *Scientific Reports* **9,** 12981 (2019).

26. Susi, T., Meyer, J. C. & Kotakoski, J. Manipulating low-dimensional materials down to the level of single atoms with electron irradiation. *Ultramicroscopy* **180,** 163–172 (2017).

27. Tripathi, M. *et al.* Electron-beam manipulation of silicon dopants in graphene. *Nano Letters* **18,** 5319–5323 (2018).

28. Lin, Y.-C. *et al.* Structural and chemical dynamics of pyridinic-nitrogen defects in graphene. *Nano Letters* **15,** 7408–7413 (2015).

29. Haider, M. *et al.* Electron microscopy image enhanced. *Nature* **392,** 768–769 (1998).

30. Nellist, P. D. *et al.* Direct sub-angstrom imaging of a crystal lattice. *Science* **305,** 1741–1741 (2004).

31. Hawkes, P. Aberration correction past and present. *Philosophical Transactions of the Royal Society of London A: Mathematical, Physical and Engineering Sciences* **367,** 3637–3664 (2009).

32. Scherzer, O. Über einige fehler von elektronenlinsen. *Zeitschrift für Physik* **101,** 593–603 (1936).

33. Peierls, R. Quelques propriétés typiques des corps solides. fre. *Annales de l'institut Henri Poincaré* **5,** 177–222 (1935).

34. Landau, L. D. Zur Theorie der phasenumwandlungen II. *Phys. Z. Sowjetunion* **11,** 26–35 (1937).

35. Ludacka, U. *et al.* In situ control of graphene ripples and strain in the electron microscope. *npj 2D Materials and Applications* **2,** 1–6 (2018).

36. Meyer, J. C. *et al.* The structure of suspended graphene sheets. *Nature* **446,** 60–63 (2007).

37. DiVincenzo, D. & Mele, E. Self-consistent effective-mass theory for intralayer screening in graphite intercalation compounds. *Phys. Rev. B* **29,** 1685 (1984).

38. Berger, C. *et al.* Ultrathin epitaxial graphite: 2D electron gas properties and a route toward graphene-based nanoelectronics. *The Journal of Physical Chemistry B* **108,** 19912–19916 (2004).

39. Berger, C. *et al.* Electronic confinement and coherence in patterned epitaxial graphene. *Science* **312,** 1191–1196 (2006).

40. Novoselov, K. S. *et al.* Room-temperature quantum Hall effect in graphene. *Science* **315,** 1379–1379 (2007).

41. Novoselov, K. S. *et al.* Two-dimensional gas of massless Dirac fermions in graphene. *Nature* **438,** 197–200 (2005).

42. Lee, C., Wei, X., Kysar, J. W. & Hone, J. Measurement of the elastic properties and intrinsic strength of monolayer graphene. *Science* **321,** 385–388 (2008).

43. Balandin, A. A. *et al.* Superior thermal conductivity of single-layer graphene. *Nano Letters* **8,** 902–907 (2008).

44. Bao, W. *et al.* Controlled ripple texturing of suspended graphene and ultrathin graphite membranes. *Nature Nanotechnology* **4,** 562–566 (2009).

45. Peres, N. M. R., Guinea, F. & Castro Neto, A. H. Electronic properties of disordered two-dimensional carbon. *Phys. Rev. B* **73,** 125411 (12 2006).

46. Bauer, W. & Sosin, A. Threshold Displacement Energies and Subthreshold Displacements in Copper and Gold Near 10° K. *Journal of Applied Physics* **35,** 703–709 (1964).

47. Jung, P., Chaplin, R., Fenzl, H., Reichelt, K. & Wombacher, P. Anisotropy of the threshold energy for production of Frenkel pairs in copper and platinum. *Phys. Rev. B* **8,** 553 (1973).

48. Kotakoski, J. *et al.* Stone-Wales-type transformations in carbon nanostructures driven by electron irradiation. *Phys. Rev. B* **83,** 245420 (2011).

49. Banhart, F., Kotakoski, J. & Krasheninnikov, A. V. Structural defects in graphene. *ACS Nano* **5,** 26–41 (2011).

50. Meyer, J. C. *et al.* Direct imaging of lattice atoms and topological defects in graphene membranes. *Nano Letters* **8,** 3582–3586 (2008).

51. Ramasse, Q. M. *et al.* Probing the bonding and electronic structure of single atom dopants in graphene with electron energy loss spectroscopy. *Nano Letters* **13,** 4989–4995 (2013).

52. Lee, J., Zhou, W., Pennycook, S. J., Idrobo, J.-C. & Pantelides, S. T. Direct visualization of reversible dynamics in a Si6 cluster embedded in a graphene pore. *Nature Communications* **4,** 1–7 (2013).

53. Yang, Z. *et al.* Direct observation of atomic dynamics and silicon doping at a topological defect in graphene. *Angewandte Chemie* **126,** 9054–9058 (2014).

54. Kepaptsoglou, D. *et al.* Electronic structure modification of ion implanted graphene: the spectroscopic signatures of p-and n-type doping. *ACS Nano* **9,** 11398–11407 (2015).

55. Susi, T. *et al.* Towards atomically precise manipulation of 2D nanostructures in the electron microscope. *2D Materials* **4,** 042004 (2017).

56. Tripathi, M. *et al.* Implanting germanium into graphene. *ACS Nano* **12,** 4641–4647 (2018).

57. Chirita, A. *et al.* Three-dimensional ab initio description of vibration-assisted electron knock-on displacements in graphene. *Phys. Rev. B* **105,** 235419 (2022).

58. Nosraty Alamdary, D., Kotakoski, J. & Susi, T. Structure and energetics of embedded Si patterns in graphene. *physica status solidi (b)* **254,** 1700188 (2017).

59. Wang, X. *et al.* Heteroatom-doped graphene materials: syntheses, properties and applications. *Chemical Society Reviews* **43,** 7067–7098 (2014).

60. Ullah, S. *et al.* Advances and trends in chemically doped graphene. *Advanced Materials Interfaces* **7,** 2000999 (2020).

61. Varela, M. *et al.* Spectroscopic imaging of single atoms within a bulk solid. *Physical Review Letters* **92,** 095502 (2004).

62. Ramasse, Q. M. *et al.* Direct experimental evidence of metal-mediated etching of suspended graphene. *ACS Nano* **6,** 4063–4071 (2012).

63. Hofer, C. *et al.* Direct visualization of the 3D structure of silicon impurities in graphene. *Applied Physics Letters* **114,** 053102 (2019).

64. Susi, T. *et al.* Silicon–carbon bond inversions driven by 60-keV electrons in graphene. *Physical Review Letters* **113,** 115501 (2014).

65. Zagler, G. *et al.* Beam-driven dynamics of aluminium dopants in graphene. *2D Materials* **9,** 035009 (2022).

66. Chuvilin, A., Meyer, J. C., Algara-Siller, G. & Kaiser, U. From graphene constrictions to single carbon chains. *New Journal of Physics* **11,** 083019 (2009).

67. Jin, C., Lan, H., Peng, L., Suenaga, K. & Iijima, S. Deriving Carbon Atomic Chains from Graphene. *Physical Review Letters* **102,** 205501 (2009).

68. Chuvilin, A., Kaiser, U., Bichoutskaia, E., Besley, N. A. & Khlobystov, A. N. Direct transformation of graphene to fullerene. *Nat. Chem* **2,** 450–453 (2010).

69. Kotakoski, J., Krasheninnikov, A. V., Kaiser, U. & Meyer, J. C. From Point Defects in Graphene to Two-Dimensional Amorphous Carbon. *Physical Review Letters* **106,** 105505 (2011).

70. Vajda, P. Anisotropy of electron radiation damage in metal crystals. *Reviews of Modern Physics* **49,** 481 (1977).

71. Kinchin, G. & Pease, R. The displacement of atoms in solids by radiation. *Reports on Progress in Physics* **18,** 1 (1955).

72. Zobelli, A., Gloter, A., Ewels, C., Seifert, G. & Colliex, C. Electron knock-on cross section of carbon and boron nitride nanotubes. *Phys. Rev. B* **75,** 245402 (2007).

73. Susi, T., Meyer, J. C. & Kotakoski, J. Quantifying transmission electron microscopy irradiation effects using two-dimensional materials. *Nature Reviews Physics* **1,** 397–405 (2019).

74. Lehnert, T., Lehtinen, O., Algara–Siller, G. & Kaiser, U. Electron radiation damage mechanisms in 2D MoSe2. *Applied Physics Letters* **110,** 033106 (2017).

75. Despoja, V., Mowbray, D. J., Vlahović, D. & Marušić, L. TDDFT study of time-dependent and static screening in graphene. *Phys. Rev. B* **86,** 195429 (2012).

76. Yan, H. *et al.* Damping pathways of mid-infrared plasmons in graphene nanostructures. *Nature Photonics* **7,** 394–399 (2013).

77. Iglesias, J. M., Martin, M. J., Pascual, E. & Rengel, R. Hot carrier and hot phonon coupling during ultrafast relaxation of photoexcited electrons in graphene. *Applied Physics Letters* **108,** 043105 (2016).

78. Li, J. *et al.* Nature of exciton transitions in hexagonal boron nitride. *Applied physics letters* **108,** 122101 (2016).

79. Kozawa, D. *et al.* Photocarrier relaxation pathway in two-dimensional semiconducting transition metal dichalcogenides. *Nature Communications* **5,** 1–7 (2014).

80. Paquet, E. & Viktor, H. L. Molecular dynamics, Monte Carlo simulations, and Langevin dynamics: a computational review. *BioMed research international* **2015** (2015).

81. Newton, I. *Sir Isaac Newton's mathematical principles of natural philosophy and his system of the world* (Univ of California Press, 1962).

82. Allen, M. P. *et al.* Introduction to molecular dynamics simulation. *Computational soft matter: from synthetic polymers to proteins* **23,** 1–28 (2004).

83. Dollfus, P. *et al. Simulation of Transport in Nanodevices* (John Wiley & Sons, 2016).

84. Verlet, L. Computer" experiments" on classical fluids. I. Thermodynamical properties of Lennard-Jones molecules. *Physical Review* **159,** 98 (1967).

85. Swope, W. C., Andersen, H. C., Berens, P. H. & Wilson, K. R. A computer simulation method for the calculation of equilibrium constants for the formation of physical clusters of molecules: Application to small water clusters. *The Journal of Chemical Physics* **76,** 637–649 (1982).

86. Born, M. & Oppenheimer, R. Zur quantentheorie der molekeln. *Annalen der Physik* **389,** 457–484 (1927).

87. Hohenberg, P. & Kohn, W. Inhomogeneous electron gas. *Physical Review* **136,** B864 (1964).

88. Kohn, W. & Sham, L. J. Self-consistent equations including exchange and correlation effects. *Physical review* **140,** A1133 (1965).

89. Perdew, J. P. & Wang, Y. Accurate and simple analytic representation of the electron-gas correlation energy. *Phys. Rev. B* **45,** 13244 (1992).

90. Perdew, J. P., Burke, K. & Ernzerhof, M. Generalized gradient approximation made simple. *Physical Review Letters* **77,** 3865 (1996).

91. Porezag, D., Frauenheim, T., Köhler, T., Seifert, G. & Kaschner, R. Construction of tight-binding-like potentials on the basis of density-functional theory: Application to carbon. *Phys. Rev. B* **51,** 12947 (1995).

92. Seifert, G., Porezag, D. & Frauenheim, T. Calculations of molecules, clusters, and solids with a simplified LCAO-DFT-LDA scheme. *International Journal of Quantum Chemistry* **58,** 185–192 (1996).

93. Elstner, M. *et al.* Self-consistent-charge density-functional tight-binding method for simulations of complex materials properties. *Phys. Rev. B* **58,** 7260 (1998).

94. Malola, S., Häkkinen, H. & Koskinen, P. Raman spectra of single-walled carbon nanotubes with vacancies. *Phys. Rev. B* **77,** 155412 (2008).

95. Gaus, M., Cui, Q. & Elstner, M. DFTB3: extension of the self-consistent-charge density-functional tight-binding method (SCC-DFTB). *J. Chem. Theory Comput* **7,** 931–948 (2011).

96. Haario, H., Saksman, E. & Tamminen, J. An adaptive Metropolis algorithm. *Bernoulli,* 223–242 (2001).

97. Andersen, M., Panosetti, C. & Reuter, K. A practical guide to surface kinetic Monte Carlo simulations. *Frontiers in Chemistry* **7,** 202 (2019).

98. Young, W. & Elcock, E. Monte Carlo studies of vacancy migration in binary ordered alloys: I. *Proceedings of the Physical Society (1958-1967)* **89,** 735 (1966).

99. Cai, W., Bulatov, V. V., Justo, J. F., Argon, A. S. & Yip, S. Kinetic Monte Carlo approach to modeling dislocation mobility. *Computational Materials Science* **23,** 124–130 (2002).

100. Dirac, P. A. M. The quantum theory of the electron. *Proceedings of the Royal Society of London. Series A, Containing Papers of a Mathematical and Physical Character* **117,** 610–624 (1928).

101. Susi, T. *et al.* Single-atom spectroscopy of phosphorus dopants implanted into graphene. *2D Materials* **4,** 021013 (2017).

102. Enkovaara, J. *et al.* Electronic structure calculations with GPAW: a real-space implementation of the projector augmented-wave method. *Journal of Physics: Condensed Matter* **22,** 253202 (2010).

103. Blöchl, P. E. Projector augmented-wave method. *Phys. Rev. B* **50,** 17953 (1994).

104. Kresse, G. & Joubert, D. From ultrasoft pseudopotentials to the projector augmented-wave method. *Phys. Rev. B* **59,** 1758 (1999).

105. Larsen, A. *et al.* The Atomic Simulation Environment—A Python library for working with atoms. *Journal of Physics: Condensed Matter* **29,** 273002 (2017).

106. Walt, S. v. d., Colbert, S. C. & Varoquaux, G. The NumPy array: a structure for efficient numerical computation. *Computing in Science & Engineering* **13,** 22–30 (2011).

107. Hourahine, B. *et al.* DFTB+, a software package for efficient approximate density functional theory based atomistic simulations. *The Journal of Chemical Physics* **152,** 124101 (2020).

108. Rauls, E., Elsner, J., Gutierrez, R. & Frauenheim, T. Stoichiometric and non-stoichiometric (1010) and (1120) surfaces in 2H–SiC: a theoretical study. *Solid State Communications* **111,** 459–464 (1999).

109. Virtanen, P. *et al.* SciPy 1.0: Fundamental Algorithms for Scientific Computing in Python. *Nature Methods* **17,** 261–272 (2020).

110. Krommer, A. R. & Ueberhuber, C. W. *Computational integration* (SIAM, 1998).

111. Kretschmer, S., Lehnert, T., Kaiser, U. & Krasheninnikov, A. V. Formation of defects in two-dimensional MoS2 in the transmission electron microscope at electron energies below the knock-on threshold: the role of electronic excitations. *Nano Letters* **20,** 2865–2870 (2020).